SYNTHESIS AND PHOTOLUMINESCENCE PROPERTIES OF RARE EARTH DOPED ALKALINE EARTH NIOBATE PHOSPHORS FOR SOLID STATE LIGHTING APPLICATIONS

THESIS

Submitted to the Delhi Technological University

for the Award of the Degree of

DOCTOR OF PHILOSOPHY

in

APPLIED PHYSICS

by

AMIT KUMAR VISHWAKARMA

(Reg. No. 2K11/Ph.D/AP/03)

DEPARTMENT OF APPLIED PHYSICS

DELHI TECHNOLOGICAL UNIVERSITY

DELHI- 110 042, INDIA

OCTOBER-2016

SYNTHESIS AND PHOTOLUMINESCENCE PROPERTIES OF RARE EARTH DOPED ALKALINE EARTH NIOBATE PHOSPHORS FOR SOLID STATE LIGHTING APPLICATIONS

by

AMIT KUMAR VISHWAKARMA

(Reg. No. 2K11/Ph.D/AP/03)

DEPARTMENT OF APPLIED PHYSICS

Submitted

in the fulfilment of the requirements of the degree of

DOCTOR OF PHILOSOPHY

to the

**DELHI TECHNOLOGICAL UNIVERSITY
DELHI- 110 042, INDIA**

OCTOBER-2016

CERTIFICATE

This is to certify that the thesis entitled *"Synthesis and photoluminescence properties of rare earth doped alkaline earth niobate phosphors for solid state lighting applications"* submitted to the Delhi Technological University, Delhi for the award of degree of Doctor of Philosophy is based on the original research work carried out by me under the supervision of Dr. M. Jayasimhadri, Department of Applied Physics, Delhi Technological University, Delhi. It is further certified that the work embodied in this thesis has neither been partially nor fully submitted to any other university or institution for the award of any degree or diploma.

Amit Kumar Vishwakarma
Research Scholar
(Reg. No. 2K11/Ph.D/AP/03)

This is to certify that the above statement made by the candidate is correct to the best of my knowledge.

Dr. M. Jayasimhadri
Supervisor
Assistant Professor, Department of Applied Physics
Delhi Technological University, Delhi

Prof. S.C. Sharma
Head, Department of Applied Physics
Delhi Technological University, Delhi

ACKNOWLEDGEMENTS

Amit Kumar Vishwakarma

RESEARCH PUBLICATIONS
(Included in thesis)

1. **Amit K Vishwakarma**, Kaushal Jha, M. Jayasimhadri, B. Sivaiah, Bhasker Gahotri, D. Haranath *"Emerging cool white light emission from Dy^{3+} doped single phase alkaline earth niobate phosphors for indoor lighting applications"* **Dalton Transactions 44 (2015) 17166-17174** *(Impact Factor: 4.177)*.

2. **Amit K Vishwakarma**, Kaushal Jha, M. Jayasimhadri, A.S. Rao, Kiwan Jang, B. Sivaiah, D. Haranath *"Red light emitting $BaNb_2O_6$: Eu^{3+} phosphor for solid state lighting applications"* **Journal of Alloys and Compounds 622 (2015) 97-101** *(Impact Factor: 3.014)*.

3. **Amit K Vishwakarma**, M. Jayasimhadri *"Pure orange color emitting Sm^{3+} doped $BaNb_2O_6$ phosphor for solid-state lighting applications"* **Journal of Luminescence 176 (2016) 112-117** *(Impact Factor: 2.693)*.

4. **Amit K Vishwakarma**, M. Jayasimhadri, *"Significant enhancement in photoluminescent properties via flux assisted Eu^{3+} doped $BaNb_2O_6$ phosphor for White LEDs"* **Journal of Alloys and Compounds 683 (2016) 379-386** *(Impact Factor: 3.014)*.

5. **Amit K Vishwakarma**, M. Jayasimhadri, *"Synthesis and luminescent properties of europium doped $BaNb_2O_6$ nanophosphor synthesized via metal-citrate gel method"* **RSC Advances (to be submitted)** *(Impact Factor: 3.289)*.

RESEARCH PUBLICATIONS
(Other than thesis work)

1. Lokesh Mishra, Anchal Sharma, **Amit K Vishwakarma**, Kaushal Jha, B.V. Ratnam, M. Jayasimhadri, A.S. Rao, R.K. Sinha, Kiwna Jang. *"White light emission and color tunability of dysprosium doped barium silicate glasses"* **Journal of Luminescence 169 (2016) 121-127** *(Impact factor: 2.693)*.

2. B.V. Ratnam, Mukesh K Sahu, **Amit K Vishwakarma**, Kaushal Jha, H. J. Woo, Kiwan Jang, M. Jayasimhadri. *"Optimization of synthesis technique and luminescent properties in Eu^{3+} activated $NaCaPO_4$ phosphor for solid state lighting applications"* **Journal of Luminescence** (under review) *(Impact factor: 2.693)*.

ABSTRACT

The growing demand for energy together with alarming concerns over global warming and climate changes have been drawn enormous attention for investigating new efficient lighting sources primarily to reduce the world's electricity consumption. Approximately 20% of the global electricity consumption is rendered only for lighting. This not only consumes significant amount of energy, the inefficient traditional technologies also contributes to that considerably. Switching from these conventional to more energy-efficient lighting sources is essential for reducing the global energy consumption. Solid state lighting, and in particular, light emitting diodes (LEDs), have emerged as the most promising long-term solution that could meet the precise efficiency, safety, durability and reliability standards. The market for LEDs is predicted to experience a multifold expansion in the coming decade, with the majority of the growth coming from bright and efficient white light emitting diodes (w-LEDs). Currently, w-LEDs have been found in a wide variety of applications, including general lighting, automotive industry, architectural lighting, cellular phones, monitors of notebook computers etc.

Nakamura et. al developed w-LED by coating yellow emitting phosphor (YAG: Ce^{3+}) on blue InGaN LED chip. This development of phosphor converted (pc)-w-LED is a technological advancement in solid state lighting industry. However, pc-w-LED has several serious issues, such as a poor color rendering index (Ra <65) due to lack of red emission and halo effect. In an attempt to improve the Ra, many researchers have reported that the white light can be generated by coating of sulfide-based green and nitride based red emitting phosphors on blue LED chip. However, sulfide and nitride based phosphors still suffer from certain shortcomings related to their thermal and chemical instabilities. The commercially available red emitting Y_2O_3: Eu^{3+} employed in w-LED has stable chemical and physical properties, but it has negligible absorption in the blue (450-480 nm) region. Therefore, it is essential to search for a new phosphor with strong absorption under near-UV (n-UV) and blue light to render better color rendition resulting in an ideal w-LED source.

Motivated by the above mentioned facts, white, orange and red emitting various rare earth doped $BaNb_2O_6$ phosphors have been synthesized by solid state reaction method. Structural, morphological and luminescent properties have been investigated in detail. In addition to this, luminescent properties have been significantly enhanced for the red emitting $BaNb_2O_6$ phosphor by using various fluxes and also by changing the synthesis route from solid state reaction (SSR) to metal citrate gel (MCG). Based on the extensive characterization and measured luminescent properties, the outcome of the research work has been organized into seven chapters and the chapter wise summary of the same is as follows:

Chapter 1 begins with a brief introduction, motivation for the research work and an overview of the current work. This chapter includes baics concepts about phosphor and photoluminescence. Subsequently, generation of white light, solid state ligitng technology and their current applications have been discussed in detail. Spectroscopic properties of rare earth ions especially europium (Eu^{3+}) has been discussed briefly. A short description of the importance of the present work, host (ANb_2O_6; where A= alkaline earth metals) and preference of nanophosphor over the bulk phosphor have also been discussed in this chapter. Finally, the objectives of the thesis based on the review of the literature have been incorporated.

Chapter 2 describes the synthesis procedures and characterization techniques used in the current thesis. In the present work, SSR and MCG method have been used to synthesize the $BaNb_2O_6$ phosphor. Few chloride fluxes have been intentionally blended into solid state reaction method to enhance the obtained luminescence properties. This chapter elaborates the utility of many sophisticated experimental techniques such as thermogravimetric analysis (TGA)- differential scanning calorimetric (DSC), X-ray diffraction (XRD) , scanning electron microscopy (SEM), field emission scanning electron microscopy (FE-SEM), UV-Vis spectrophotometer and spectrofluoro-photometer in order to study the various properties such as thermal, structural, morphological, luminescent and colorimetric properties.

Chapter 3 presents the comprehensive study on the emerging cool white light emission from Dy^{3+} doped single phase alkaline earth niobate ($BaNb_2O_6$) phosphors for indoor lighting applications. The thermal, structural, morphological and luminescent

properties have been systematically studied to obtain the efficient cool white light from single phase $BaNb_2O_6$: Dy^{3+} phosphor. The emission spectra exhibit sharp blue ($^4F_{9/2} \rightarrow$ $^6H_{15/2}$) and yellow ($^4F_{9/2} \rightarrow$ $^6H_{13/2}$) emission bands in the visible region under n-UV excitation. The Commission Internationale de I'Eclairage (CIE) coordinates are found to be x= 0.322, y= 0.339 with CCT value 5907 K found to be in cool white region, which is close to the standard white lamp colorimetric point. The luminescent characteristics suggest that this phosphor could be the most suitable for generating an appreciable cool white light.

Chapter 4 deals with the pure orange light emitting Sm^{3+} doped $BaNb_2O_6$ phosphor for solid state lighting applications. The strong orange emission has been observed at 599 nm corresponding to $^4G_{5/2} \rightarrow ^6H_{7/2}$ under 405 nm n-UV excitation. The structural and morphological studies exhibit pure orthorhombic phase and irregular size dense particles in micrometre range. The CIE chromaticity coordinates are found to be (0.557, 0.440), which are close to the Nichia corporation developed amber LED. The calculated purity of orange color is 99.5% and correlated color temperature (CCT) is about 1970 K. The measured lifetime for optimized sample is found to be in microsecond range. The results suggested that $BaNb_2O_6$: Sm^{3+} phosphor is a potential candidate for applications in displays and solid state lighting.

Chapter 5 describes the red light emitting $BaNb_2O_6$ phosphor for solid state lighting applications. X-ray diffraction pattern for the synthesized phosphor confirms the formation of pure orthorhombic phase for $BaNb_2O_6$. The particle sizes are in the range of 3–5 μm observed for the as prepared sample. In addition to this, photoluminescence studies reveal that this phosphor exhibit intense red emission due to $^5D_0 \rightarrow ^7F_2$ transitions of Eu^{3+} ion under n-UV and blue excitations. The CIE chromaticity coordinates evaluated from the emission spectra are falling in the pure red region of the CIE 1931 diagram, which are very much close to the commercial red (Y_2O_2S: Eu^{3+}) phosphor. Based on the above results, it is concluded that Eu^{3+} doped $BaNb_2O_6$ phosphor may be potential candidate to use in w-LEDs as a red component.

Chapter 6 focussed especially on the enhancement of photoluminescence properties of Eu^{3+} doped $BaNb_2O_6$ phosphor by two ways namely (i) flux assisted solid state reaction and (ii) metal citrate gel (MCG) method. In the flux assisted solid state

reaction method, the photoluminescent properties enhanced significantly by using various chloride fluxes such as (NH_4Cl, LiCl, KCl and NaCl). Among all fluxes used, NH_4Cl was found to be a suitable flux that enhances luminescence intensity more than two times while compared to the optimized Eu^{3+} doped $BaNb_2O_6$ phosphor (synthesized by SSR without flux). The CIE chromaticity coordinates of the optimized sample are found to be (0.65, 0.35), which are well-matched with commercial red emitting Y_2O_3: Eu^{3+} phosphor.

On the other hand, in MCG method, Eu^{3+} doped $BaNb_2O_6$ phosphor has been synthesized at low processing temperature relative to the solid state reaction method. FE-SEM confirms the nanofeatures of the synthesized samples. The photoluminescence spectra exhibit enhancement in emission intensity about three times when compared to the optimized Eu^{3+} doped $BaNb_2O_6$ phosphor (synthesized by SSR without flux). The CIE chromaticity coordinates for the optimized samples are close to the NTSC standard coordinates of the red-emitting phosphors.

Finally, the conclusions have been drawn from the studies of Eu^{3+} doped $BaNb_2O_6$ phosphor that luminescent properties have been significantly enhanced in both the methods. Moreover, this phosphor may be a potential candidate to use as a red component for white LEDs and also to enhance the CRI of the commercially available phosphor.

Finally, ***Chapter 7*** includes the general conclusions derived from the present work and scope for the future work. The thesis lists the many noticeable features of the proposed new phosphors and their exceptional properties are also highlighted along with their potential use in various display applications. The thesis ends on a note that addresses the enormous scope of this work in future.

CONTENTS

List of Tables

List of Figures

1

Phosphors - An Overview

Solid-state lighting in the form of white light emitting diodes (w-LEDs) are now emerging as a cost effective, energy efficient and alternative to the conventional light sources, for next generation illumination. Moreover, the study of phosphor materials are more fascinating in the current research era. The main emphasis of this chapter is to provide the basic understanding of phosphors, mechanism of luminescence, approaches for generating white light and solid state lighting technology. Furthermore, the properties of rare earth ions have been discussed briefly in the present chapter. The motivation and importance of choosing $BaNb_2O_6$ compound as a host material and the objectives of the current work are highlighted.
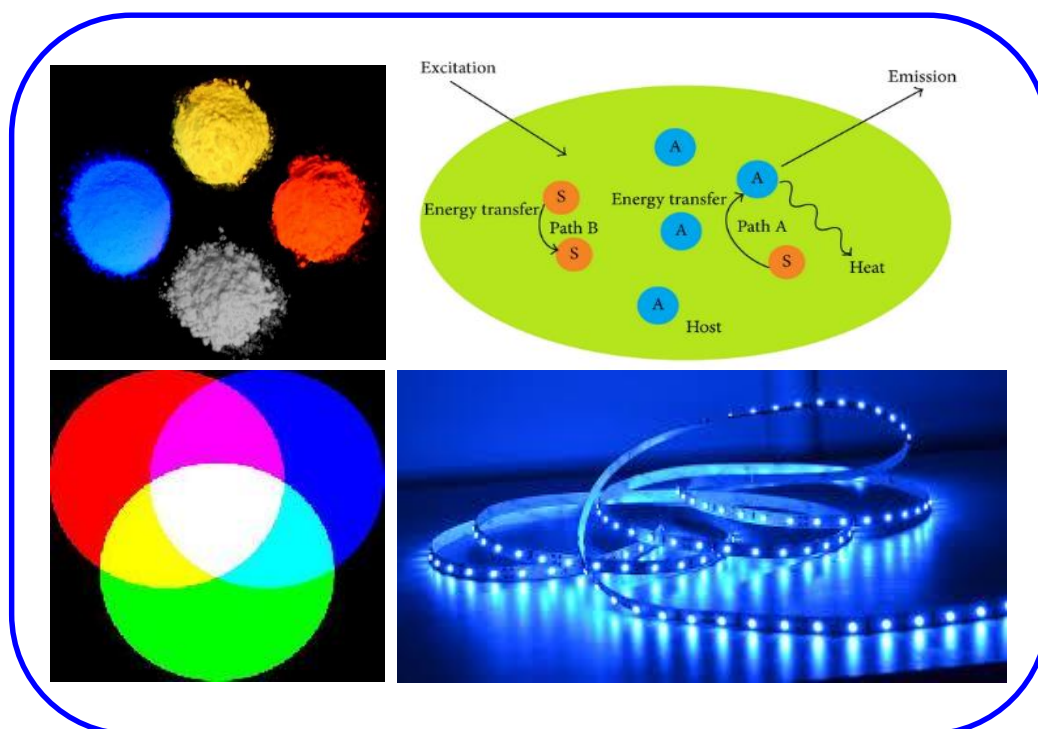
1.1. Basics of Phosphors and Luminescence

Phosphor is a substance that emits light or exhibits luminescence, when excited by some kind of external energy such as visible, ultraviolet (UV) and near infrared (NIR) sources [1]. *Phosphors* are also called as luminescent materials. The word 'luminescence' was first introduced as 'luminescenz' by a German Physicist, Eilhardt Wiedemann, in 1888, which originates from the Latin word 'lumen' means 'light' to define "all those phenomena of light which are not solely conditioned by the rise in temperature"[2]. Luminescence is often considered as cold light whereas incandescence is hot light. In another way, the word luminescence is defined the phenomena which involve absorption of energy and subsequent emission of light is known as luminescence [1]. Luminescence is a common phenomenon of our daily lives e.g. the fluorescent lamps for lighting and architectural decoration, television screens and lasers in some medical devices [3–5]. There are various types of luminescence, which can be classified depending on the method of excitation or stimulation as given in the section 1.1.2. Each process has its own significance and advantages in the field of science and technology. In the present work, more emphasis has been given to the study of photoluminescence of inorganic materials that exhibit strong emission in the visible region.

1.1.1. History of Phosphors

In the 17th century, the term "*Phosphor*" was invented by an alchemist Vincenzo Cascariolo of Bologna, Italy. He found a heavy crystalline shining stone at the foot of a volcano and fired it in a charcoal furnace to convert to noble metal. Surprisingly instead of any noble metal, he found that the sintered stone is emitting red light in the dark after exposure to the sunlight. This stone was named as "Bolognian stone" as represented in Figure 1.1 under white light and UV light exposure. This stone recognized as barite ($BaSO_4$) with the fired product being BaS ($BaSO_4 + 2C \rightarrow BaS + 2CO_2$), which is now known as phosphor material. Phosphor means "light bearer" in Greek and appears in Greek myths as the personification of the morning star Venus [6–8]. Later in 1768, Canton developed CaS and then in 1866, Sidot invented the first green emitting ZnS luminescent material. An understanding of the luminescence from these materials started in 1886 when Verneuil demonstrated that pure CaS did not exhibit luminscence, and a doping of Bi was required for light emission. Later, it was found

that a doping of Cu was essential for emission from green ZnS and Cr for red BaS [9,10].
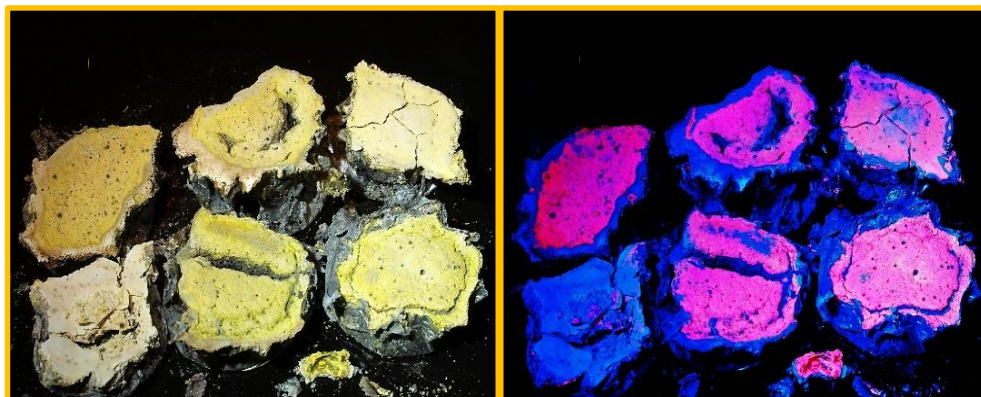
Figure 1.1. (a) Bologna stone under white light (b) Bologna stone under UV Light.

1.1.2. Types of luminescence

Luminescence is classified into different types depending upon the mode of excitation.

(i) *Bioluminescence* is generated by a living organism. It is actually chemiluminescence as the light generating molecules become excited by a chemical reaction. Some biological entities, such as fireflies, mushrooms and even bacteria exhibit bioluminescence. These produce the chemicals *luciferin* (a pigment) and *luciferase* (an enzyme). The luciferin reacts with oxygen to produce light. The luciferase acts as a catalyst to speed up the reaction.

(ii) *Chemiluminescence* (*Chemoluminescence*): This type of luminescence results from some chemical or electrochemical reactions. In this, two chemicals react to form an excited (high-energy) intermediate, which breaks down by releasing some of its energy as photons of light.

(iii) *Photoluminescence* is caused by moving electrons to energetically higher levels through the absorption of photons.

    (a) *Fluorescence:* Rapid emission of photon as electrons jump from excited state to lower energy level.

    (b) *Phosphorescence:* Delayed (millisecond to hours) emission of photons that have been trapped in forbidden state.

(iv) *Mechanoluminescence* is resulting from any mechanical action on a solid. It can be further subdivided into three groups: Triboluminescence, Fractoluminescence and Piezo-luminescence.

    (a) *Triboluminescence:* Luminescence due to disruption of bonds in crystal by fractures.

    (b) *Fractoluminescence:* Luminescence due to exerted pressure.

    (c) *Piezoluminescence:* Luminescence produced during crystallization.

(v) *Crystalloluminescence* is occasionally produced during crystallization.

(vi) *Sonoluminescence* is the emission of short bursts of light from imploding bubbles in a liquid when excited by sound.

(vii) *Radioluminescence* is generated when some materials are exposed to ionizing radiation like α, β or γ rays.

(viii) *Thermoluminescence*, unlike what the name suggests, is luminescence activated thermally after initial irradiation by other means such as α, β, γ, UV or X-ray s. This happens when previously absorbed energy is stored at defects and is released in the form of light on application of some thermal energy. It is used in dating archeological artifacts.

(ix) *Electroluminescence* is produced when the excitation is by a voltage applied to the luminescent material.

(x) *Cathodoluminescence* is produced when the excitation is by energetic electrons or cathode rays. Ex: Displays, cathode ray tube or TV tube and electron microscope (TEM type) screens.

1.1.3. Photoluminescence

The phenomenon of absorption of energy (electromagnetic radiation in the form of photons) and subsequent emission in a visible region is known as photoluminescence [8,11]. Figure 1.2 shows the schematic energy level diagram of the luminescent ion to illustrate the possibility of obtaining photoluminescence.

Generally this is two-step process: one is excitation and another emission. Basically, an incoming photon excites the ion from its ground level to the higher energy level (excited state). The excited ion returns to the ground state either radiatively or non-radiatively. The radiative emission process gives a photon, and the non-radiative return gives a phonon (heat or lattice vibration) [12,13]. The former is the one through

which the luminescence process occurs, and the other is the energy of the excited state is used

Excited state

Photo excitation   **R**   **NR**

Ground state
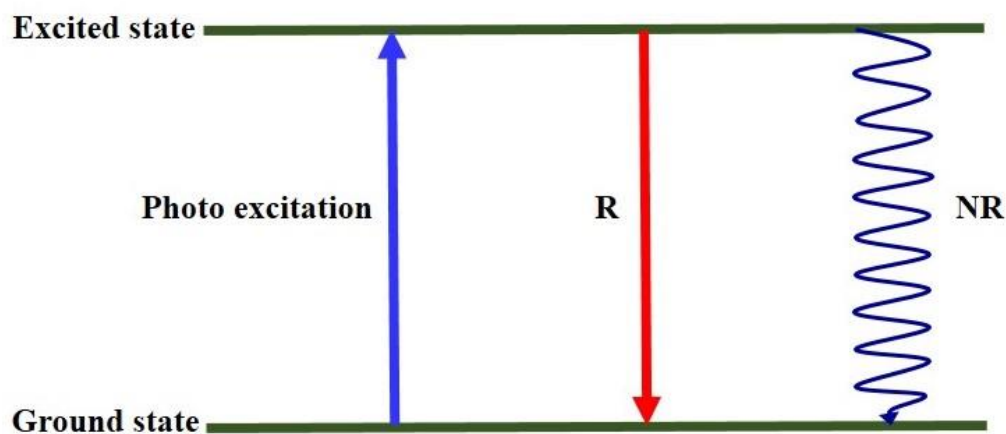
Figure 1.2. Schematic diagram of photoluminescence process.

to excite due to the vibrations of the host lattice. In order to generate efficient luminescence, it is necessary to suppress this non-radiative process. Further, photoluminescence is divided into two processes: (i) *fluorescence* and (ii) *phosphorescence*. Fluorescence and phosphorescence are photon emission processes that occur from excited electronic states. The classification is mainly based on the emission after the source of exciting energy is removed. The delayed emission ($> 10^{-8}$ sec) is generally known as phosphorescence and emission during the time of excitation is called as fluorescence [14,15]. More clearly, fluorescence is light emission from a sample during the time when it is exposed to radiation, whereas phosphorescence is the light that appears from the sample after the interruption of excitation. However, it should be noted that these definitions are applicable only to inorganic materials. For organic molecules, different terminology is used as light emission from an excited singlet state is called fluorescence while that from a triplet excited state is defined as phosphorescence. Another distinction is made between fluorescence and phosphorescence is based on the temperature dependence of the luminescence decay time. Fluorescence is independent of the excitation intensity and of temperature with decay time less than 10^{-8} seconds whereas phosphorescence is often depended on the intensity of excitation and strongly dependent on temperature with a decay time of more than 10^{-8} seconds (varies from µs to minutes, hours and even days) [16–18].

1.1.4. Luminescence mechanism and energy transfer

The emission of electromagnetic radiation in excess of thermal radiation is known as luminescence. Luminescence is entirely different from incandescent emission process in which solid emit light due to the reason of their high temperature. Luminescence arises when the atoms of material become energized by electromagnetic radiation (UV, n-UV, visible, IR, X-ray, etc.) in some way without any heating of material [4,19]. These atoms then release the energy in the form of visible radiation. In the present work, inorganic phosphors are used to convert UV/n-UV/blue radiation into particularly visible radiation for w-LED applications. Phosphor consist of a host and an activator also called as luminescent center [4].

Energy transfer (ET) between ions plays a vital role in the phosphor-converted w-LEDs. The basic process of energy transfer is presented in this section. Before going to discuss energy transfer process, it is better to introduce some terms which are frequently used such as sensitizer (S) and activator (A). Phosphors are generally inorganic materials doped with small quantity of impurities or additives or quencher called as dopants or activators. The ion or group act as a luminescence center in the phosphor is called activators of the host lattice. The absorption of energy takes place either by host lattice or activators. However, in most of the cases, the emission occurs only at the activator sites. The sensitizer added to improve or enhance the absorption. In an energy transfer process, a sensitizer sensitizes the activator and the activator emit the expected light emission. Of course, the ion, group or molecule of the host itself can also act as a sensitizer to transfer the absorbed excitation energy to the activator. This is called as host sensitization [20–22]. However, part of the excitation energy can transfer from one center to other luminescent centers. The electron in the luminescent centers transport to excited states after absorbing excitation energy and the energy in the excited states can usually be disbursed in the following ways: (i) emission of light (photon) via direct excitation of the activator as shown in Figure 1.3 (a) and (ii) emission of light (photon) by indirect excitation from the sensitizer to the activator via phonon emission or transfer of energy (as shown in Figure 1.3 (b)).
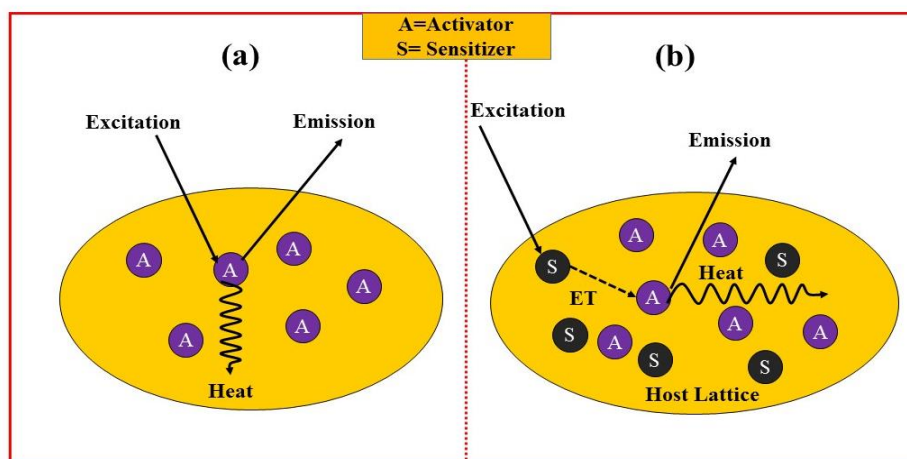
Figure 1.3. Schematic representation of luminescence processes in a phosphor.

The luminescence in inorganic phosphors is usually consists of excitation, energy transfer, and emission processes as shown in Figure 1.3 (b) [19,23]. There are two main processes involved in emission from the luminescent center for the phosphor. The first one is called Stokes emission where the energy of the emitted photons is lower than that of the incident photon. Lattice relaxation causes the energy loss due to a change in the strength of the chemical bond.
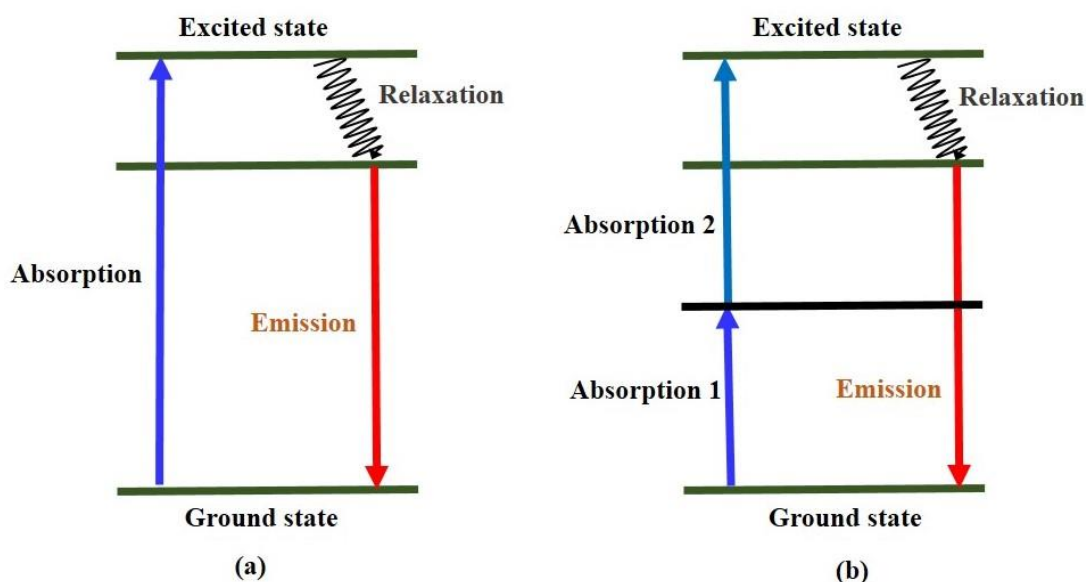
Figure 1.4. Schematic representation of energy transfer processes for (a) Stokes emission (b) Anti-Stokes emission.

The gap between absorption and emission energy band is called the Stokes shift [24]. On the other hand, there is also the possibility that a phosphor, when excited with longer wavelength light source could absorb two (or several) photons at one time and emit a photon of higher energy than the incident photon. This process is called up-conversion, and the emission is called anti-Stokes emission. Both Stokes and anti-Stokes emissions are shown in Figure 1.4.

Apart from the energy transfer by movement of electron transfer, there are four basic mechanisms involved in energy transfer processes between ions (i) Resonant radiative energy transfer through emission of sensitizer and re-absorption by activator (ii) Non-radiative transfer associated with resonance between sensitizer and activator. (iii) Multi-photon assisted energy transfer and (iv) Cross relaxation between two identical ions. The efficiency of radiative energy transfer depends upon how the efficiently activator is excited by the sensitizer emission as represented in Figure 1.5 (a). There should be significant overlap between the emission spectrum of the sensitizer and the excitation spectrum of the activator. The lifetime of the sensitizer fluorescence does not vary with activator concentration, if radiative energy transfer takes place predominantly. In Figure 1.5 (b), significant decrease in the decay time of sensitizer fluorescence with the increasing activator concentration exhibit the non- radiative energy transfer. The equal energy difference between the excited states of the sensitizer to the activator leads the energy transfer mechanism. Non-resonant energy transfer can take place with the aid of a phonon if the difference between the ground and excited state of sensitizer and activator is large. The energy transfer mechanism in phosphors mainly depends on the competitive interaction and characteristic transitions of sensitizer and activator and the distance between them. If the two ions have different excited states the probability of energy transfer is negligible known as phonon-assisted non-radiative transitions as shown in Figure 1.5 (c). Cross-relaxation terminology refers to all kinds of down conversion energy transfer between identical two adjacent luminescent centers or ions. Figure 1.5 (d) shows simple possible energy level scheme involving cross-relaxation, when the first ion initially in an excited state exchanges energy with the second ion that is initially at ground state, resulting the both ions simultaneously changing to intermediate states within the energy between the two initial states [22,25].
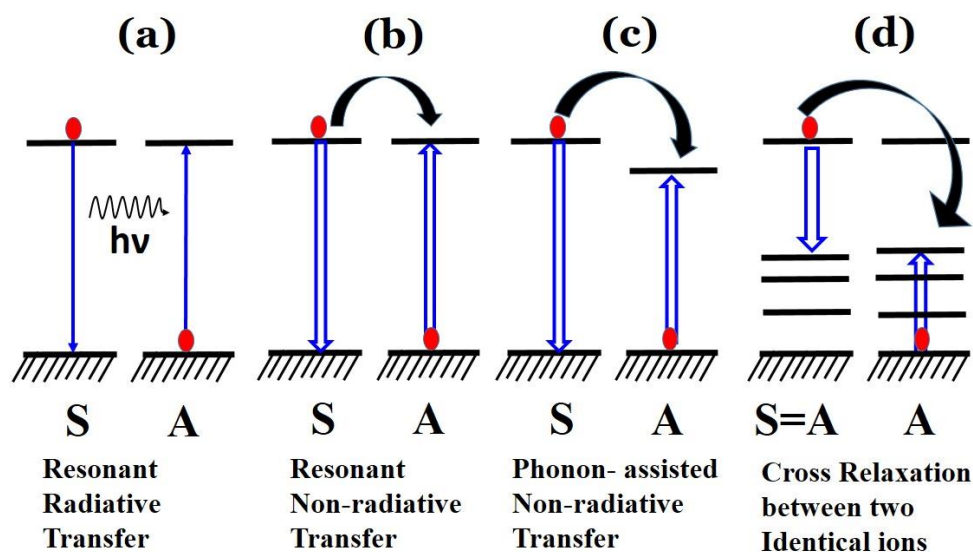
Figure 1.5. Schematic diagram for different energy transfer processes between the two ions.

However, emission properties of the phosphors are sensitive to the crystal field. As mentioned above, light absorption, the energy transfers between the various dopants, radiative and non-radiative relaxation processes present in the phosphor can be determined by the local environment that surrounds the activator ions. Phosphors are made from a suitable host material by adding suitable activator. Rare earth and transition metal ions usually act as activators or energy converters. In the present work, the activators are limited to only rare earth ions.

1.2. Basics of Rare Earth Ions

1.2.1. History of rare earths

In the history, Lanthanides have been called "rare earth" because it was believed that these elements were intermittently distributed in nature. They are relatively abundant in nature and because of their special properties have become of importance. The rare earth ions most regularly used for the applications in phosphors, lasers, optical switching, compact disc players and amplifiers etc. The rare earth forms a group of chemically similar elements which have in common an open 4f shell and also called as lanthanons. In terms of their electronic configuration, rare earths correspond to the progressive filling of 4f shells containing the 14 elements. The 4f shells are shielded by

5s and 5p shells, so do not play more role in their chemical bonding with other atoms [21,26]. Therefore, the 4f electrons are only weakly perturbed by the charge of the surrounding ligands. The spectra of lanthanide compounds are sharp and similar to the spectra of atom. The shielded character of the 4f orbitals is also responsible for the unique optical properties of rare earth ions. Table 1.1 gives the outer electronic configuration and ground states of rare earth ions of different ionic state [27,28]. Most of the rare earth elements exhibit many oxidation states and variable valency though the sesquioxides RE_2O_3 is usually more widespread form. Commonly, rare earth ions in crystal form exists as trivalent (RE^{3+}) or divalent (RE^{2+}) cations with their electronic configurations as $4f^n\ 5s^2\ 5p^6$ or $4f^{n-1}\ 5d\ 5s^2\ 5p^6$, respectively and gives emission in infrared (IR), visible and UV regions for the realization of optically active materials for photonic and optoelectronic applications (see the Table 1.2). Certainly, the particular electronic configuration leads to a variety of interesting optical properties that are successfully used in commercial applications, and considerable effort is still dedicated to the development of novel materials and the exploration of physical phenomena. In the periodic table, rare earth group starts with lanthanum (Z=57) and ends with lutetium (Z=71). Table 1.2 gives the physical properties of trivalent rare earth ions based on the electronic configuration along with their ground state, atomic number, weight, melting point, boiling point and ionic radius. Among all rare earths, Promethium (Pm) exhibit radioactive property with very short half-life time and does not appear in nature at all. It was first synthesized in the atomic reactor and currently used in human circulatory analysis for computerized axial tomography (CAT) scans when injected into the body. Figure. 1.6 shows Dieke diagram for the energy levels originating from trivalent rare earth (RE^{3+}) ions [27,29]. In a periodic table, yttrium (Y) and scandium (Sc) are not lanthanides but due to similar chemical properties allow them to include in rare earths category.

Table 1.1. Outer electronic configuration and ground states of rare earth ions with different ionic states.

Symbol (Atomic No.)	Configuration (Ground state)			
	Ln^0	Ln^+	Ln^{2+}	Ln^{3+}
La (57)	$5d^1\,6s^2\,(^2D_{3/2})$	$5d^2\,(^7F_2)$	$5d^1\,(^2D_{3/2})$	$4f^0\,(^1S_0)$
Ce (58)	$4f^1\,5d^3\,6s^2\,(^1G_4)$	$4f^1 5d^1 6s^2\,(^2G_{7/2})$	$4f^2\,(^3H_4)$	$4f^2\,(^2F_{3/2})$
Pr (59)	$4f^3\,6s^2\,(^4I_{3/2})$	$4f^3\,6s^2\,(^5I_4)$	$4f^3\,(^4I_{9/2})$	$4f^2\,(^3H_4)$
Nd (60)	$4f^4\,6s^2\,(^3I_4)$	$4f^4\,6s^2\,(^6I_{7/2})$	$4f^4\,(^3I_4)$	$4f^3\,(^4I_{9/2})$
Pm (61)	$4f^5\,6s^2\,(^6H_{5/2})$	$4f^5\,6s^2\,(^7H_2)$	$4f^5\,(^6H_{5/2})$	$4f^4\,(^3I_4)$
Sm (62)	$4f^6\,6s^2(^7F_0)$	$4f^6\,6s^2\,(^4F_{3/2})$	$4f^6\,(^7F_0)$	$4f^5\,(^6H_{5/2})$
Eu (63)	$4f^7\,6s^2\,(^8S_{3/2})$	$4f^7\,6s^2\,(^9S_4)$	$4f^7\,(^8S_{7/2})$	$4f^6\,(^7F_0)$
Gd (64)	$4f^7 5d^1 6s^2\,(^9D_2)$	$4f^7 5d^1 6s^1\,(^{10}D_{5/2})$	$4f^7 5d^1\,(^9D_2)$	$4f^7\,(^8S_{7/2})$
Tb (65)	$4f^9\,6s^2\,(^6H_{15/2})$	$4f^9\,6s^2\,(^7H_8)$	$4f^9\,(^6H_{15/2})$	$4f^8\,(^7F_6)$
Dy (66)	$4f^{10}\,6s^2\,(^5I_8)$	$4f^{10}\,6s^2\,(^6I_{17/2})$	$4f^{10}\,(^5I_8)$	$4f^9\,(^6H_{15/2})$
Ho (67)	$4f^{11}\,6s^2\,(^4I_{15/2})$	$4f^{11}\,6s^2\,(^5I_8)$	$4f^{11}\,(^4I_{15/2})$	$4f^{10}\,(^5I_8)$
Er (68)	$4f^{12}\,6s^2\,(^3H_6)$	$4f^{12}\,6s^1\,(^4H_{13/2})$	$4f^{12}\,(^3H_6)$	$4f^{11}\,(^4I_{15/2})$
Tm (69)	$4f^{13}\,6s^2\,(^2F_{7/2})$	$4f^{13}\,6s^1\,(^3F_4)$	$4f^{13}\,(^2F_{7/2})$	$4f^{12}\,(^3H_6)$
Yb (70)	$4f^{14}\,6s^2\,(^1S_0)$	$4f^{14}\,6s^1(^4S_{1/2})$	$4f^{14}\,(^1S_0)$	$4f^{13}\,(^2F_{7/2})$
Lu (71)	$4f^1 5d^1 6s^2\,(^2D_{3/2})$	$4f^{14}\,6s^2\,(^1S_0)$	$4f^{14}\,6s^1$ $(^2S_{1/2})$	$4f^{14}\,(^1S_0)$

Table 1.2. Physical properties of rare earth ions.

Symbol	Atomic number (Z)	Atomic weight (amu)	Melting point (K)	Boiling point (K)	Ionic (Ln^{3+}) radius (Å)	Electronic Configuration (Ln^{3+})	Ground state (Ln^{3+})
La	57	138.91	1191	3737	1.032	$[Xe]4f^0$	$^1S_0$
Ce	58	140.116	1071	3706	1.010	$[Xe]4f^1$	$^2F_{5/2}$
Pr	59	140.91	1204	3793	0.990	$[Xe]4f^2$	$^3H_4$
Nd	60	144.24	1294	3347	0.995	$[Xe]4f^3$	$^4I_{9/2}$
Pm	61	145	1315	3273	0.983	$[Xe]4f^4$	$^5I_4$
Sm	62	150.36	1347	2067	0.958	$[Xe]4f^5$	$^6H_{5/2}$
Eu	63	151.964	1095	1802	0.947	$[Xe]4f^6$	$^7F_0$
Gd	64	157.25	1586	3546	0.938	$[Xe]4f^7$	$^8S_{7/2}$
Tb	65	158.93	1629	3503	0.923	$[Xe]4f^8$	$^7F_6$
Dy	66	162.5	1685	2840	0.912	$[Xe]4f^9$	$^6H_{15/2}$
Ho	67	164.93	1747	2973	0.901	$[Xe]4f^{10}$	$^5I_8$
Er	68	167.26	1802	3141	0.090	$[Xe]4f^{11}$	$^4I_{15/2}$
Tm	69	168.934	1818	2223	0.880	$[Xe]4f^{12}$	$^3H_6$
Yb	70	173.04	1092	1469	0.868	$[Xe]4f^{13}$	$^2F_{7/2}$
Lu	71	174.967	1936	3675	0.861	$[Xe]4f^{14}$	$^1S_0$
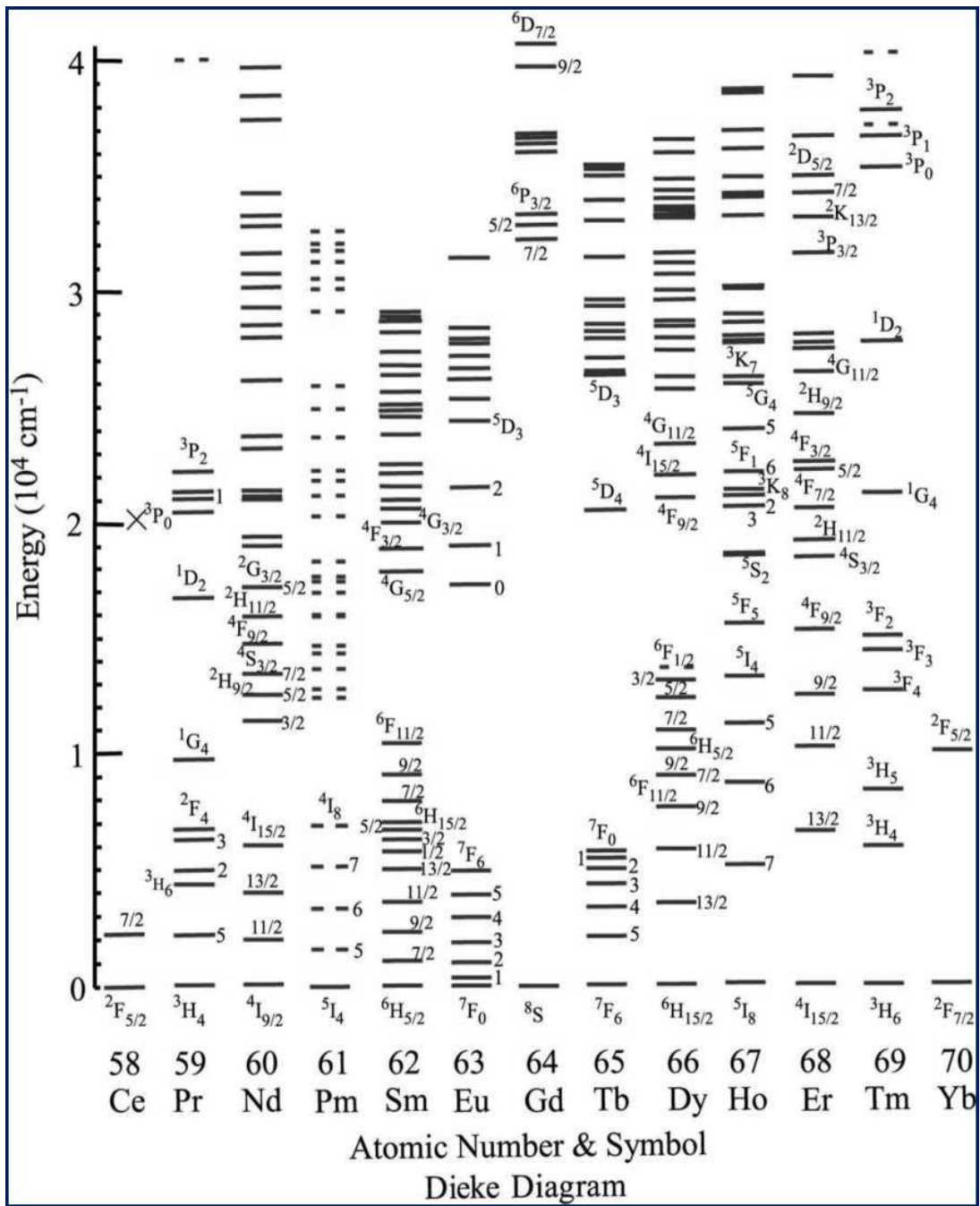
Figure 1.6. Dieke diagram for energy levels of RE^{3+} ions [29]. The configuration range from f^1(Ce^{3+}) to f^{13} (Yb^{3+}).

1.2.2. Intra-configurational f-f transitions

Absorption and luminescence spectroscopy are an important methods to understand the lanthanide systems because they allow concluding the natural frequencies of lanthanide ions. The absorption spectra exhibit a group of narrow lines or broadened spectra in the case of a single crystal, solution and glasses. These bands and lines are attributed to electronic transition inside 4f shell. Each band corresponds to the transitions between two $^{2S+1}L_J$ free ion levels (or J-manifolds). They are not escorted by a change in intra-configurational transitions. The mechanism of intra-configurational f-f transitions in rare earth ions may be interpreted in three types: (i) electric dipole or induced electric dipole transitions, (ii) magnetic dipole transitions and (iii) electric quadrupole transitions [30,31]. The f-f transitions between electronic states of rare-earth ions is predominantly of electric-dipole nature. Magnetic dipole and electric quadrupole transition are allowed, but their contributions to radiative decay are small.

(i) Electric dipole or induced electric dipole transitions: An electric dipole transition is the consequence of the interaction of the spectroscopically active RE^{3+} ion with the electric field vector of the electromagnetic radiation through an electric dipole. Electric dipole transitions between states of 4f and 5d configurations are parity allowed. The oscillator strengths for f-d transitions are therefore much larger than that of f-f transitions with the magnitude of 10^{-1}-10^{-2}. The selection rules for electric dipole transitions are $\Delta l = \pm 1$; $\Delta \tau = 0$; $\Delta S = 0$; $|\Delta L| \leq 6$; $|\Delta J| \leq 6$, $|\Delta J| = 2,4,6$ if J= 0 (or) J′=0. The creation of an electric dipole supposes a linear movement of charge, which has odd parity. The electric dipole operator has, therefore, odd transformation properties under inversion with respect to an inversion center. Intra-configurational electric dipole transitions are forbidden by the Laporte selection rule. However, the forbidden f-f electric dipole transitions arise from the admixture of the $4f^N$ configuration with the excited configuration of the opposite parity (e.g. $4f^{N-1}5d$ (or) $4f^{N-1}5g$). Noncentrosymmetric interactions allow the mixing of electronic states of opposite parity. The observed transitions are much weaker than the ordinary electric dipole transitions. These are called as induced electric dipole transitions possessing the intensities of the order of 10^{-6}.

(ii) Magnetic dipole transitions: Magnetic dipole transitions are caused by the interaction of the spectroscopic active RE^{3+} ion with the magnetic field component of

the light through a magnetic dipole. The intensity of the magnetic dipole transition is weaker than the induced electronic-dipole transitions and is of the order of 10^{-8}. A magnetic dipole transitions have even parity and are parity allowed between states of f^N and subject to selection rules $\Delta\tau = \Delta S = 0$ and $\Delta J = 0, \pm 1$ (but $0 \leftrightarrow 0$ forbidden).

(iii) Electric quadrupole transitions: The electric quadrupole transitions arise from a displacement of charge that has a quadrupolar nature. An electric quadrupole consists of four point charges with overall zero charge and zero dipole moment. An electric quadrupole has even parity. Electric quadrupole transitions are much weaker than the induced electric dipole and the magnetic dipole transitions. So far, no experimental evidence exists for the occurrence of quadrupole transition in lanthanide spectra. However, hypersensitive transitions are considered as pseudo-quadrupole transitions, because these transitions obey the selection rules of quadrupole transitions. These transitions are parity allowed among the states of f^N with the selection rules $\Delta S = 0$ and $|\Delta L| = |\Delta J| \leq 2$. On the other hand, hypersensitive transitions are found to be very sensitive to the host environment and the ion concentrations. Since there is some peculiarity in their intensity variations, such absorption transitions are known as "hypersensitive transitions." These selection rules are the same as that of a pure quadrupole transitions, but calculations have revealed that the intensities of hypersensitive transitions are larger in magnitude. Therefore, hypersensitive transitions have been called as pseudo-quadrupole transitions. According to Jorgensen and Judd [32,33], the hypersensitivity of bands is due to the inhomogeneity of the ligand environment. Karraker [34] concluded that the hypersensitive transitions show differences, which are characteristic for the coordination and symmetry of the lanthanide ion. Choppin et al. [35] suggested that the band shape and intensity of hypersensitive transitions could be used as a qualitative indication of the site symmetry.

1.2.3. Significance of trivalent rare earth ions as activators

Trivalent lanthanides have been the most extensively used as activator ions for various luminescent devices. Some of the unique properties of rare earth ions that distinguish them from other optically active ions are as follows:

(i)   They emit narrow lines, almost monochromatic light and have long emission lifetimes.

(ii)   Luminescence of RE^{3+} ions spreads in the various spectral ranges.

(iii)   Their intra-configurational f-f transitions have small homogeneous linewidths.

(iv)   They possess several excited states suitable for optical pumping

(v)   Well-developed theoretical models are available for accurate energy level analysis, transition intensities and to predict/understand excited state dynamics.

These distinct properties enable rare earth ions to perform excellently in many optical applications and luminescent devices.

1.3. Solid State Lighting: LED Technology

The fast growth of w-LED opens the new opportunity in the general illumination market. Solid state lighting (SSL) commonly referred to the lighting application using light emitting diode, organic light emitting diode (OLEDs) and light emitting polymers. The history of solid state lighting goes back more than a century in 1907 when H. J. Round invented green light emission from a silicon carbide junction diode [36]. Another scientist Losev detected similar observation in 1927. However, this broad invention remained unnoticed for a long time till 1962. In 1962 Nick Holonyak developed first commercial LEDs at General Electric. However, there was no application except displays and signing boards [37,38]. A revolution took place in the development of semiconductor (InGaN/GaN) based blue LED chip by Shuji Nakamura in 1993. Nichia Corporation brought first commercial w-LED into the market in 1996. The SSL received considerable attention in the past decades due to their inherent advantages such as high-efficiency, low energy consumption and long lifetime comparative to the traditional light sources. Thus SSL is emerging as extremely competent field and a possible alternative to existing lighting technology. SSL system is still on its way to surpass the fluorescent lighting in price and efficiency. However already achieved performance in terms of the lifetime and internal efficiency clearly indicates their future potential [39,40]. Likewise other conventional light sources, LEDs are not inherently white light source, and they emit nearly monochromatic light. Owing to this reason LEDs are highly efficient for colored light application such as traffic light and signboards. Semiconductor LEDs made from doping of elements in the semiconductor to create the p-n junction. The diodes emit light when a suitable potential

is applied, leads to various color emission depends on the band gap of the semiconductor. However, generation of white light from this monochromatic source is essentially required [41–44].

1.4. Generation of White Light

There are various approaches to obtain efficient white light. The three most popular approaches are shown in Figure 1.7. These are (i) Mixing of three monochromatic red, green and blue LEDs (ii) Combination of blue LED with yellow phosphors (iii) UV LED absorb short wavelength and down convert it to longer wavelength emission with blue and yellow phosphors (or red, green and blue phosphors) [12,45]. Naturally, there are pros and cons to each of the methods. The advantage using a blue LED with yellow phosphor (YAG: Ce^{3+}) is its high theoretical efficacy, which is attractive for the creation of a cheap, bright white light source. However, this benefit comes at the expense of a lower value for the colour-rendering index (CRI), which is typically so low that such devices are undesirable for indoor use. UV/n-UV LEDs with phosphor mixtures provide a better CRI value and are suitable for indoor applications but at the expense of poorer efficacy [46,47]. The potential advantages and technical challenges in each method are listed in Table 1.3.

Table 1.3. Advantages and disadvantages of various white light generation approaches.

Method	Advantages	Disadvantages
RGB LEDs	• No quantum deficit • White point control • Excellent CRI	• No control on CCT • Complex circuit • Variable lifetime of each LEDs
Blue LED + Yellow phosphor	• Small, light weight • Easy to fabricate • Long lifetime	• Poor CRI • Less efficient
UV/n-UV LED + RGB phosphors	• Gives good white color • Excellent CRI • Cost effective than RGB LEDs	• Less efficient due to stokes conversion • Difficult to control the uniformity of phosphor coating • Different ageing of phosphors
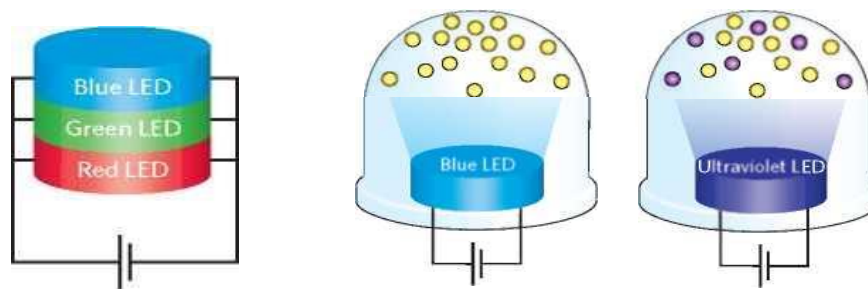
Red+Green+Blue LEDs   Blue LED+ Yellow Phosphor   UVLED+ RGB Phosphor

Figure 1.7. Three dominant ways to produce LED-based white light.

1.5. Why More Research on Red Phosphors is Required?

The most common methods for generation of white light are (i) a blue LED with yellow phosphor and (ii) a UV/n-UV LED with tricolor phosphors. Commercially available phosphor converted w-LED is made of with yellow phosphor (YAG: Ce) coated with GaInN LED (450-470nm) chip. YAG: Ce based w-LED emit cool white light due to which restricts their uses due to low CRI and high CCT. This limitation is caused by lack of red component in the yellow phosphor and has gained research attention. Still, they are suffering from poor CRI due to the separation of blue and yellow color (Halo effect). Another method, n-UV chip with tricolor phosphor (red, green, blue) is obvious way to produce white light. Currently, n-UV LED based w-LEDs are using $Y_2O_2S: Eu^{3+}$, $ZnS: Cu^{2+}, Al^{3+,}$ and $BaMgAl_{10}O_{17}: Eu^{2+}$ phosphors for red, green and blue emission, respectively [48–50]. However, this approach has three basic problems. The first is that the efficiency of red phosphor, which cannot absorb the light in UV region, and its brightness is much less than the commercially available green and blue phosphor. The sulfide-based red phosphor has high emission efficiency but due to less chemical stability and high toxicity, restricts their commercial application. The other main commercial red phosphors in today's market also made with the sulfide based material. Nitride-based phosphors requires high pressure and temperature and has broad emission in the deep red region which is insensitive to human eyes [51]. Thus novel red phosphor materials that could be effectively excited in the n-UV and blue region with excellent absorption and emission properties along with good thermal and chemical stability, minimal thermal quenching, high quantum yield and preferably with low manufacturing cost are needed to meet the market requirements.

1.6. Eu^{3+} Activated Phosphor

Extensive research has been performed for the synthesis and development of diverse red phosphors with various hosts and activator ions. Published literature indicates that various nitride based broadband emitting Eu^{2+} and Mn^{2+} activated red phosphors have been developed. However, broad emission leads to a spillover into the deep red which is insensitive to the human eye and leads to decrease in spectral efficiency [52]. Therefore, narrow emitters are in demand good color purity. Rare earth ions (RE^{3+}) particularly Eu^{3+}, Sm^{3+}, and Dy^{3+} are suitable as activators, due to their sharp transitions within the 4f shell. They exhibit narrow emission lines due to intra-configurational f - f transitions and are widely used as the activators. Among all rare-earths, Eu^{3+} ions are excellent dopant for red luminescence as they exhibit a high quantum efficiency and photostability at same time [53,54]. Eu^{3+} ions form a number of discrete energy levels owing to the presence of these deep-lying 4f shell which is not entirely filled. Luminescence originating from electronic transitions between 4f levels, which is mostly due to the magnetic dipole and electric dipole transitions and these transitions offer the possibility of efficient emissions. Electric dipole transitions are parity forbidden. The intensity of these transitions depends strongly on the site symmetry in a host crystal. Magnetic dipole transitions are not affected much by the site symmetry because they are parity allowed. Red luminescence of trivalent europium (Eu^{3+}) ions due to f - f transitions is of technological importance since it has been extensively used in phosphors for lamps and color displays. It is known that emission wavelengths of Eu^{3+} are determined primarily by their local environment in host crystals. When the Eu^{3+} ions are embedded in a site with inversion symmetry, the $^5D_0 \rightarrow {}^7F_1$ magnetic dipole transition is intense, while in a site without inversion symmetry the $^5D_0 \rightarrow {}^7F_2$ electric dipole transition is hypersensitive [53,55]. The intensity ratio of $^5D_0 \rightarrow {}^7F_2$ to $^5D_0 \rightarrow {}^7F_1$ is called as asymmetry ratio, which gives a measure of the degree of distortion from inversion symmetry of the local environment around the Eu^{3+} ions in the host matrix [32].

Eu^{3+} ions have tremendous technological applications and therefore its luminescence properties have been studied in many host lattices such as phosphates, silicates, nitrides, oxynitrides, borates, fluorides, oxyfluorides, etc. Each of these host matrices has its advantages and disadvantages. As already mentioned most of the well-known red emitting phosphors for w-LEDs, usually are based on sulfide

semiconductors such as $Zn_{1-x}Cd_xS$: Ag [9,56], Ba_2ZnS_3: Mn [57], CaS: Eu [58,59], SrY_2S_4: Eu [60], etc. are available in the market. Moreover, tungstates or molybdates are considered as potential host for Eu^{3+} doped ions due to the intense charge transfer band, absorption in UV region, effective f - f transitions of Eu^{3+} in n-UV and blue region which gives excellent thermal, catalytic and hydrolytic properties. Silicate-based phosphor materials have also been explored as silicate material, which have good chemical and thermal stability although it was difficult to form single phase host. Rare earth doped alkaline earth niobates like ANb_2O_6 (A= alkaline earth metals) has drawn attention in the area of research due to their enormous technological applications [61–63]. Rare earth doped luminescent properties have not been studied much more for alkaline earth niobates. In the present thesis, major work has been focused to enhance the photoluminescence properties of Eu^{3+} in alkaline earth niobate host using various fluxes, and different synthesis techniques.

1.7. Applications of Phosphors

Rare earth doped luminescent materials (phosphors) have been thoroughly investigated and are widely used due to their potential applications such as color TV screens, optoelectronics, discharge lamp, sensors, biological labeling, plasma display panels, luminous paints, and especially in white LEDs etc [64–67]. Figure 1.8 display the few applications of phosphors which are being used currently. Figure 1.9 presents the phosphor devices based on the mode of excitation.

| Plasma Display | Solar cell | White LEDs |
| Security Inks | Luminous Paints | Bio-imaging |
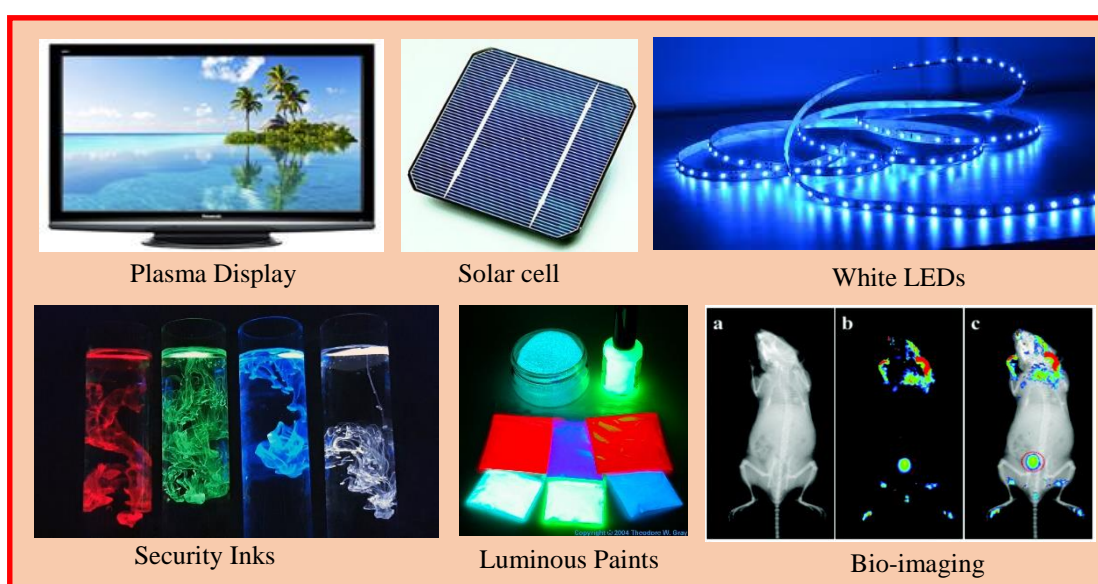
Figure 1.8. Applications of luminescent materials.
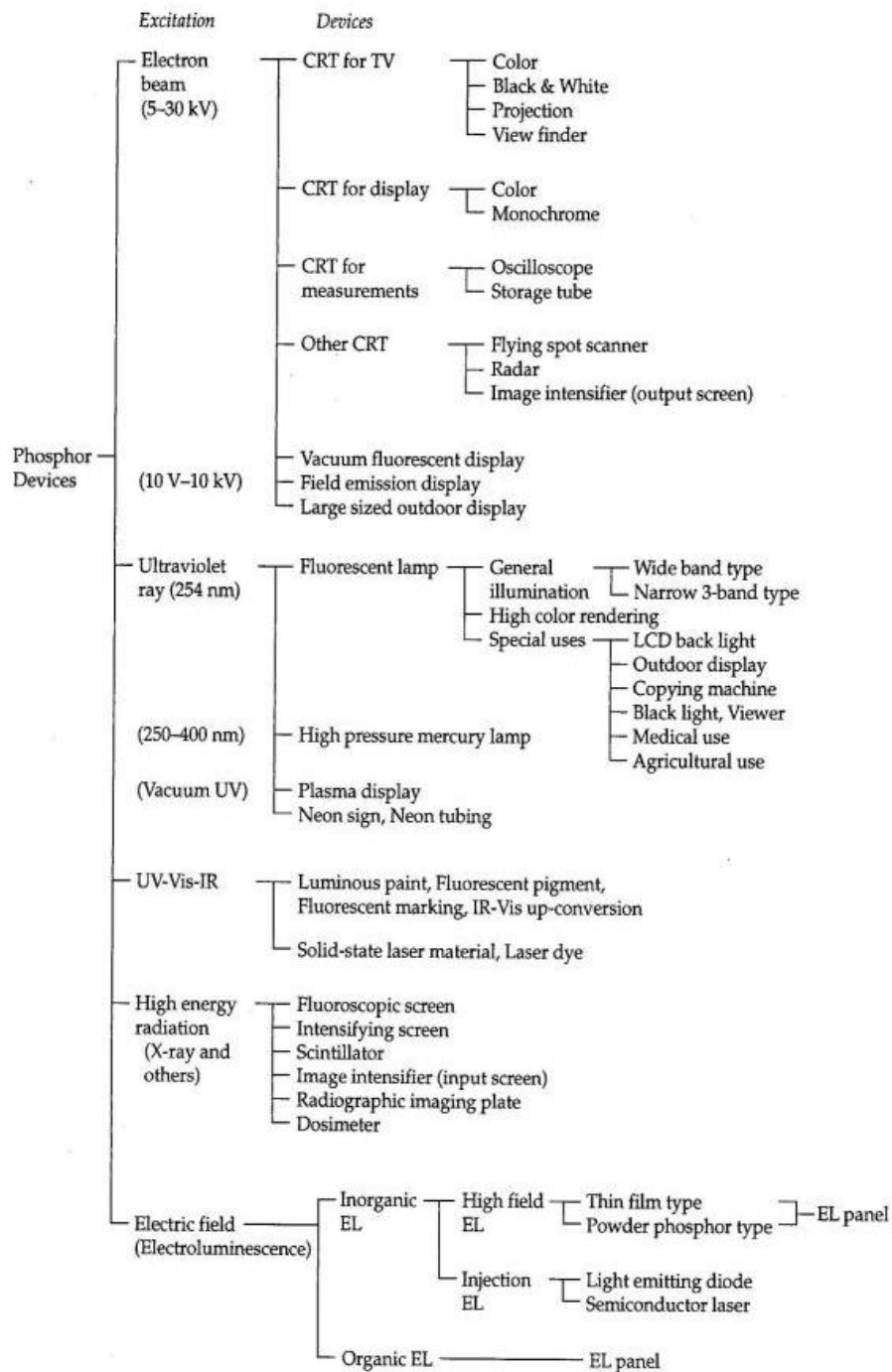
Figure 1.9. Classification of phosphor devices based on the mode of excitation

1.8. Common Lighting Technologies

Artificial light has long been a significant contributor to the quality and productivity of human life. Discovery of fire is the earliest form of artificial lighting is also known as first generation of lighting. Progressively over the years, mankind

developed a better light source and therefore various technologies were established. Among all of them, incandescent and fluorescent lights led the lighting industry for a long time. In the Incandescent bulbs, when an electrical current passes through the coiled tungsten filament it glows and emits light. The manufacturing cost continued to fall, but the efficacy (ratio of light output to the input electric power) is around 18 lm/W limiting their application. A major portion of the energy (~90%) turns into the heat only just 10% of the energy emitted in the form of light [1,45,68]. Further, in the second generation, 90% artificially generated lighting originates from plasma discharge known as fluorescent lighting. The most common application of fluorescent lighting is the low-pressure mercury plasma with 75% conversion efficiency [69]. In general, the spectral energy distribution of plasma discharge strongly depends on the vapor pressure of the plasma gas inside the tube. In the low-pressure mercury discharge lamp, the vapor pressure amount is just few torr which gives the spectrum line at 185, 254 and 365 nm to excite the phosphor coating inside the tube. Fluorescent lamps are available in different shape and sizes such as fluorescent tubes, compact fluorescent lamps (CFL) with the varying efficiencies. However, CFL has an environmental disadvantage. Each CFL contains around 5 mg of mercury, which is very toxic and contains heavy metal poison. Therefore, it is essential to use low energy light bulb that does not contain mercury or other toxic materials [68]. High-pressure discharge lamps and low-pressure sodium lamps are also another option of lighting devices but due to long startup and cool down time their uses are limited in certain outdoor applications. Moreover, in the mercury-based fluorescent technology, there is some additional energy loss associated with the phosphor conversion of ultraviolet (UV) wavelength at 254 nm to visible luminescence [70]. CFLs are expected to be fixed the replacement incandescent lamps which will be available at reasonable cost with more efficient, nontoxic source of white light. Solid state lighting (SSL) is the emerging technology with the potential to surpass their luminous efficacy limitations and at the same time to introduce the new functionalities and design of lighting. Based on the semiconductor light emitting diodes (LEDs), SSL has made extraordinary progress in the past decade [44]. Nowadays, use of LEDs became a mature technology which can compete with the traditional incandescent and fluorescent lamps. They have abundant advantages over latter such as long lifetime, small size, robustness, fast switching and efficiency. It is well recognized that the replacement of incandescent lamps by higher efficiency light sources will lead

to the considerable reduction of worldwide electricity consumption. Figure 1.10 compares the spectra from a w-LED with an incandescent lamp. The heated filament radiates with approximately the Planck blackbody spectral distribution in incandescent lamp. Owing to the limit of the filament is operated, the peak output lies in the infrared at the wavelength of about 10^{-6} m and the spectrum across the visible range is abruptly sloped toward the red. However, the majority of the emitted radiation lies outside the human visual response [71].
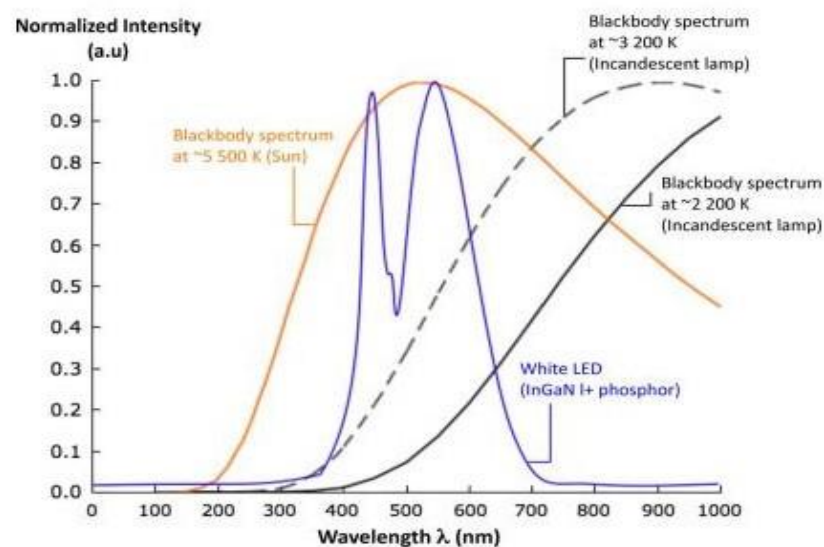
Figure 1.10. Normalized intensity graph for blackbody radiator at 5500 K (sun), 3200 K (warm white incandescent lamp), 2200 K (cooler white incandescent lamp) and for a w-LED (blue LED + phosphor).

As per the US Department of Energy roadmap, SSL expected 137 lm/W w-LED performance by 2020. In this new era of LED sources, the world has an opportunity for energy saving of about 1000 TW.h/year. This corresponds to an annual reduction of about 200 million ton of carbon emission with 100 billion/year savings [4]. The progress in w-LED efficiency with time, compared to the conventional light sources are shown in Figure 1.11. The cost and production of these LED lights are likely to decline, making them more economical with the development of solid state lighting technology. In order to estimate the suitable light source, a basic understanding of some performance parameters like efficacy, lifetime, correlated color temperature (CCT), color rendering index (CRI), Commission Internationale de l'Eclairage (CIE) color

coordinates, etc. are required. A brief description of the performance parameters is given below.
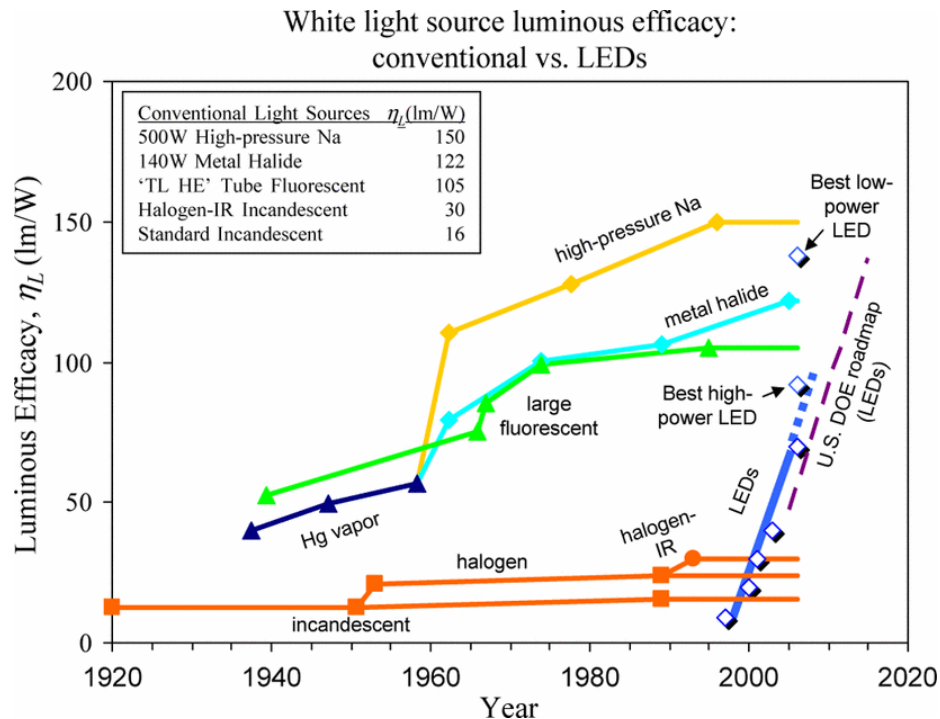
Figure 1.11. Evolution of luminous efficacy performance of white light sources [19].

1.8.1. Correlated color temperature (CCT)

Correlated color temperature (CCT) is defined as the absolute temperature of a blackbody whose chromaticity resembles the same color as that of the light source [5, 6]. As the temperature increases, hot objects will subsequently glow in red, orange, and yellowish white and bluish white. In simple, CCT explains a method of describing the color characteristics of light, usually implies low CCT warmer (more yellow- red) light while high CCT appears to be a colder (more blue) light, by measuring it in degrees Kelvin (K). Typical CCT of the white region diagram is in the range between 2000 and 10000 K [39].

1.8.2. Color rendering index (CRI)

The color rendering index (CRI or Ra) definition is based on comparing the color of test objects when illuminated by the light source under test, to the colors of the objects illuminated by a reference source such as natural light source/sunlight. When CRI is calculated, it can be rated on a scale from 0 to 100. The low CRI ratings suggested that less accurate color will be reproduced. A CRI of 100 would signify that

all color samples illuminated by a light sources and incandescent light source have high CRI since all colors in their spectrum are rendered equally [39].

1.8.3. CIE chromaticity coordinates

Commission Internationale de l'Eclairage (CIE) is the most widely used method to describe the composition of any color in terms of three primary color (red-green-blue). A color space is a three-dimensional space specified by a set of three numbers (tristimulus values *X, Y* and *Z*) which specify the color stored in the ratio of the primary color and not in the specific amount of the each individual primary color, the number of dimensions used to match the color of P(λ). The standard CIE 1931 *XYZ* color space specified by the two chromaticity coordinates known as x and y, creating the simple chromaticity diagram shown in Figure 1.12. The "horseshoe" curve consists of the chromaticity points of each color of light whose spectrum consists of only a single wavelength. All the colors of perceptible light have chromaticities represented by points inside the area bounded by the horseshoe. According to the chromaticity diagram, the primary colors red, blue and green are represented by (0.67, 0.33), (0.14, 0.08) and (0.21, 0.71) respectively. The CIE color coordinate of pure white light is (0.33, 0.33) [39,64].Further, the quality of white light was evaluated from the chromaticity coordinates using McCamy's relation,[72] by first evaluating ratio between inverse slope line and chromaticity epicentre as:

$$n = \frac{(x - x_e)}{(y - y_e)}$$

where x_e= 0.3320 and y_e =0.1858. Then the Correlated Color Temperature (CCT) was evaluated as:

$$CCT = -449n^3 + 3525\,n^2 - 6823.3n + 5520.33$$

The color purity or color saturation of a light source is the distance in the chromaticity diagram between the *(x, y)* color-coordinate point of the test source and the coordinate of the equal-energy point divided by the distance between the equal-energy point and the dominant wavelength point. The color purity is thus given by:

$$\text{Color purity} = \frac{\sqrt{(x-x_{ee})^2+(y-y_{ee})^2}}{\sqrt{(x_d-x_{ee})^2+(y_d-y_{ee})^2}}$$

where, *(x, y), (x_{ee}, y_{ee})* and *(x_d, y_d)* represent the chromaticity coordinates of the light source under test, equal-energy reference illuminant and dominant-wavelength point, respectively [39].
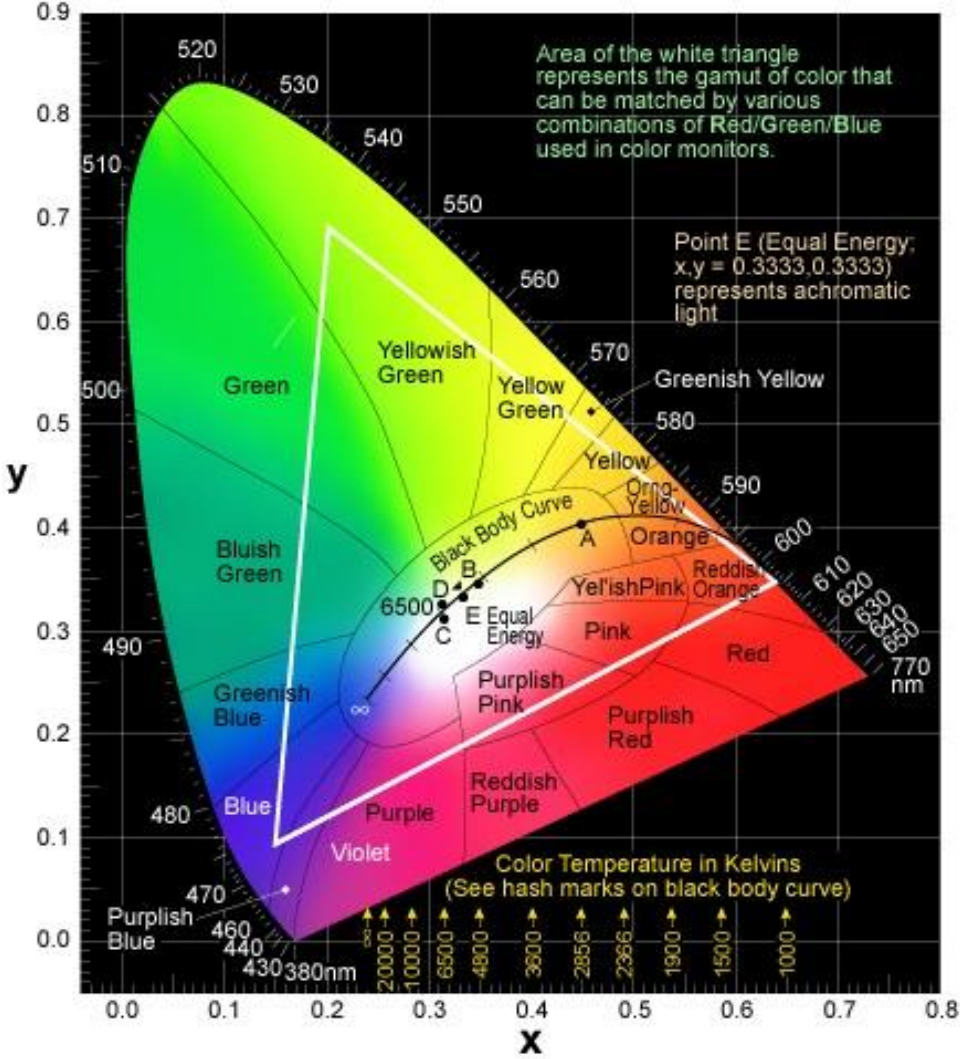
Figure 1.12. The CIE 1931 chromaticity coordinates.

1.8.4. Luminous efficacy

Luminous efficacy is a figure of merit of the light source. The luminous efficacy of a light source is governed by how much electrical energy is converted to light by the source and how well the human eye detects the emitted radiation. In another way, luminous efficacy determined as the ratio of the total luminous flux (lumen) to the power (watts) and expressed in lumen per watt (lm/w) [39,64].

A comparative analysis of various light sources in terms of their defining parameters are given in Table 1.4. This statistics proves the importance of LED light sources over other traditional light sources.

Table 1.4. Efficacy, lifetime, CCT and CRI of various light sources.

Light Source	Incandescent	Halogen	Compact Fluorescent	High-intensity discharge	White LED
Energy Efficiency	Very low	Low	High	High	Very High
Efficacy (lm/w)	7-20	15-25	60-100	65-110	90-120
Lifetime (hrs)	750-2000	2000-4000	9000-20000	5000-20000	>50000
CCT (K)	2400-3100	3000-3100	3000-6500	2900-5700	5000-6000
CRI	98-100	98-100	75-90	15-62	60-95
Heat	Yes++	Yes++	Yes	Yes	No
Mercury	No	No	Yes	Yes	No

1.9. Outline of the Host as a Phosphor

Phosphor materials consist of an inorganic compound in which performance mainly depends on the selection of suitable host and activator. The inorganic compound not only acts as a host material to hold the rare earth ions but act act as a sensitizer. In this pursuit, plenty of the materials are currently investigated as a host for rare earth dopants. Our attention has been focused on niobates in the present work.

1.9.1. History of Niobium

In 1801, Charles Hatchett found a new element in sample of mineral called as "Columbium" and now became famous element "Niobium." He named the "Columbite" for new element after the poetical name of America "Columbia". However, his findings were disputed because the element that Hatchett found actually was a mixture of Nb^0 and Ta^0. In 1846, Heinrich Rose argued that the mineral originally named as "Tantalite." Actually, this mineral contains Nb and Ta, and the confusion arose due to similar chemical properties between niobium and tantalum. Niobium was first used commercially in incandescent lamp filament in the 20th century and quickly became outdated by tungsten which has a high melting point [73]. Nowadays, a number of applications are emerging for niobates. These niobates and tantalates exhibit many interesting properties such as a solid electrolytic capacitor, catalysis, photochromic devices, transparent oxides, etc. Few alkali, and alkaline earth niobates have been examined for their potential application in the field of science and technology. The alkali earth niobates $LiNbO_3$, $KNbO_3$, $KTaO_3$ and $NaNbO_3$, classified as perovskite have been reported for interesting properties such as piezoelectricity, electro-optic, nonlinear optical behavior in the field of photonics, frequency doubler, holographic storage and microwave dielectrics [74,75].

1.9.2. Alkaline earth niobates

In the alkaline earth niobates, pyro and ortho such as $Ca_2Nb_2O_7$, $Sr_2Nb_2O_7$, $Mg_4Nb_2O_9$ $SrNbO_3$, $BaNb_5O_{15}$, and $Ba_5Nb_{12}O_{35}$, etc., have been studied for their luminescent properties along with other properties. According to Wachtel [76] and Blasse [77], the luminescent properties of inorganic compounds containing niobium oxygen complex (NbO_6) are structurally sensitive as the absorption edge of the niobates is due to charge transfer that occurs within this complex. The alkaline earth niobates have the general formula $A^{2+}Nb_2O_6$, where A^{2+} is a divalent cation of Mg, Ca, Sr, Ba or transition metal such as Cu, Cd, Zn, Ni, Mn, Co or Fe) and known as meta-niobates. They are the subcomponent of the complex perovskite family, $M(A_{1/3}Nb_{2/3})O_3$ and mostly exists in an isostructural form of an orthorhombic structure with columbite mineral group except the A= Sr, Ba and Pb analogues, which crystallizes in different structures [78]. Pullar [79] has been specially mentioned the microwave dielectric ceramics along with magnetic, catalytic and excellent optical of these niobates.

Moreover, rare earth doped alkaline earth niobate phosphors have attracted much attention of the researcher due to their advantages such as high chemical and thermal stability than other phosphates, borates, vanadates, etc. [80]. Moreover, they have been used in LEDs and plasma display panel (PDP) applications. In the present work, $BaNb_2O_6$ has been selected as the host material due to enrich a class of stable structure (orthorhombic).
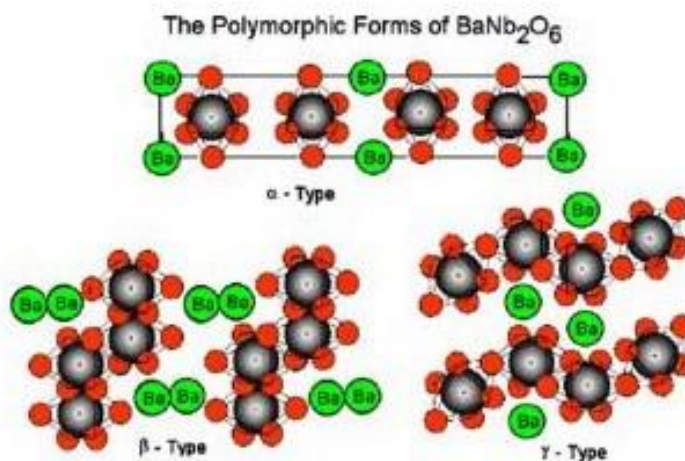
Figure 1.13. Isomorphic structure of $BaNb_2O_6$.

$BaNb_2O_6$ is polymorphic and has five different crystal structures. Among five, three are exhibit unique meta-niobate and other two are isomorphous to ferrate ($NdFeO_6$) and tantalite ($BaTaO_6$). The three isomorphic structure of $BaNb_2O_6$ are shown in Figure 1.13. The symmetry of the crystal is an orthorhombic and the corners nearly 60° and 120° angles to form a ring of six octahedra. The barium atom is situated in the cages formed by the rings [73]. $BaNb_2O_6$ considered as one of the most promising ferroelectric materials. Moreover, rare earth activated $BaNb_2O_6$ may be an excellent phosphor material for solid state lighting applications due to its high thermal and chemical stability. However, the best of our knowledge, no one has reported on the rare earth doped $BaNb_2O_6$ phosphors to generate white light based on the proposed approaches in the present work. Therefore, rare earth doped alkaline earth niobates along with strong n-UV and blue absorption are expected to be used as a potential white phosphor under different excitation wavelengths, which has been motivated me to carry out this present research work.

1.10. Objectives of the Thesis

The research on SSL-based w-LED has grown unbelievable in the past decade due to their inherent advantages. In the present work, attempts are made to synthesize rare earth activated $BaNb_2O_6$ phosphors with improved luminescent properties and finally to examine the approaches/methods to generate white light and also multicolor emission from $BaNb_2O_6$ phosphor upon n-UV and blue LED excitation. Moreover, the main focus would be given for the enhancement of luminescence in rare-earth doped $BaNb_2O_6$ phosphor through different synthesis procedures and after that optimizing the activator doping concentration. Also, thermal, structural and morphological properties of rare earth doped $BaNb_2O_6$ would be investigated. Thus, the discussion made in the previous sections and motivated by the above facts, the short term specific objectives of the thesis are as follows:

(i)   To synthesize single phase rare earth doped $BaNb_2O_6$ phosphors by using solid state reaction method to achieve required optimum structure and phase.

(ii)   To study the thermal, structural and morphological properties of the synthesized phosphors.

(iii)   To optimize the luminescence properties in the visible region and absorption in the n-UV region to obtain efficient white light and multicolor emission.

(iv)   To enhance the photoluminescence properties in rare earth doped $BaNb_2O_6$ phosphors by SSR (adding chloride flux) and MCG method and compare its photoluminescence characteristics to know the better luminescence.

(v)   To evaluate the CIE chromaticity color coordinates (x, y) and correlated color temperature (CCT) from the photoluminescence spectra of the prepared phosphors.

(vi)   Finally, to estimate the feasibility to generate white light from rare earth doped $BaNb_2O_6$ phosphor for solid state lighting applications.

2

Synthesis and Characterization

The development of high quality material requires adequate knowledge on the various synthesis methodologies along with the relevant characterization techniques. The purpose of this chapter is to explain the synthesis methods adopted in the present work. The structural, morphological, photoluminescent properties of the synthesised powder phosphor samples have been characterized using various analytical tools such as X-ray diffraction (XRD), scanning electron microscopy (SEM), field emission scanning electron microscopy (FE-SEM), UV-Vis spectrophotometer and spectrofluorophotometer etc. The working principles and experimental tools used in the current work are also explained in this chapter.

Synthesis and characterization

2.1. Synthesis Routes

There are various synthesis techniques described in the literature for the preparation of phosphors and nanophosphors. These include well known solid state reaction method, sol-gel, metal citrate gel, co-precipitation, hydrothermal, combustion, spray pyrolysis, and combinatorial chemistry method. It is well known that the performance of materials is closely related to morphology, particle and grain size distribution i.e. the ways in which they are processed. The synthesis method plays a significant role in determining the microstructure, luminescence properties, and quantum efficiency of the phosphors [80]. The conventional solid state reaction is used via grinding or milling technique for the fine-grained luminescent material. This method has some drawback, which can introduce defects in the materials. Defect have some serious implications for luminescent materials as they provide non-radiative recombination. The wet chemical synthesis is essentially required to synthesize small, dispersed, uniform shaped particle size. The drawback of these methods are complicated chemical procedures with high cost and small production volume. Among wet chemical processes, metal citrate gel synthesis is preferred and very suitable for the mass production [81]. In the current research work, emphasis has been given on two promising techniques such as solid state reaction (SSR) and metal citrate gel (MCG) method, in order to investigate and optimize the methodology that result in the formation of most efficient phosphors. Figure 2.1 (a-d) shows the step by step procedure of wet chemical methods: metal citrate gel, co-precipitation, hydrothermal and combustion synthesis, respectively. A brief description of the various synthesis techniques and their relative advantages and limitations are described in Table 2.1.

Table 2.1. Comparison of synthesis methods in terms of the particles size, morphology, homogeneity, time, cost, suitable phosphors and limitations [82].

Synthesis methods	Solid state reaction (SSR)	Metal citrate gel (MCG)	Co-precipitation (CP)	Hydrothermal (HT)	Combustion synthesis (CS)	Spray pyrolysis (SP)
Particle size	>3 µm	10 nm - 3 µm	10 nm -1 µm	10 nm -1 µm	500 nm -3 µm	100 nm -2 µm
Morphology	Bad	Medium	Good	Medium	Medium	Very good
Homogeneity	Bad	Good	Good	Good	Medium-good	Medium-good
Cost	Low	Medium	Medium	High	Low	Medium
Synthesis time	Long	Medium	Medium	Long	Short	Short
Suitable phosphors	All compounds	All compounds except nitrides	Oxides and fluorides compounds	All compounds	All compounds except nitrides	All compounds except nitrides
Limitations	• Extensive grinding and milling required	• Requires a soluble precursor • Carbon contamination • Difficult to obtain for nitrides, sulfides, other non-oxide materials	• Requires a soluble precursor • Difficult to obtain for nitrides	• Requires a soluble, precursor • Special equipment needed	• Requires a soluble precursor • Carbon contamination • Difficult to obtain for nitrides.	• Requires a soluble precursor • Difficult to obtain for nitrides and other non-oxide materials
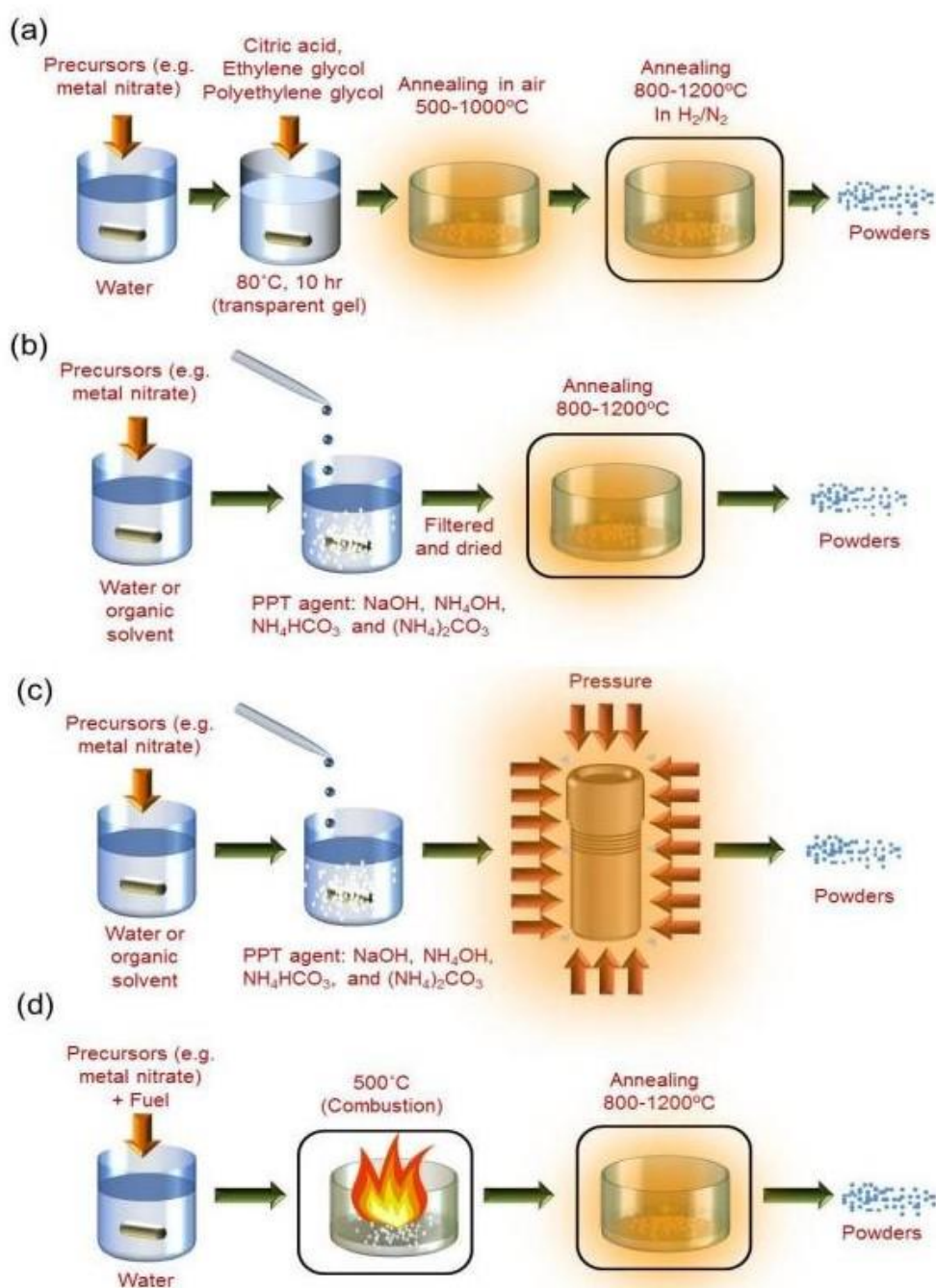
Figure 2.1. Schematic diagram of wet chemical syntheses (a) Metal citrate gel (b) Co-precipitation (c) Hydrothermal (d) Combustion synthesis.

The present thesis is mainly focussed on two synthesis techniques as given below:

2.1.1. Solid state reaction (SSR) method

The solid state reaction is extensively used to synthesize inorganic materials because of its facile operation. This method is the widely used for the preparation of

almost all kinds of oxides, (oxy)nitrides, (oxy)chlorides, (oxy)halides and (oxy)fluorides based phosphors, which is straight forward and suitable for mass production [83]. This synthesis is usually carried out at high temperatures (i.e. 1200–1800 °C). The thermodynamic point of view, the reaction: $AO\ (s) + B_2O_3 \rightarrow AB_2O_4$ may complete at high temperature. Under certain conditions of high temperature, the reaction can proceed at the crystal boundary of AO and B_2O_3 crystallites and form a product layer of spinal type AB_2O_4. The first stage of this reaction is to form nuclei of AB_2O_4 crystallites at the crystal lattice of the reactants, or adjacent to, their boundary. The nucleation reaction is not easy since the nuclei are from different reactants and are different in structure. Therefore, nucleation needs to go through structural rearrangement, including breaking the cation-anion bonds of reactant molecules, releasing, diffusing, and repositioning of A^{2+} and B^{3+} ions in the crystal lattice. A high temperature favors all these processes and thus nucleus formation occurs. Similarly, the growth of nucleus is also quite difficult. A^{2+} and B^{3+} ions in the reactants need to diffuse through two boundaries (Figure. 2.2) to grow on the nucleus to thicken the product layer. It is obvious that the controlling step of the reaction is the diffusion of A^{2+} and B^{3+} ions, which is favored by an increase in temperature. On the other hand, the reaction rate decreases with the thickening of the product layer [64].
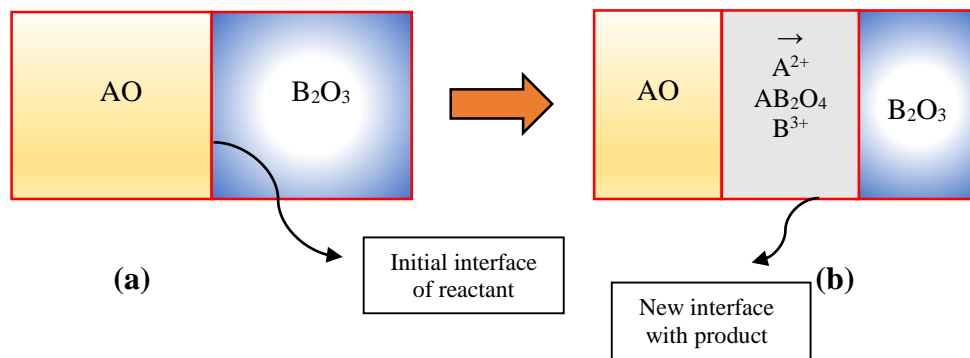
Figure 2.2. Schematic diagram of reaction mechanism of oxide materials.

Moreover, in some cases a controlled atmosphere is required for command over the valence of the activator and the stoichiometry of the host lattice in the preparation of material doped with rare earth oxides. The particle size of the phosphor prepared by this method is relatively large and uncontrollable. There are several limitations in the synthesis of phosphors prepared by a conventional solid state method. Firstly, this process requires high calcination temperatures. Secondly, the grain size of the phosphor

powders prepared by this method is several tens of micrometres. Furthermore, the average particle size of the phosphors prepared by this method is often larger than 5 μm, making light scattering an issue for integration with a n-UV chip [64].

In the current study, rare earth doped $BaNb_2O_6$ have been synthesized by using high purity chemical precursors $BaCO_3$ (Fisher Scientific, 99%), Nb_2O_5 (Junsei Chemical Co. Ltd., 99.9%) as starting materials. Corresponding rare earth oxides as dopants or chlorides as fluxes have been used on the requirement of applications and availability. In the present work, Dy_2O_3, Sm_2O_3, Eu_2O_3 (Sigma Aldrich, 99.9%) have been used as doping materials to obtain the Dy^{3+}, Sm^{3+} and Eu^{3+} doped $BaNb_2O_6$ phosphors.
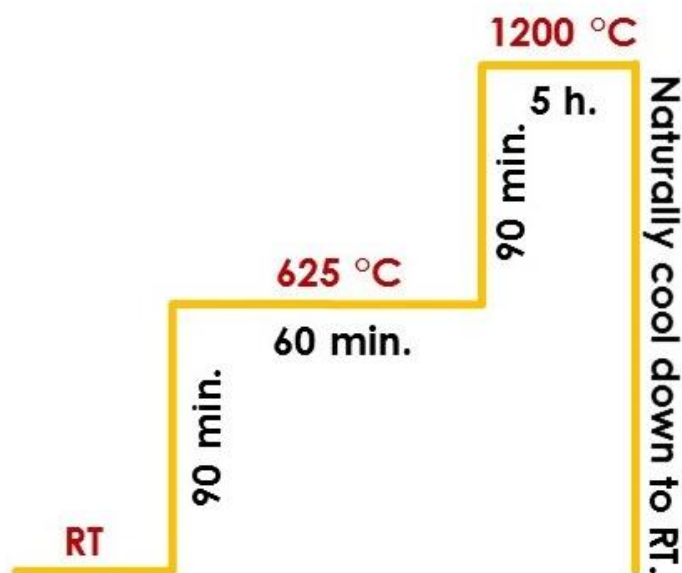
Figure 2.3. Heat treatment procedure for RE^{3+} doped $BaNb_2O_6$ phosphors.

The required amount of these starting materials were weighed stoichiometrically and ground in an agate mortar pestle for an hour with acetone as dispersing medium. The well ground mixture was taken in alumina crucible and placed inside the muffle furnace in two step heating process based on the results obtained from the thermogravimetric (TGA) and differential scanning calorimetry (DSC). Rare earth doped $BaNb_2O_6$ phosphors were obtained by sintering at different temperatures, firstly at 625 °C for 1 hour and then at 1200 °C for 5 hours as shown in Figure 2.3.

The synthesis process followed in the present work is given in Figure 2.4 by using conventional solid state reaction method.
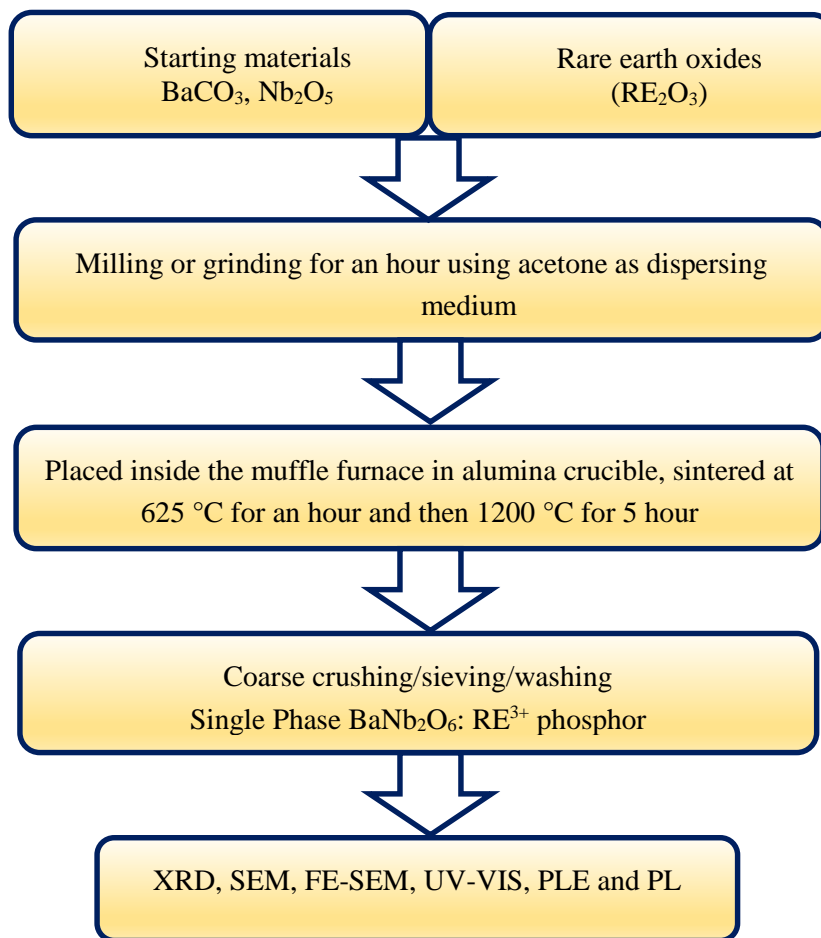
Figure 2.4. Schematic illustration of phosphor synthesis procedure by SSR method.

2.1.2. Metal citrate gel (MCG) method

An intense level of research activity has been carried out on the development of luminescent materials by metal citrate gel (MCG) method. This is also known as sol–gel combustion method [84]. Figure. 2.1(a) represents the basic production cycle for MCG method. Metal oxides are dissolved in nitric acid solution in the appropriate molar ratios (which is less costly than metal nitrate powders). Citric acid is uses as a chelating agent then added along with ethylene glycol/polyethylene glycol (cross-linking agents). Further, ammonia solution is used to maintain the pH value [85–87]. The solution is stirred at temperatures, usually below 150 °C, which produces a transparent gel. The gel is calcined at low temperature (~500 °C) to remove organics and residual water, resulting in a nanocrystalline powder. The particle size and morphology can be controlled by varying the solvent and heating conditions, or by changing the precursors. Various type of single phase materials can be simply synthesized by this method,

without any extensive grinding and milling. However, the phosphors can be contaminated with carbon due to the use of organic reagents and thus a pre-annealing step in air atmosphere is required. Sometimes, a reducing atmosphere may be required to obtain Eu^{2+} and Ce^{3+} activated phosphors [88,89].

In the Chapter 6 of present thesis, fine nanophosphors of Eu^{3+} doped $BaNb_2O_6$ were synthesized by a facile MCG method. High purity (>99.9%) Barium nitrate $(BaNO_3)_2$, Niobium Chloride $(NbCl_5)$, Europium oxide (Eu_2O_3), Citric acid $(C_6H_8O_7 \cdot H_2O)$, and Hydrogen Peroxide (H_2O_2) were used as the starting materials. The synthesis procedure is shown in Figure 2.5.
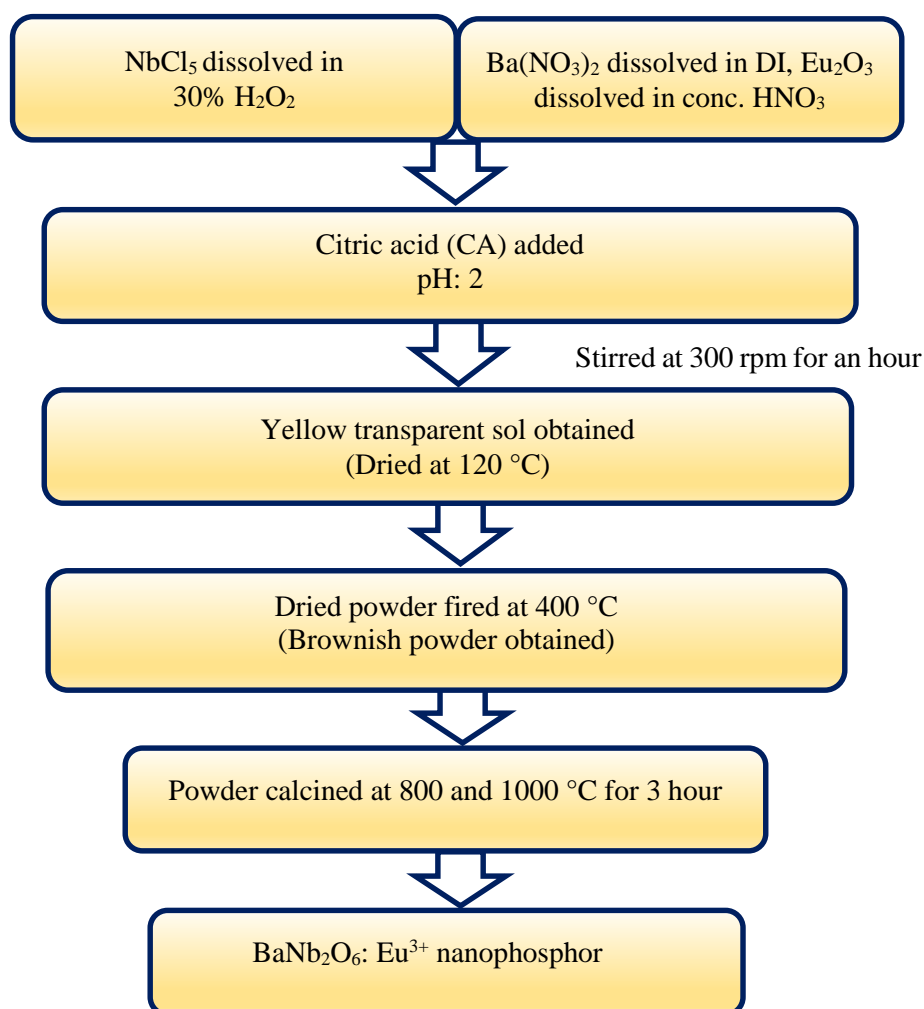
Figure 2.5. Flow chart representing the processing steps of metal citrate gel method.

The stoichiometric amount of $NbCl_5$ dissolved in 30% H_2O_2 aqueous solution. $(BaNO_3)_2$ and Eu_2O_3 were dissolved in deionized (DI) water and minimum amount of concentrated nitric acid, respectively. All the metal nitrates chloride solution were

mixed by continuous stirring at 300 rpm then the citric acid was introduced in that solution in the molar ratio of 1:3 (metal: nitrate). The solution was agitated using magnetic stirrer for further 45 min to obtain a transparent homogeneous solution, at this stage, pH was 2.0. In next step, the solution was dried at 120 °C on a hotplate to evaporate the water. As the water evaporated slowly from the solution, a yellowish colored colloidal suspension was formed and then the bulk of thick brown gel product with high viscosity obtained. Subsequently, the gel was fired at 400 °C for 1 hour then further ground and sintered at different temperatures to obtain the pure phase of $BaNb_2O_6$ powder.

2.2. Characterization of Luminescent Materials

The characterization of materials is very important parameter for any synthesized samples. The crystallinity and phase identification of phosphors are analysed by using powder X-ray diffraction (XRD). The morphology and particle size were examined using scanning electron microscopy (SEM) and field emission-scanning electron microscopy (FE-SEM). Optical band gap, photoluminescence (PL) and lifetime were measured by using UV-Vis spectrophotometer and spectrofluoro-photometer, respectively.

2.2.1. Thermal analysis

When the matter/substance is heated, it goes under certain physical and chemical changes. Physical changes includes phase changes such as vaporization, transition, crystallization, adsorption, absorption or desorption of gases. Chemical changes include reactions to form new compound via oxidation, corrosion, decomposition, dehydration and binding between compounds. This physical and chemical changes takes place over a wide temperature range. It is necessary to characterize materials to reveal their behaviour over a range of temperature to determine at which temperature range material or chemicals can withstand without changing. The analytical technique used to study changes in physical properties of any substance with temperature is called thermal analysis technique. Usually, the substance is subjected to a controlled temperature program during the analysis. Although there are many thermal analysis techniques, we confine our discussion in this thesis to two

methods which have been used in present thesis. These methods are thermogravimetric analysis (TGA) and differential scanning calorimetric DSC.

2.2.1.1. Thermogravimetric analysis (TGA)

In the thermogravimetric analysis technique, the mass of a substance is measured in controlled atmosphere and recorded continuously as a function of temperature of time. In contrast, the temperature of the sample increases linearly with time. The obtained curve of mass or mass percentage as a function of temperature known as thermogram or a thermal curve and its first derivative is called derivative thermogram [90]. The changes in weight of a sample with change in temperature gives information about the temperature at which the material loses or gains weight. Loss of weight indicates the decomposition or evaporation of the sample. A gain in weight can indicate adsorption by the sample in the atmosphere or chemical reaction with the atmosphere such as oxidation. The temperature at which no weight changes takes place indicates the temperature stability of material [91].

Thermogravimetry has several applications such as determining the composition of multicomponent systems, adsorption and desorption of gases, thermal stability of materials, kinetics of decomposition processes, oxidation reactions and oxidation stability, roasting and calcinations of minerals, determination of curie temperature, sorption and desorption of moisture and volatiles content of materials, the level of inorganic and organic components in materials and estimated lifetime of the product etc.

2.2.1.2. Differential scanning calorimetric (DSC)

Differential Scanning Calorimetry (DSC) is a thermoanalytic technique, similar to differential thermal analysis (DTA). The basic difference between the DSC and DTA is that DSC is a calorimetric method in which difference in energy is measured. In contrast, differences in temperature are recorded in DTA. DSC monitors the difference in the temperature between a sample and a reference material as a function of time and temperature in a specific atmosphere. Qualitatively measures heat absorbed or released by a material undergoing a physical or chemical change. DSC helps in determining the exothermic (ΔH negative) and endothermic events (ΔH positive) occurring in the

sample with temperature variation [90,92]. DSC is used in measuring a glass transition, phase change, purity evaporation, melting, purity crystallization, sublimation, polymerization, heat capacity, compatibility, pyrolysis, etc. TGA-DSC apparatus consists of a sample holder comprising thermocouples, sample containers and ceramic or metallic block, temperature programmer, furnace, and recording system. The key feature is the existence of two thermocouples connected to a voltmeter. One thermocouple is placed in an inert material such as Al_2O_3, while the other is placed in a sample of the material under study. As the temperature is increased, there is a brief deflection of the voltmeter if the sample is undergoing a phase transition. Operating temperatures are generally within the range of room temperature to about 1400 °C (melting temperature). In the present thesis, TGA-DSC measurements were carried out using the instrument Mettler-Toledo Stare e and NETZSCH as shown in Figures 2.6 (a) and (b), respectively.
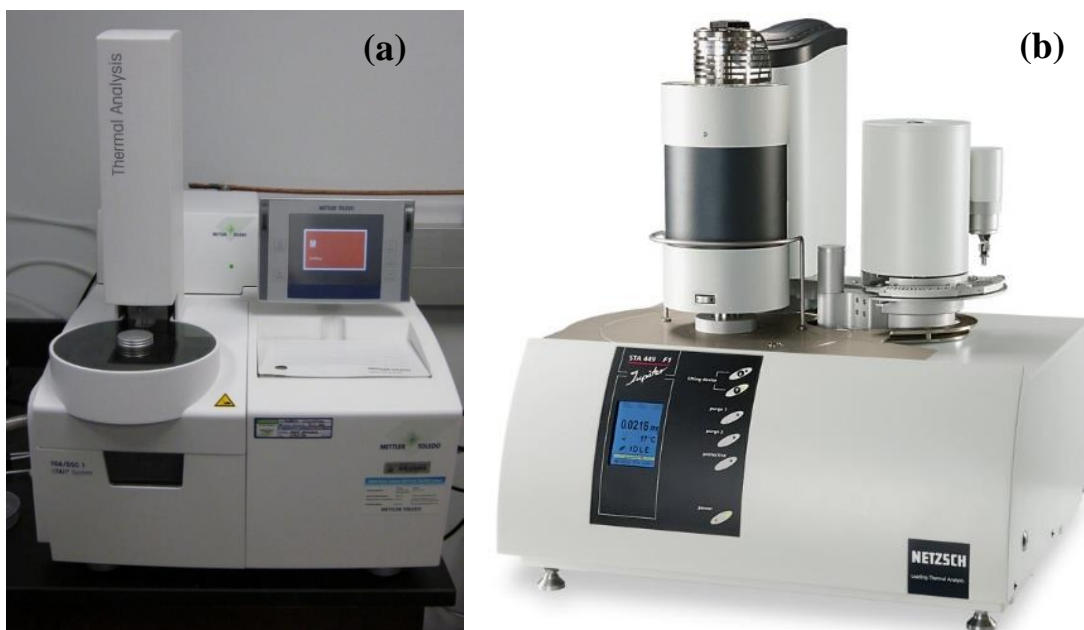
Figure 2.6. **(a)** Mettler-Toledo made thermogravimetric analysis (TGA)

(b) NETZSCH manufactured differential scanning calorimetry (DSC).

2.2.2. Powder X-ray diffraction

X-ray diffraction (XRD) is a very powerful technique used to identify the crystalline phase present in material and to measure the structural properties such as strain, stress, crystallite size, epitaxy, phase composition, preferred orientation, and

defect structure of these materials. XRD is also used to determine the thickness of thin films and multilayer and atomic arrangements in amorphous materials (including polymers) [64].

X-ray diffraction techniques are based on observing the scattered intensity of an X-ray beam hitting a sample as a function of incident and scattered angle. X-ray diffraction is based on constructive interference of monochromatic incident X-ray and a crystalline sample and X-rays. The positions of the diffraction peaks are determined by using the spacing of the crystallographic planes in the following Bragg's law [93]:

$$(n\lambda = 2d \sin \theta)$$

where n is an integer, λ is the wavelength of the X-ray source which is equal to 1.5406 Å, d is the spacing of the crystal planes and θ is the glancing angle. The XRD pattern of each crystalline material is unique. Typically, the identification of the compounds is achieved by comparison of d-spacing with standard reference patterns. X-ray diffractometers consist of three basic component (i) X-ray tube, (ii) Sample holder, and (iii) X-ray detector which is illustrated in Figure 2.7.
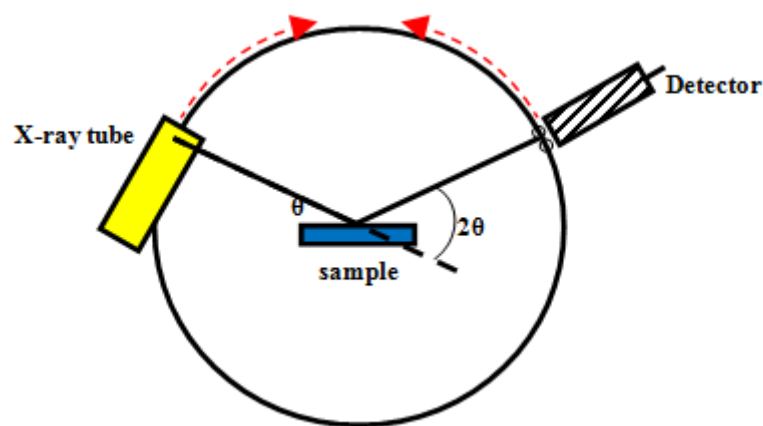
Figure 2.7. Schematic representation of X-ray diffraction method.

X-ray diffraction offers unparalleled accuracy in the measurement of atomic spacing and is the technique of choice for determining the strain in the materials. XRD is non-contact and non-destructive which make it ideal for in-situ studies. The intensities measured in XRD can provide the quantitative accurate information on the atomic arrangements at interfaces. Materials composed of any element can be successfully studied with XRD, but XRD is most sensitive to high Z-elements, since

the diffracted intensities from these are much larger than from low Z elements. As a consequence, the sensitivity of XRD depends on the material of interest.

X-rays are generated in a cathode ray tube by heating a filament to produce electrons, accelerating the electrons towards a target by applying a voltage, and bombarding the target material with electrons. When electrons have sufficient energy to displace inner shell electrons of the target material, characteristic X-ray spectra are produced. These spectra consist of several components, the most common being K_α and K_β. K_α consist in part of $K_{\alpha 1}$ and $K_{\alpha 2}$. $K_{\alpha 1}$ has slightly shorter wavelength and twice in the intensity as $K_{\alpha 2}$. The specific wavelength are characteristics of the target material (Cu, Fe, Mo, Cr). Filtering, by foils or crystal monochromators, is required to produce monochromatic X-rays needed for diffraction. $K_{\alpha 1}$ and $K_{\alpha 2}$ are sufficiently close in wavelength such that a weighted average of the two is used. Cu is the most common target material for single-crystal diffraction, with Cu-K_α radiation of 1.5406 Å. These X-ray are collimated and directed onto sample. As sample and detector are rotated, the intensity of the reflected X-rays is recorded. The geometry of an X-ray diffractometer is such that the sample rotates in the path of the collimated X-ray beam at angle θ, while the X-ray detector mounted on an arm to collect the diffracted X-rays and rotates at an angle of 2θ. The instrument used to maintain the angle and rotate the sample is termed a goniometer [94].

Figure 2.8. Bruker D8 Advance X-ray diffraction machine.

For typical powder pattern, data is collected at 2θ in various angles that are present in X-ray scan. When the geometry of incident X-rays impinging on the sample satisfies the Bragg equation, constructive interference occurs and a peak in intensity occurs. A detector records and processes this X-ray signal and converts the signal to a count rate which is then output to a device such as a printer or a computer monitor. Peak positions occur, where the X-ray beam has been diffracted by the crystal lattice. Figure 2.8 represents the Bruker made D8 advance X-ray diffractometer.

2.2.3. Rietveld analysis

The Rietveld method refines user-selected parameters to minimize the difference between an experimental pattern (observed data) and a model based on the hypothesized crystal structure and instrumental parameters (calculated pattern). Refinement of the crystal structure can be carried out from the data obtained from spectra using Rietveld analysis. This method was developed by Hugo Rietveld which uses least squares approach to refine a theoretical line profile until it matches the measured profile [95,96]. A number of parameters like background, peak shape, lattice parameters can be refined using a Rietveld refinement software such as Full Prof Suite, PANanalytical X'Pert HighScore Plus etc.

The X-ray powder diffraction patterns in the present thesis were measured using a Bruker D8 Advance and Rigaku MiniFlex-II. The diffractometer was equipped with a Ni filtered Cu - Kα source (λ =1.5406 Å) and was operated at 40 kV and 30 mA. The diffraction peaks were recorded in the 2θ range from 20° to 60° at room temperature. Rietveld refinement of the samples was carried out using Full Prof Suite.

2.2.4. Scanning electron microscopy (SEM)

The scanning electron microscope (SEM) is one of the most versatile instruments available for the examination and analysis of the microstructural characteristics of solid objects. SEM permits the observation and characterization of heterogeneous organic and inorganic material on nanometer (nm) to micrometer (μm) scale. This is a type of electron microscope that can image and analyse the bulk specimens sample surface by scanning it with a high energy beam of electrons. A major reason for the SEM's usefulness is the high resolution which can be obtained when bulk

objects are examined. The principle of SEM is based on the interaction of an incident electron beam and the solid specimen. As the beam strikes the sample it creates various signals (secondary electrons, back-scattered electrons and auger electrons etc.), all of which can be appropriately detected. Using these signals an image is being recreated on the display screen. The SEM can also be used to provide crystallographic information along with the grain structure (fracture surfaces, etched, or decorated surfaces), size and shape. Figure 2.9 shows a schematic of a simple scanning electron microscope. SEM consists of three distinct parts: an electron column, a detection system, and a viewing system. There are two basic types of electron guns in current use: (i) thermionic electron gun and (ii) field emission electron gun. The diameters of the electron beam originating from these gun types are about 20-50 μm and 10 nm, respectively. Two electron beams are controlled simultaneously by the same scan generator: one is the incident electron beam and the other is for the cathode ray tube (CRT) screen. The beam is defocused by a series of magnetic lenses as shown in schematic diagram of Figure 2.9.
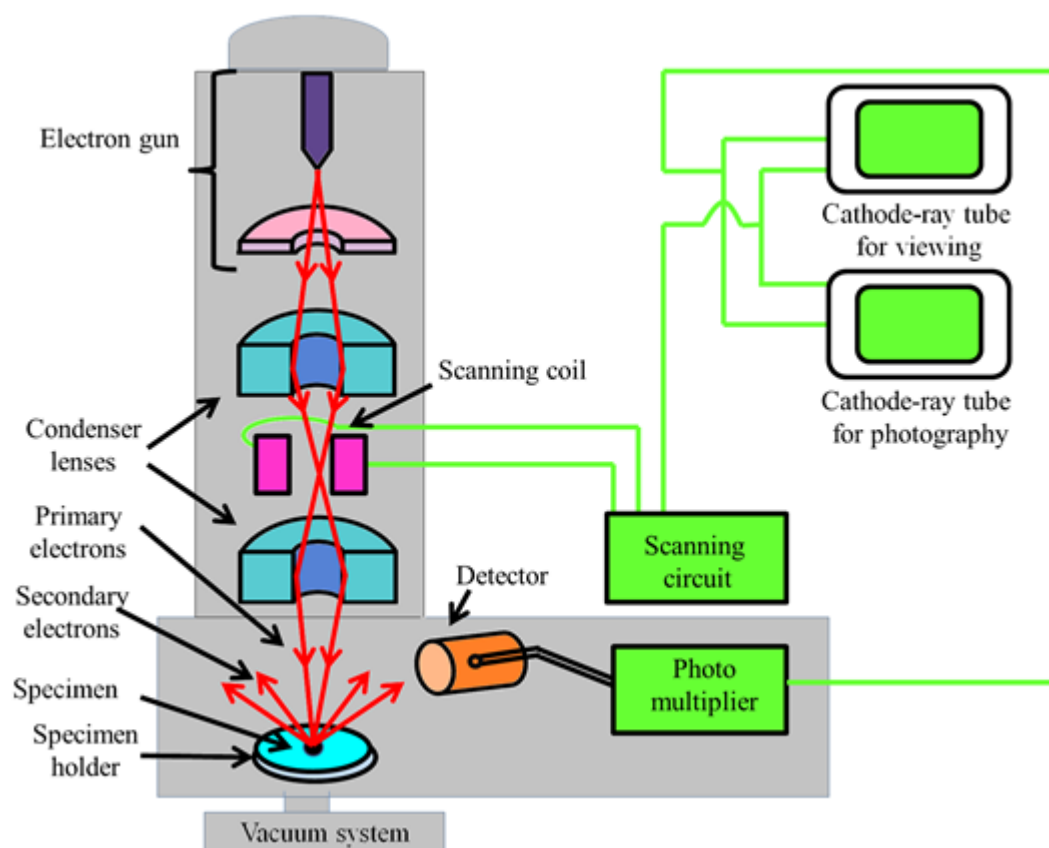
Figure 2.9. Schematic diagram of SEM showing basic components.

The focal length is controlled by increasing the current through the condenser lens. Electronic devices amplify the signals produced and display them in the form of high resolution images on the CRT screen. Specimens used in SEM analysis, should be conducting so that the electrons have a path to the ground. Non-conducting samples are made conducting by coating them with a suitable metallic layer of gold or carbon using low vacuum sputter coating or high vacuum evaporation [90].

The SEM analysis of the samples in the present study were carried out using Hitachi S-3700N. The resolution of SEM was 10 nm at 30kV with magnification varying between 5x-3,000,000x. A photograph of the same has been presented in Figure 2.10.

Figure 2.10. Hitachi S-3700N Scanning electron microscopy.

2.2.5. UV-Vis spectroscopy

UV-Vis absorption spectroscopy is analytical and important tool to understand the optical properties of materials which involves absorption of UV/Visible light by a molecule causing the excitation of an electron from ground to excited electronic state. UV-Vis absorption spectrum is a plot of degree of absorption of a sample against the wavelength of the incident radiation. It may include both broad and sharp lines of

absorption. A typical spectrophotometer set up for UV-Vis absorption is shown in Figure 2.11. In absorption spectroscopy, the photon energy of the radiation incident on the sample is selected by a scanning monochromator. The radiation selected by the monochromator is passed through a rotating disc that alternately directs the radiation along a reference beam path (going through reference cell) and through a path containing the sample (sample cell). One detector alternately records the signals from both beam paths. Absorbance may be presented as transmittance ($T(\lambda) = I(\lambda) / I(\lambda_0)$).
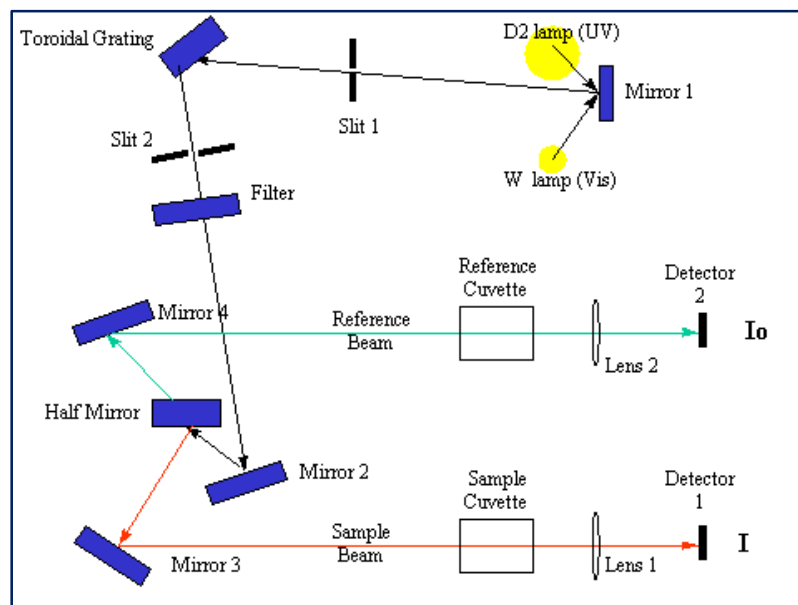
Figure 2.11. Schematic working diagram of UV-Vis spectrophotometer.

The transmittance $T(\lambda)$ is defined as the ratio of the intensity of the light passed through the sample $I(\lambda)$ to the intensity of the reference signal $I(\lambda_0)$. In a transmission spectrum, T is plotted as a function of wavelength (or an equivalent parameter). Instead of transmittance, the absorbance or optical density (A), is often the quantity plotted on the y - axis. Absorbance of the sample is related to the transmittance by the equation

$$A = - \log_{10}(T)$$

Absorption spectroscopy is used to measure the transmitted signal for transparent (non-scattering) samples such as single crystals or solutions. In case of solid or polycrystalline samples there is an alternative technique available known as diffuse reflection spectroscopy. Reflectance, which is the base quantity that characterize the process of reflection, is defined as the ratio of the reflected radiant flux (or power) to the incident radiant flux (or power). Generally, the reflectance of the powder at any

wavelength can be considered to be the sum of specular reflectance and diffuse reflectance [97]. The difference in setup for absorption and reflection spectroscopy is in the detection compartment. When diffuse reflection spectroscopy is used, the backscattered signal is detected and compared to the backscattered signal from a reference material [16]. Polycrystalline powders of MgO or $BaSO_4$ can be used as a reference. The reflectance (R) is plotted on the y - axis and is defined as

$$R = I/I_0(\lambda)$$

where I is the intensity of reflected light and I_0 is the intensity of incident light. The schematic representation of diffuse reflectance is shown in figure 2.12.
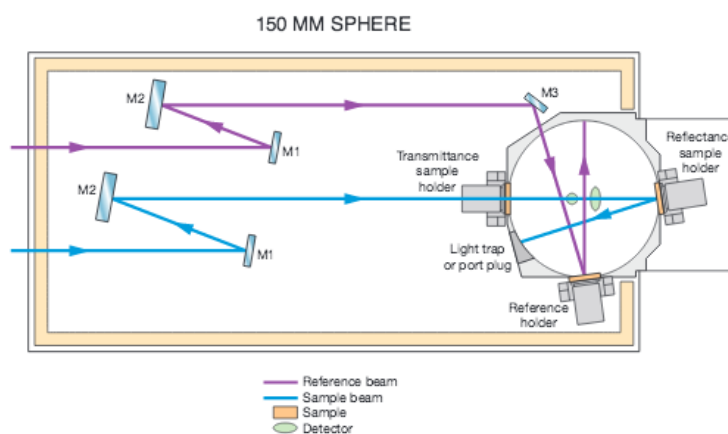
Figure 2.12. Schematic representation of diffuse reflectance spectroscopy.

In the present study, the diffuse reflectance sprectra was carried out using Agilent Technologies, Cary 300 UV-Vis-NIR spectrophotomer fitted with integrating sphere. Barium sulphate was used as a reference.

2.2.6. Photoluminescent spectroscopy

The luminescence properties of a phosphor can be characterized by its emission spectrum, brightness, and decay time. Photoluminescence is often referred to as fluorescence spectrometry or fluorometry specially when applied to molecules systems. Photoluminescence is advantageous in many fields, including environmental research, pharmaceutical and food analysis, forensics, pesticide studies, medicine, biochemistry, and semiconductors.

Photoluminescence (PL) is the spontaneous emission of light from a material under optical excitation. The photoluminescence substance absorbs radiation of a certain wavelength and then re-emits the photon at different wavelengths. It is a contactless, non-destructive method of probing the electronic structure of materials. Light is directed on to a sample, where it is absorbed and imparts the excess energy in to material in a process called photo-excitation. Photo-excitation originates due to electrons within the material to move in the permitted excited states.
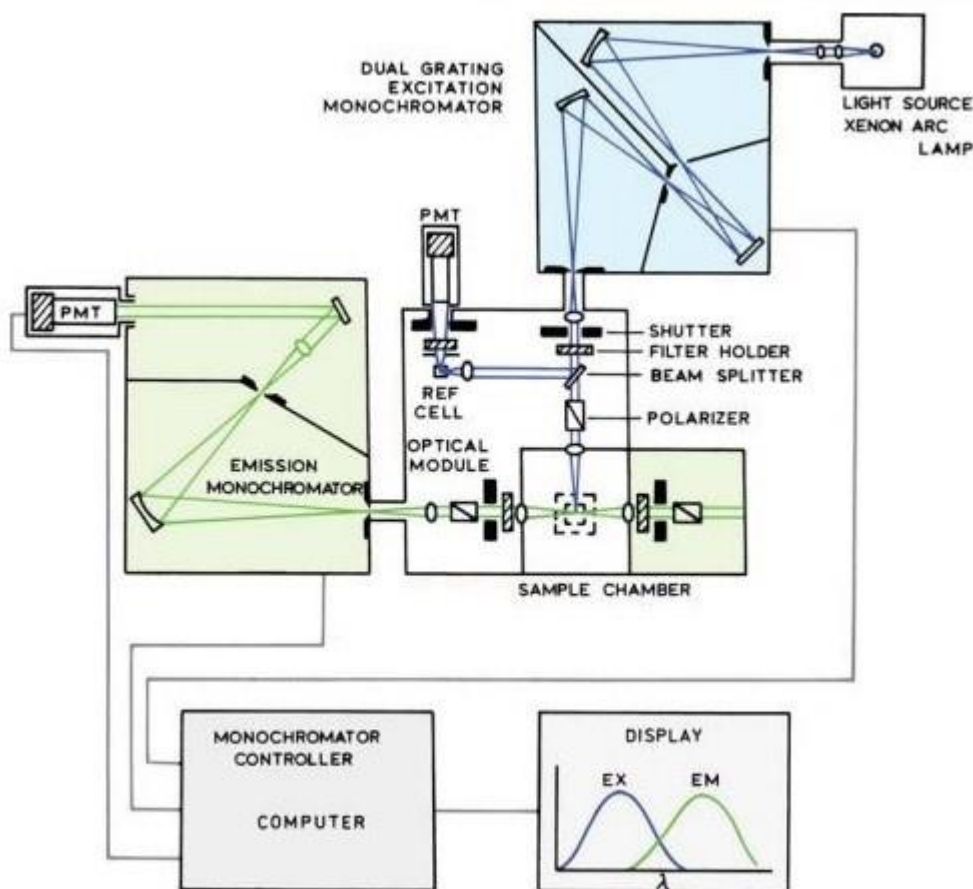
Figure 2.13. Schematic diagram of spectrofluorphotometer.

When these electrons return to their equilibrium state, the excess energy is released either in form of light (a radiative transition) or in form of heat (non-radiative process). The energy of the emitted light (photoluminescence) relates to the difference in energy levels between the two electronic states involved in the transition between the excited state and equilibrium state [98].

A typical configuration of the spectrometer is schematically described in Figure 2.13. It contains a broadband excitation source, a light dispersing element for the excitation radiation, a sample compartment, a light dispersing component for the radiation emitted, and a sensitive detector for measuring the intensity of the radiation emitted. Usually, emission and excitation spectra are recorded in the same setup. In emission spectroscopy, the emitted light is spectrally resolved by scanning the emission dispersing component. The dispersing component for the excitation source remains fixed during scanning of the emitted light. An emission spectrum yields information on the energetic positions of the optical transitions that are involved in the emission of light [16]. In the excitation spectroscopy, the emission monochromator is set at a wavelength corresponding to an intense emission line and the excitation light is scanned. The spectral ranges of the monochromator are:

- Excitation monochromator: 220 nm to 900 nm
- Emission monochromator: 220 to 900 nm

Figure 2.14. Shimadzu made spectroflurophotometer (Model: RF-5301PC).

Figure 2.14 shows spectrofluorophotometer manufactured by Shimadzu (Model: RF-5301PC). The instrument is equipped with xenon flash lamp and various external cut-off filters to separate excitation and emission spectra. It can measure the luminescence characteristics of solid (pellet or powder), liquid and thin film samples using various sample holders provided by the manufacturer. Another spectrofluorophotometer made by Edinburgh Instruments, UK (model F900) has been

used in the present work to measure the emission and time decay spectra of few samples in the current work. The spectrometer uses a xenon lamp with monochromator to excite the samples for emission study. Microsecond xenon flash lamp used as a source of excitation for the decay measurements of the samples.

3

Emerging Cool White Light Emitting Dy^{3+} doped BaNb$_2$O$_6$ Phosphor for Indoor Lighting Applications

Single phase cool white light emitting BaNb$_2$O$_6$:Dy^{3+} phosphors have been synthesized via conventional solid state reaction method. XRD spectra and Rietveld structural refinement studies confirm that all the samples exhibit pure phase. SEM observations reveal the dense particle packaging with irregular morphology in micron range. The as-prepared phosphors exhibit blue (482 nm) and yellow (574 nm) emissions under 349, 364, 386 and 399 nm excitations corresponding to $^4F_{9/2} \rightarrow {}^6H_J$ (J= 15/2 and 13/2) transitions of Dy^{3+} ions. The energy transfer mechanism between Dy^{3+} ions has been studied in detail and the luminescence decay lifetime for the $^4F_{9/2}$ level was found to be around 146.07 μs for the optimized phosphor composition. The calculated CIE chromaticity coordinates for the optimized phosphor is (x=0.322, y=0.339), which is close to the NTSC (x=0.310, y=0.316) coordinates. The values of CIE chromaticity coordinates and CCT of 5907 K confirm cool white light emission from the phosphor. The study reveals that BaNb$_2$O$_6$:Dy^{3+} phosphor could be a potential candidate for n-UV excited white-LED applications.
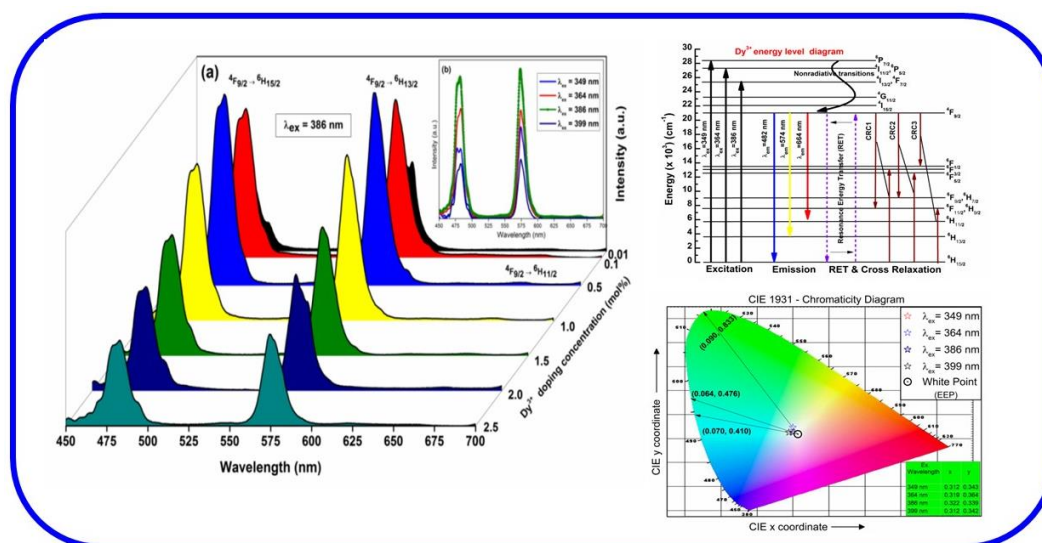
3.1. Introduction

In recent years, rare earth ions doped inorganic luminescent materials have been extensively studied in the fields of materials science, physics, chemistry and life sciences due to various potential applications in display devices (e.g., cathode ray tubes, vacuum fluorescent displays, and field emission display), lighting gadgets (e.g., fluorescent tubes and white light emitting diodes), solid state lasers, biological labelling, X-ray, medical devices, ionization radiation and so on [99,100]. Among them, w-LEDs have been considered to be the next generation illumination sources in the field of solid state lighting instead of traditional incandescent and currently implemented fluorescent lamps due to their numerous advantages such as small size, high energy efficiency, energy-saving, robustness, high brightness, fast switching, longer life time (>100 000 h) and environmental friendliness [101–103]. Generally, two approaches have been implementing to achieve white light through SSL. The first one is phosphor free SSL approach employing RGB-LEDs, which consist of red, green and blue monochromatic LEDs to obtain white light. The main drawback of this approach is that every LED must be adjusted by individual power supply to balance the emission intensity of each color. However, the second approach involves phosphor integrated to the SSL device. The phosphor-converted (pc) LED uses an UV/n-UV light in combination with single/multiple phosphors that convert a part of light emitted by UV/n-UV LED into white light [104,105]. At present, most of the commercially available w-LEDs are based on the second approach because of the simplicity in operation. The combination of blue LED (InGaN) coated with yellow emitting ($Y_3Al_5O_{12}:Ce^{3+}$) phosphor is one of the widely used approaches to produce w-LEDs. However, this approach encounters some serious issues such as halo effect i.e. blue/yellow color separation, color dependence on chromaticity, and poor color-rendering index (<65) due to the lack of green and red-emitting phosphor components at long wavelength region, which limits the LED applications further [106]. Therefore, single phase novel phosphors are essentially required for the fabrication of w-LED using   UV/n-UV LED chips to overcome the problems mentioned above.

Hence, in the present chapter, the $BaNb_2O_6$ phosphor has been synthesized to investigate thoroughly for the first time. The luminescent properties of various rare-

earth ions doped niobate phosphors have been investigated and reported elsewhere [107–110]. However, to the best of our knowledge, luminescent properties of Dy^{3+} ions doped $BaNb_2O_6$ phosphors has never been reported in the literature. In addition, it is well-known that Dy^{3+} ions with $4f^9$ electronic configuration has complex energy levels and various possible transitions between f-f levels that are highly selective and exhibit sharp line spectra [111]. It gives emission in blue and yellow band and the intensity ratio of these two emission bands depends on the host crystal structure [112,113].

In the current chapter, a series of Dy^{3+} ions doped single-phase $BaNb_2O_6$ phosphors have been prepared by solid state reaction method to explore its possibility as potential phosphor for w-LEDs by investigating photoluminescence and colorimetric properties in detail.

3.2. Synthesis of $BaNb_2O_6$: Dy^{3+}

The precursor chemicals $BaCO_3$, Nb_2O_5 and Dy_2O_3 were taken as starting materials. $Ba_{(1-x)}Nb_2O_6$: xDy^{3+} (x = 0.01, 0.1, 0.5, 1.0, 1.5, 2.0 and 2.5 mol %) phosphors were synthesized by conventional solid state reaction method as described section 2.1.1 (Chapter 2) and the synthesis procedure has been mentioned in Figure 2.4.

3.3 Results and Discussion

3.3.1. Thermal studies of $BaNb_2O_6$

The thermal behaviour of $BaNb_2O_6$ was investigated by utilizing TGA and DSC profiles as shown in Figure 3.1. There are two major stages of weight loss observed in TGA curve. At first stage of weight loss about 16.52% takes place between 100 and 600 °C accompanying to the endothermic broad peak at 455 °C in DSC attributed due to removal of moisture and acetone. In the second stage, slight weight loss about 9.34 % observed between 600-785 °C attributed due to release of CO_2 gas. In addition to that one exothermic peak observed at 1050 °C, which could be due to the formation of main $BaNb_2O_6$ phase. Based on the TGA profile, it is noticed that total weight loss in the process of forming $BaNb_2O_6$ up to the calcination temperature 1200 °C is about 25.86 %. DSC profile exhibits crystallization temperature (T_c) at 1050 °C for the

$BaNb_2O_6$ powder sample. Hence, the samples calcined at 1100 and 1200 °C were characterized by using XRD to optimize the calcination temperature and phase purity.
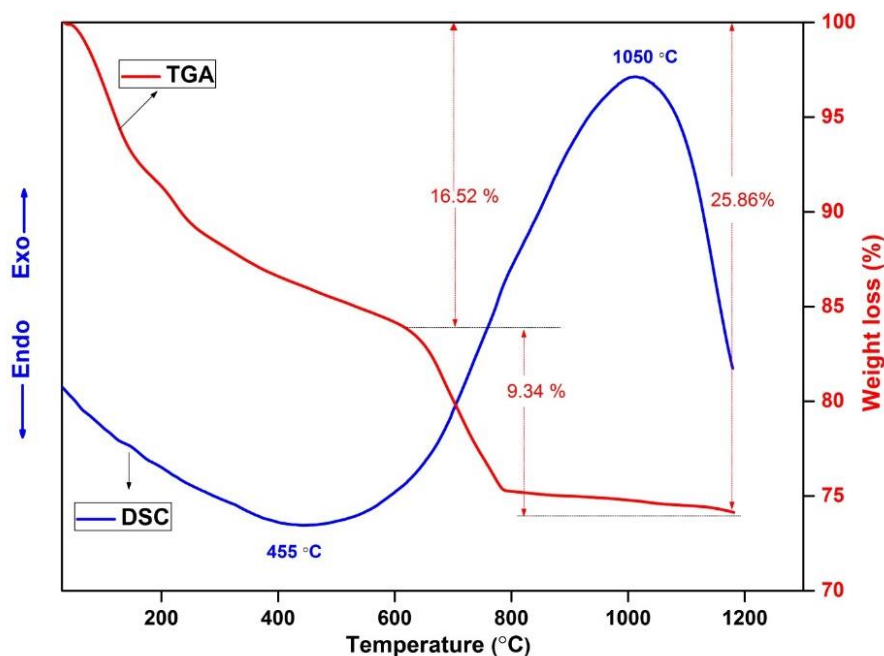
Figure 3.1. TGA-DSC curves for $BaNb_2O_6$ powder synthesized by SSR method.

3.3.2. Structural and morphological analysis

Figure 3.2 represents the X-ray diffraction profiles of $BaNb_2O_6$ powder. The pure phase of $BaNb_2O_6$ was not observed at 1100 °C. Further, the sample sintered at 1200 °C exhibit pure phase of $BaNb_2O_6$ and all the lines are matching with the reported values of orthorhombic $BaNb_2O_6$ (PDF-4+ (ICDD) standard card no. 04-012-8861). No other impurity phase was detected, which indicate the formation of pure orthorhombic $BaNb_2O_6$ phase at the calcination temperature 1200 °C. The crystal structure of $BaNb_2O_6$ compound was reported for the first time by Sirotinkin *et al.* in 1990, and has orthorhombic [space group $C222_1$ (20)] structure with cell parameters a = 7.880 Å b = 12.215 Å, c = 10.292 Å, and Z = 8 [114]. Figure 3.3 illustrates the XRD patterns of undoped and Dy^{3+} ions doped $BaNb_2O_6$ phosphors that are in agreement with the PDF-4+ (ICDD) standard card no. 04-012-8861. It was found that there is no change in peak positions among all XRD patterns, which indicate pure phase formation for undoped and doped $BaNb_2O_6$ phosphors with respect to their

corresponding (hkl) planes. This fact could be due to large ionic radius of Ba^{2+} (1.36 Å) than Dy^{3+} (0.92 Å) and Dy^{3+} ions may occupy Ba^{2+} sites when they enter into $BaNb_2O_6$ host lattice. Hence, no additional peaks were found up to 2 mol% doping of Dy_2O_3, which means that Dy^{3+} ions were successfully substituted for Ba^{2+} ions without changing crystal structure of the host lattice.
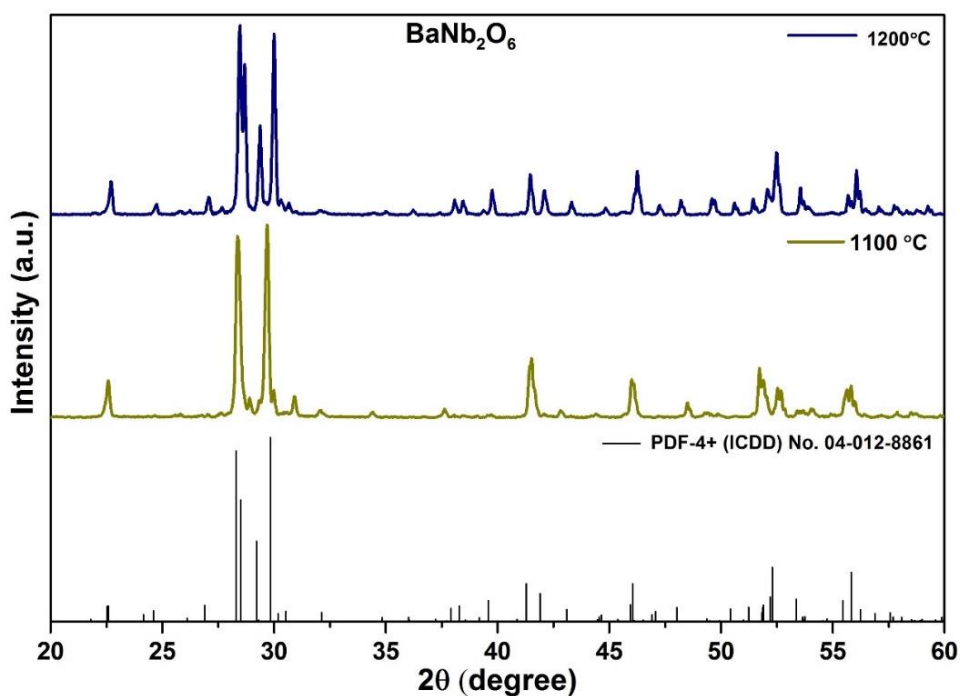
Figure 3.2. X-ray diffraction pattern of $BaNb_2O_6$ powder sintered at 1100 and 1200 °C.

The average crystallite size (D) and strain (ε) of the samples were calculated using most reliable Williamson–Hall (W-H) equation [94,115]

$$\beta \, Cos \, \theta = \left(\frac{K\lambda}{D}\right) + \, 4\varepsilon \, Sin\theta$$

where K is shape factor (0.94), *D* is average crystallite size, λ is wavelength of Cu-K$_\alpha$ radiation, θ is Bragg's diffraction angle of the planes and β is the corrected full width at half maximum (FWHM). The average crystallite size of $Ba_{(1-x)}Nb_2O_6$: xDy^{3+} (x = 0.0, 0.1, 0.5, 1.0 and 2.0 mol%) samples was found to be in the range 44 and 55 nm. The strain present in lattice was calculated and the values for x = 0.0, 0.1, 0.5, 1.0 and 2.0 mol% Dy^{3+} ions doped $BaNb_2O_6$ sintered at 1200 °C were found to be 0.081, 0.114, 0.113, 0.061 and 0.091, respectively. Further the average crystallite size calculated by Debye - Scherer's formula [116] $[D = K\lambda/\beta Cos\theta]$ was found to be in the range of 40

to 89 nm, which are in good agreement with the calculations performed using W-H method [117].
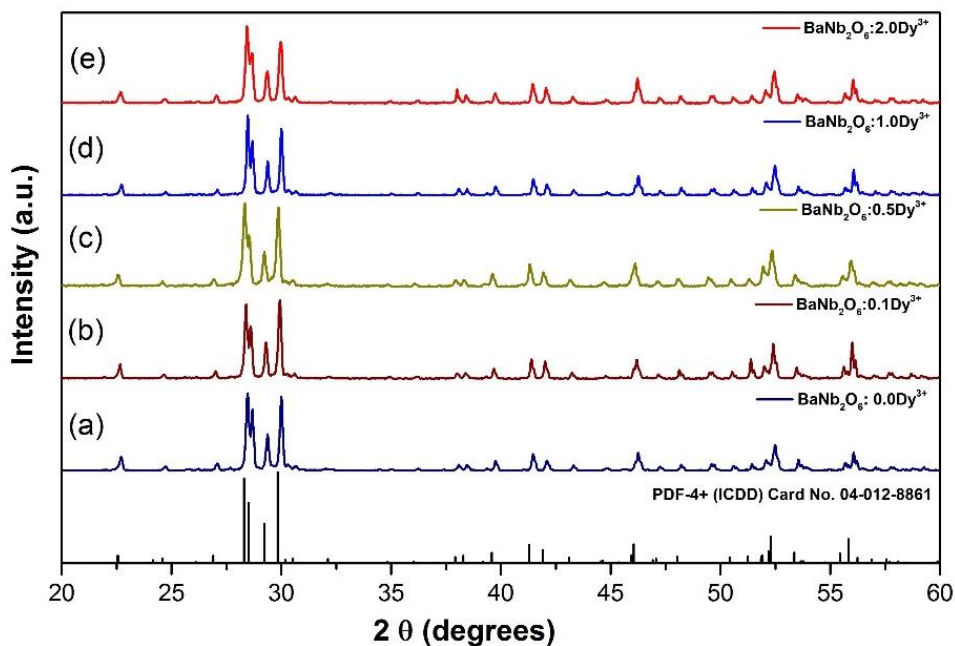
Figure 3.3. Powder XRD patterns of $Ba_{(1-x)}Nb_2O_6:xDy^{3+}$ (x=0.0, 0.1, 0.5, 1.0 and 2.0 mol%) phosphors.
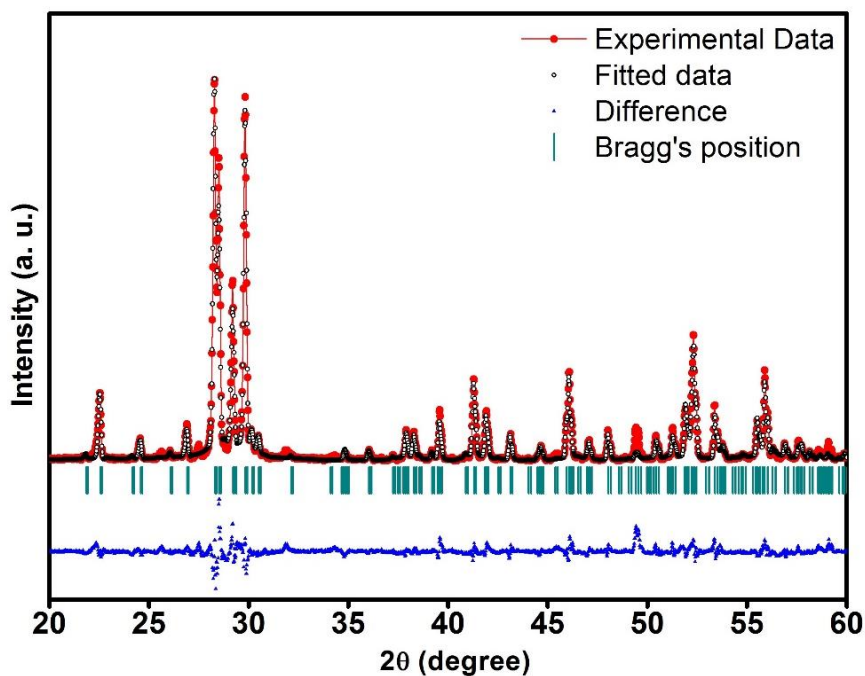
Figure 3.4. Experimental, calculated and difference in X-ray diffraction pattern of $BaNb_2O_6$ powder.

The Rietveld refinement of undoped $BaNb_2O_6$ was carried out using FullProf software as shown in Figure 3.4. The calculated unit cell parameters are summarized in Table 3.1. The results indicate a good agreement between the observed and calculated diffraction patterns of orthorhombic phase [space group $C222_1$ (20)] without any anonymous peak [95], which are close to those reported by Sirotinkin *et al* [114]. Figure 3.5 shows the orthorhombic crystal structure of $BaNb_2O_6$ lattice projected onto b-c plane.

Table 3.1. Calculated crystallographic data of $BaNb_2O_6$ by Rietveld refinement method

Formula	$BaNb_2O_6$
Symmetry	Orthorhombic
Space group	$C222_1$ (20)
a (Å)	7.8707
b (Å)	12.2096
c (Å)	10.2881
Z	8
R_p	25.6
R_{wp}	31.0
χ^2 (Goodness of Fit)	4.2
V(Å^3)	988.680
Density (mg m^{-3})	5.62
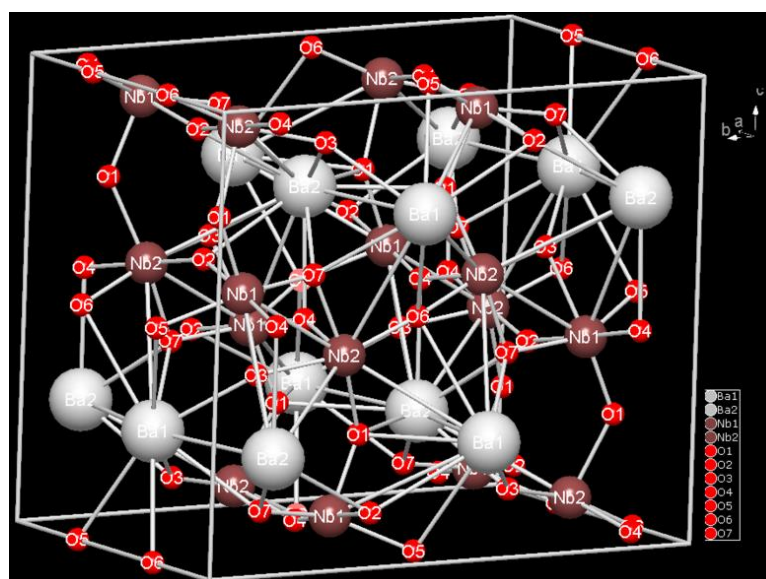
Figure 3.5. Crystal structure of $BaNb_2O_6$ in b-c plane.

Figure 3.6 (a) & (b) represents SEM micrograph of 0.5 mol% Dy^{3+} ions doped $BaNb_2O_6$ phosphor. The micrograph reveals inhomogeneous and uneven dense morphology in micrometer range. The typical crystalline particle size is in the range of 4-6 micrometer in dimension. It is obvious that, micrometer sized crystalline powder would be very much suitable to produce an efficient white light for solid state lighting applications [118].
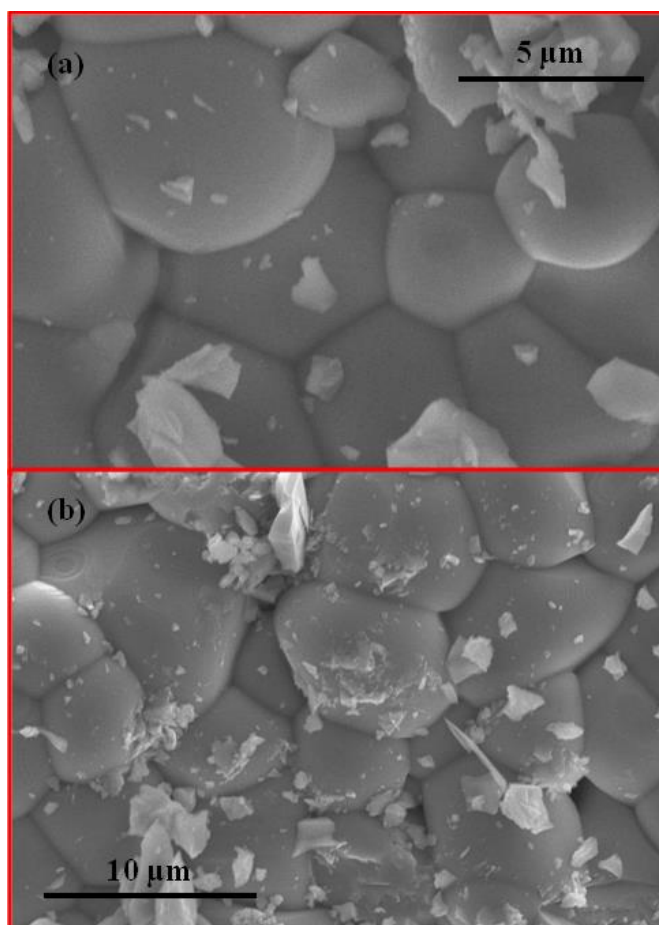
Figure 3.6. (a & b) SEM micrographs of $Ba_{(1-x)}Nb_2O_6$: xDy^{3+} (x=0.5 mol%) phosphor sintered at 1200 ^{o}C.

3.3.3. Photoluminescence studies

Figure 3.7 illustrates the photoluminescence excitation (PLE) spectrum of the $Ba_{(1-x)}Nb_2O_6$:xDy^{3+} (x=0.5 mol%) phosphor by monitoring the emission wavelength at 574 nm. The PLE spectrum consists of seven sharp peaks due to intra 4f-4f transitions

located at 326, 349, 364, 386, 427, 454 and 474 nm, which are attributed from ground state $^6H_{15/2}$ to the different excited states ($^6P_{3/2}$,$^4M_{17/2}$), $^6P_{7/2}$, ($^4I_{11/2}$,$^6P_{5/2}$), ($^4F_{7/2}$,$^4I_{13/2}$), $^4G_{11/2}$, $^4I_{15/2}$ and $^4F_{9/2}$, respectively [119,120].

Figure 3.8 (a) shows the emission spectra of $Ba_{(1-x)}Nb_2O_6$:xDy^{3+} (x= 0.01, 0.1, 0.5, 1.0, 1.5, 2.0 and 2.5 mol%) phosphors with different doping concentration of Dy^{3+} ions at 386 nm excitation wavelength. Emission spectra exhibit two intense peaks at 482 and 574 nm and a very weak peak at 664 nm corresponding to the $^4F_{9/2} \rightarrow ^6H_{15/2}$, $^4F_{9/2} \rightarrow ^6H_{13/2}$, and $^4F_{9/2} \rightarrow ^6H_{11/2}$ transitions, respectively [119].
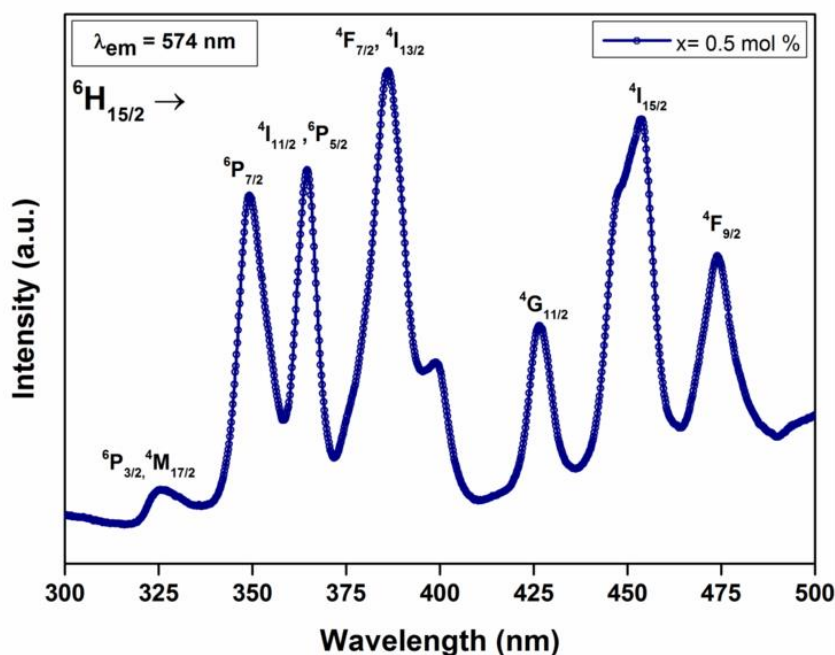
Figure 3.7. Photoluminescence excitation spectra (λ_{em}=574 nm) of $Ba_{(1-x)}Nb_2O_6$:xDy^{3+} (x=0.5 mol%) phosphor.

The $^4F_{9/2} \rightarrow ^6H_{15/2}$ transition belongs to the magnetic dipole allowed and its intensity does not depend on the crystal field of the host [121]. On the other hand, the intensity of the hypersensitive transitions (ΔL=2 and ΔJ=2) correspond to $^4F_{9/2} \rightarrow ^6H_{13/2}$ belongs to a forced electric dipole transition, which is allowed in case that Dy^{3+} ions are located at the local sites with non-inversion center symmetry [122,123]. In Dy^{3+} doped $BaNb_2O_6$ phosphor, the intensity of yellow emission ($^4F_{9/2} \rightarrow ^6H_{13/2}$) is stronger than blue ($^4F_{9/2} \rightarrow ^6H_{15/2}$) that confirms the location of the active ions (Dy^{3+}) in low symmetry environment without the inversion centre in the host. As the radius of Dy^{3+} ion is less

than Ba^{2+}, Dy^{3+} ions can easily enter into Ba^{2+} sites having low symmetry. This is in good agreement with the results obtained from XRD analysis [124]. Moreover, the emission spectra of the sample $Ba_{(1-x)}Nb_2O_6$: xDy^{3+} measured at 349, 364, 386 and 399 nm excitations as shown in inset of Figure 3.8 (b).
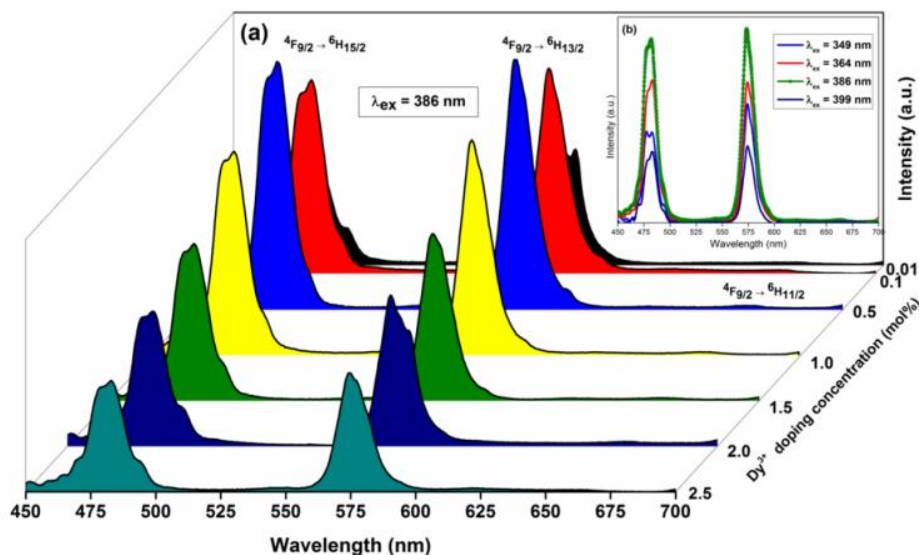
Figure 3.8. (a) Emission spectra (λ_{ex}=386 nm) of $BaNb_2O_6$:Dy^{3+} phosphor at different concentrations of Dy^{3+} ions. **(b)** Emission spectra of $Ba_{(1-x)}Nb_2O_6$: xDy^{3+} (x=0.5 mol%) phosphor at different excitations (inset figure).

The similar profile of emission lines has been observed with different intensities for each excitation. The emission intensity at 386 nm excitation is considered as optimum as its intensity is higher than the emission intensity observed for other excitation wavelengths. This may be due to relatively higher absorption at that wavelength.

The branching ratio (β) is a critical parameter to calculate the relative intensities of emission lines originating from $^4F_{9/2}$ excited state. The branching ratios for yellow and blue transitions originating from $^4F_{9/2}$ were calculated by taking the integrals under respective emission bands. For all Dy^{3+} ion concentrations, the sum of the branching ratios for the corresponding emission bands $^4F_{9/2} \rightarrow ^6H_{15/2}$ and $^4F_{9/2} \rightarrow ^6H_{13/2}$ were found to be unity ($\beta_{482} + \beta_{574}$) suggesting that both the transitions have wide possibility of attaining stimulated emission with higher efficiency [125]. Moreover, it could be

noticed that the emission band $^4F_{9/2} \rightarrow {}^6H_{15/2}$ is broadened and splitted in two peaks in the blue emission region (450-500 nm) which is due to the stark splitting [126,127].

In Figure 3.8 (a), the emission intensity increases initially with an increase in concentration of Dy^{3+} ions and reaches to a maximum at x= 0.5 mol% and then gradually decreases beyond 0.5 mol% due to concentration quenching phenomenon. As the doping concentration of Dy^{3+} ions increases, the distance between luminescent centres decreases that increases the possibility of non-radiative energy transfer [128]. The concentration quenching phenomenon resulted mainly due to the non-radiative energy transfer among Dy^{3+} ions. In the present system, energy transfer mechanism from one Dy^{3+} ion to another depends on critical distance between Dy^{3+}-Dy^{3+} ions. Hence, the critical distance (R_c) calculated between the adjacent Dy^{3+} ions. According to Blasse [128–130], the critical distance could be expressed as:

$$Rc \approx 2\left[\frac{3V}{4\pi X_c N}\right]^{\frac{1}{3}}$$

where, V is the volume of unit cell, X_c is the critical/optimised concentration (mole) of the activator ions and N is the number of cations per unit cell. By analyzing the experimental data, the values are found to be V=988.68 $Å^3$, N =8 and X_c = 0.005. The calculated critical energy transfer distance is 36 Å for the current system. Van Uitert [131] has pointed out energy transfer generally associated with exchange interaction, radiation re-absorption, or multipolar interactions. The exchange interaction is usually accountable for the energy transfer for the forbidden transition and the critical distance of about 5 Å. Since, the distance between adjacent Dy^{3+} ions is larger than 5 Å, as a result the exchange interaction becomes ineffective and multipolar interaction will become important in this case. According to Dexter's theory, when the doping amount of the activator is large enough, the luminescence intensity I and the mole fraction of activator ions x could be related as follows [132,133]:

$$log(I/x) = -\frac{Q}{3}log\,x + A$$

where, A is a constant and Q represents interaction type between rare earth ions. If Q=6, 8 and 10, the interaction may be corresponding to the electric dipole-dipole (d-d), dipole-quadrupole (d-q) and quadrupole-quadrupole (q-q) interactions, respectively

[134]. Depending on the emission spectra of $Ba_{(1-x)}Nb_2O_6$: xDy^{3+} excited at 386 nm, the correlation between *log(I/x)* and *log(x)* is shown in Figure 3.9. The calculated value of Q is 4.95, which is close to 6 discloses that the concentration quenching mechanism in the $BaNb_2O_6$:Dy^{3+} phosphor occurs due to electric dipole-dipole (d-d) interaction [128,135].
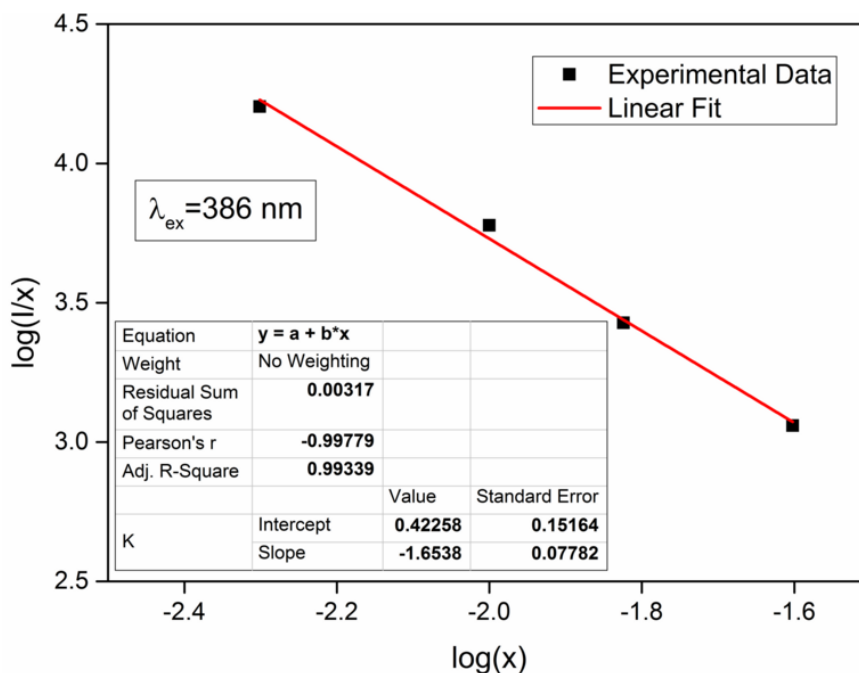
Figure 3.9. Relationship of log(I/x) with log(x) in $BaNb_2O_6$:Dy^{3+} phosphor under 386 nm excitation.

The radiative emission process explained as that the radiation excites the Dy^{3+} ions to the higher excited levels and then quickly relaxed to the $^4F_{9/2}$ level by non-radiative and radiative transfer from $^4F_{9/2}$ excited level as shown in schematic energy level diagram in Figure 3.10. The upward and downward arrows in this figure represent excitation and emission, respectively. The possible non-radiative channels explained in Figure 3.10 are: (i) the possible resonant energy transfer (RET): ($^4F_{9/2}+^6H_{15/2} \rightarrow$ $^6H_{15/2}+^4F_{9/2}$) by considering the energy match rule, and (ii) cross relaxation channels (CRC1, CRC2 and CRC3) among Dy^{3+} ions are responsible for de-population of $^4F_{9/2}$ energy level by non-radiative such as ($^4F_{9/2}+^6H_{15/2}\rightarrow^6F_{11/2},^6H_{9/2}+^6F_{5/2}$), ($^4F_{9/2}+^6H_{15/2}\rightarrow$ $^6F_{9/2},^6H_{7/2}+^6F_{5/2}$) and ($^4F_{9/2}+^6H_{15/2}\rightarrow$ $^6F_{1/2}+^6F_{11/2},^6H_{9/2}$) for as prepared phosphors [124,128,136]. Further, the luminescence intensity ratio of yellow to blue (*Y/B*) is

essential for white light emission. The calculated *(Y/B)* ratio for the optimized excitation wavelength of 386 nm was found to be close to unity for all doping concentrations. There has been slight variation in the value of the ratio near to unity for other three excitations wavelengths namely, 349, 364 and 399 nm, which confirms excellent stability of the color coordinates against different excitations and concentrations. The intensity ratio being almost constant was attributed to the local environment around Dy^{3+} ions and is invariant with the varying concentration of Dy^{3+} ions [123].
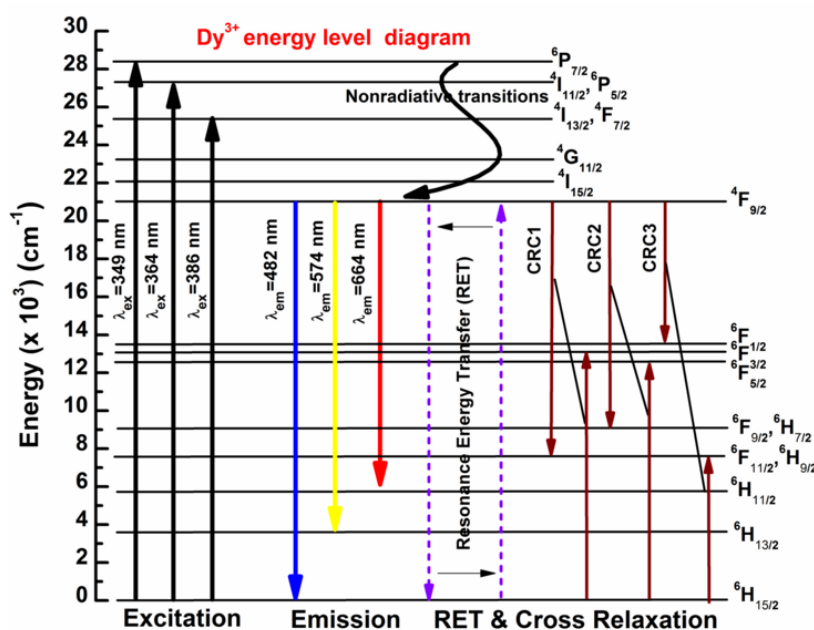
Figure 3.10. Partial energy level diagram illustrating excitation, emission and energy transfer mechanisms of Dy^{3+} ions in $BaNb_2O_6$ phosphors.

3.3.4. CIE chromaticity coordinates

The Figure 3.11 shows the CIE chromaticity coordinates for the optimized sample calculated from the emission spectra measured under different excitations. The CIE chromaticity coordinates for optimized phosphor were found to be (0.312, 0.343), (0.319, 0.364), (0.322, 0.339) and (0.312, 0.342) for corresponding excitations 349, 364, 386, 399 nm, respectively and are indicated in Figure 3.11. An excellent white light chromaticity coordinates (0.322, 0.339) were observed for 386 nm excitation and is very close to the standard equal energy white light point (0.333, 0.333). The CIE chromaticity

coordinates under optimized excitation (λ_{ex}=386 nm) for different Dy^{3+} ion concentrations are given Table.3.2. It is interesting to note that the optimized $Ba_{(1-x)}Nb_2O_6$:xDy^{3+} (x=0.5 mol%) phosphor sample exhibited superior white luminescence coordinates compared to different Dy^{3+} doped phosphor hosts such as $CaMoO_4$:Dy^{3+} (0.28, 0.27) [124] , $Sr_3Gd(PO_4)_3$:Dy^{3+} (0.25, 0.29) [128], YPO_4:Dy^{3+} (0.36, 0.42) [111] and found to be extremely close to commercial pc-LED (Blue LED+YAG:Ce^{3+}) and National Television System Committee (NTSC) white light emission coordinates (0.32, 0.32) and (0.310, 0.316), respectively.

Table 3.2. Y/B ratio, CIE chromaticity coordinates and CCT for $BaNb_2O_6$:Dy^{3+} phosphors at various doping concentrations.

λ_{ex}=386 nm			
x (Dy^{3+} concentration)	Y/B ratio	(*x, y*)	CCT (K)
0.01	1.11	(0.329, 0.339)	5689
0.10	1.06	(0.322, 0.338)	6000
0.50	1.01	(0.322, 0.339)	5907
1.00	1.05	(0.314, 0.341)	6373
1.50	1.06	(0.320, 0.340)	6056
2.00	1.11	(0.331, 0.332)	5623
2.50	1.07	(0.312, 0.319)	6652

The calculated CCT values for Dy^{3+} ions doped $BaNb_2O_6$ phosphors were found to vary between 5689-6373 K and falls in cool-white region. The calculated CCT was 5907 K for optimized concentration (x=0.5 mol%) of $BaNb_2O_6$:Dy^{3+} phosphor, which represents cool white emission and is very close to "ideal white" region of the chromaticity diagram. The higher value of CCT indicates better visual acuity and greater brightness perception as compared to lower values [137]. The CCT values lie in the cool white light region signifying the possibility of the phosphor for application in w-LED for outdoor illumination.
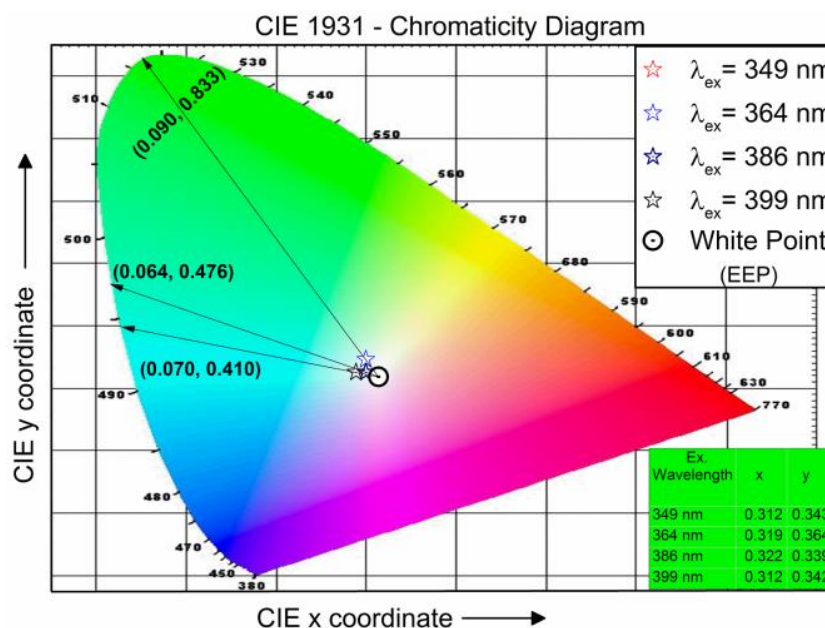
Figure 3.11. CIE chromaticity diagram for Dy^{3+} ions doped $BaNb_2O_6$ phosphor.

Using the chromaticity coordinates given in Figure 3.11 for optimized concentration of as-prepared phosphor, the color purity was calculated and found to be around 7.89×10^{-2}, 5.39×10^{-2}, 5.39×10^{-2} and 7.89×10^{-2} corresponding to 349, 364, 386 and 399 nm excitations wavelengths, respectively. The low value of the color purity indicates the purity of white light emission [39,136]. The above mentioned results indicate that the as-prepared phosphor can be considered as a potential candidate for fabrication w-LED based on n-UV chip as excitation source.

3.3.5. Luminescence decay curve analysis

The room temperature luminescence decay curve has been plotted for $Ba_{(1-x)}Nb_2O_6{:}xDy^{3+}$ (x=0.5 mol %) phosphor and is shown in Figure 3.12. It represents the decay curve of $^4F_{9/2} \rightarrow {}^6H_{13/2}$ emission for phosphor when excited under 386 nm wavelength. To understand the behaviour of luminescent decay, the decay curve was fitted with different equations and the best fit was observed for bi-exponential equation [138,139]:

$$I = A_1 \, e^{-t/\tau_1} + A_2 \, e^{-t/\tau_2}$$

where, I is the luminescence intensity; t is time; τ_1 and τ_2 are the decay time for the exponential component and A_1 and A_2 are the fitting parameter constants, respectively. Thus, the average lifetime in case of bi-exponential fitting can be determined by using equation:

$$\tau_{avg} = \frac{A_1\tau_1^2 + A_2\tau_2^2}{A_1\tau_1 + A_2\tau_2}$$

The fluorescent lifetime τ_{avg} for $^4F_{9/2}$ level for optimized phosphor sample was found to be ~146.07 µs. Generally, the PL decay curves can be influenced by energy transfer between Dy^{3+} ions. If there is no interaction between the rare earth ions, the decay curves are usually fitted to a single exponential function. The bi-exponential fitting behaviour shows the possibility of interaction between Dy^{3+} ions in $BaNb_2O_6$ lattice as discussed in the section 3.3.3.

Adj. R-Square	0.99537	
Residuals	Value	Error
A1	0.23881	0.01432
t1	10.35792	1.27731
A2	0.74621	0.00818
t2	149.0952	2.98319
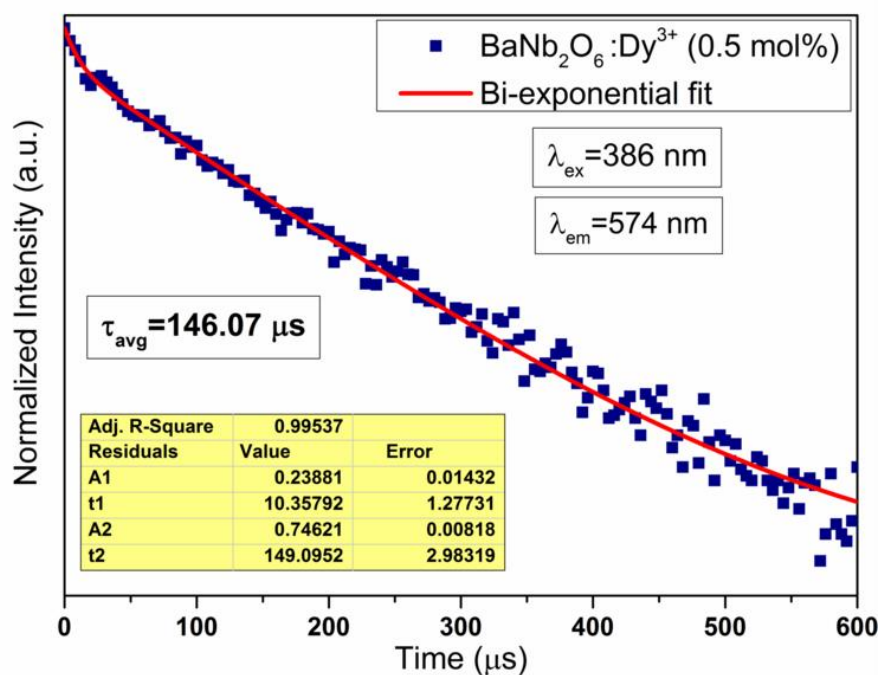
Figure 3.12. Luminescence decay curve (λ_{em}=574 nm) of $Ba_{(1-x)}Nb_2O_6{:}xDy^{3+}$ (x=0.5 mol%) phosphor under 386 nm excitation.

4

Pure Orange Color Emitting Sm^{3+} doped BaNb$_2$O$_6$ Phosphor for Solid State Lighting Applications

Single phase pure orange light emitting BaNb$_2$O$_6$: xSm^{3+} (0.5 ≤ x ≤ 3.0 mol %) phosphors with orthorhombic structure have been synthesized via high temperature solid state reaction method. Crystal structure, morphology, luminescent and decay properties were studied extensively for the synthesized phosphor. The luminescence spectrum of Sm^{3+} doped BaNb$_2$O$_6$ phosphor exhibit three intense peaks centered at 565, 599 and 645 nm corresponding to the $^4G_{5/2}{\rightarrow}^6H_{5/2}$, $^4G_{5/2}{\rightarrow}^6H_{7/2}$ and $^4G_{5/2}{\rightarrow}^6H_{9/2}$ transitions, respectively. The optimum concentration for Sm^{3+} doped BaNb$_2$O$_6$ is was 1.5 mol% and the probable energy transfer mechanisms between Sm^{3+} ions caused for concentration quenching have been explained in detail. The calculated CIE chromaticity coordinates have been found to be (0.557, 0.440) which lies in pure orange region and is in close proximity to the Nichia corporation developed amber LED. The luminescence decay lifetime for $^4G_{5/2}$ excited level was found to be in the microseconds (µs) range. The Sm^{3+} doped BaNb$_2$O$_6$ phosphor could be a potential candidate for use in the display and solid state lighting applications.
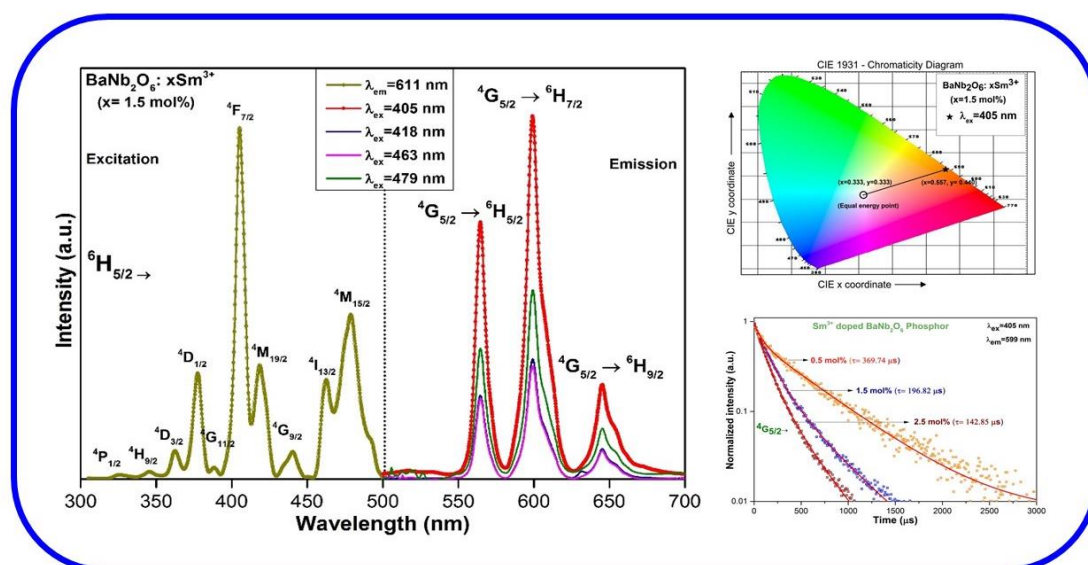
4.1. Introduction

In recent years, w-LEDs have attracted immense attention in the field of solid state lighting (SSL) over their counterpart such as incandescent and fluorescent lighting due to many advantages including superior efficiencies, longer operating lifetimes, reliability and environmental friendliness. There are several ways to fabricate the w-LEDs. The most popular and well-established method is the combination of the blue GaN LED chip with yellow emitting phosphor $Y_3Al_5O_{12}:Ce^{3+}$ (YAG: Ce^{3+}). However, w-LED fabricated by this approach suffer from poor color rendering index (R_a), which is due to the absence of red component, halo effect and low thermal quenching temperature [140,141]. To overcome these shortcomings in fabricating w-LEDs, a combination of n-UV LED chip with RGB phosphors have been studied to enhance white light emission with better R_a value [142]. The shortcoming of this approach is that the efficiency of the red phosphor $Y_2O_2S:Eu^{3+}$ is only about 1/8 of blue phosphor ($BaMgAl_{10}O_{17}: Eu^{2+}$) or green phosphor (ZnS: Cu^+, Al^{3+}). To solve this difficulty, researchers have synthesized red phosphors based on Eu^{2+} doped $CaAlSiN_3$ or $M_2Si_5N_8$ (M=Ca, Sr, Ba), which offers high quantum efficiency and stability. However, the high processing temperature and high nitrogen pressure limit their practical applications [143–145]. Another approach to generate white light is combination of the n-UV excitation source with cyan plus orange light emitting single phase phosphor. Thus, the development of orange emitting phosphors by using n-UV excitation source is essential and needs to be investigated in the fields of solid state lighting and display technologies [146–148]. Among all lanthanides, samarium (Sm^{3+}) ion with $4f^5$ electronic configuration exhibit a strong orange emission in the visible region.

In previous chapter, Dy^{3+} ion doped $BaNb_2O_6$ phosphor has been discussed to reveal the utility, importance of phosphor [149]. However, further investigations on producing orange emission from Sm^{3+} doped $BaNb_2O_6$ is still of great interest in the process of achieving white light by using new combination of cyan plus orange, which has been rarely performed. To the best of our knowledge, the luminescence properties of Sm^{3+} doped $BaNb_2O_6$ phosphor have not been reported so far.

In the present chapter, Sm^{3+} doped $BaNb_2O_6$ phosphor has been synthesized by solid state reaction method to investigate the structural, morphological, luminescent and chromaticity properties of the as prepared phosphor. These properties have been investigated in detail to examine the potentiality of the barium niobate phosphor for the

applications in display devices, LEDs and solid state lighting. The energy transfer processes in Sm^{3+} doped $BaNb_2O_6$ have also been discussed in detail.

4.2. Synthesis of $BaNb_2O_6$: Sm^{3+}

The precursor chemicals $BaCO_3$, Nb_2O_5 and Sm_2O_3 were taken as starting materials. $BaNb_2O_6$: xSm^{3+} (x = 0.5, 1.0, 1.5, 2.0, 2.5 and 3.0 mol %) phosphors were synthesized by conventional solid state reaction method as described in section 2.1.1 (Chapter 2) and the synthesis procedure has been mentioned in Figure 2.4.

4.3. Results and Discussion

4.3.1. Structural properties

Figure 4.1 (a) represents the X-ray powder diffraction pattern of $BaNb_2O_6$: xSm^{3+} (x= 0.0, 0.5, 1.0, 1.5 and 2.0 mol%) phosphors along with the standard $BaNb_2O_6$ pattern PDF4+ (ICDD) No. 04-012-8861. The diffraction patterns for $BaNb_2O_6$: xSm^{3+} phosphor indicate the orthorhombic structure (space group: $C222_1$) as all the observed peaks are well-matched with the standard diffraction patterns (PDF4+ ICDD NO: 04-012-8861) of the $BaNb_2O_6$ published by Sirotinkin *et al*. and no second phase is observed [114]. The calculated lattice parameters are (a=7.8582 Å b=12.1992 Å, and c=10.2775 Å), (a=7.8470 Å b=12.1702 Å, and c=10.2574 Å), (a= 7.8456 Å b=12.1680 Å, and c=10.2533 Å), (a= 7.8413 Å b=12.1609 Å and c=10.2493 Å), (a= 7.8372 Å b=12.1533 Å, and c=10.2413 Å), corresponding to 0.0, 0.5, 1.0, 1.5, 2.0 mol % of Sm^{3+} doped phosphor, respectively and unit cell volume (V) decreases from 985.23 to 975.76 $Å^3$ with increasing concentration. The ionic radii of Sm^{3+} and Ba^{2+} are 0.96 Å and 1.36 Å, respectively. The diffraction peaks are slightly shifting towards larger 2θ angles with increasing Sm^{3+} concentration compared to those of standard $BaNb_2O_6$ pattern as depicted in Figure 4.1(b). This is due to the decrease in interatomic spacing which results from the substitution of higher content of Sm^{3+} ions in Ba^{2+} ions [150]. It indicates that the doped Sm^{3+} ions are successfully incorporated in the host cation at Ba^{2+} sites. The shifting of peak causes due to an expansion of unit cell and result the tensile stress in the host crystal lattice. The peak shift in the XRD pattern may also arise due to the presence of strain in the crystal lattice [151]. The crystallite size and strain were estimated from the most reliable Williamson-Hall (W-H) [94,115] plot

using equation $[\beta\, Cos\, \theta = \left(\frac{K\lambda}{D}\right) + 4\varepsilon\, Sin\theta]$ where β is full width half maximum, λ is wavelength of X-ray (1.5406), θ is diffraction angle, K is shape factor, D is crystallite size and ε is strain. The crystallite size and strain were determined from the plot between βcosθ/ λ versus sinθ/ λ as shown in Figure 4.2. The reciprocal of intercept on the β cos θ/λ axis gave the average crystallite size. The strain (%) obtained from the slope = (4 × strain) of this graph. The calculated crystallite size and strain (%) were found to be 62.9, 59.0, 58.9, 52.5, 51.4 nm and 0.028, 0.062, 0.065, 0.066, 0.081 for $BaNb_2O_6$: xSm^{3+} (x= 0.0, 0.5, 1.0, 1.5 and 2.0 mol%) phosphors, respectively.
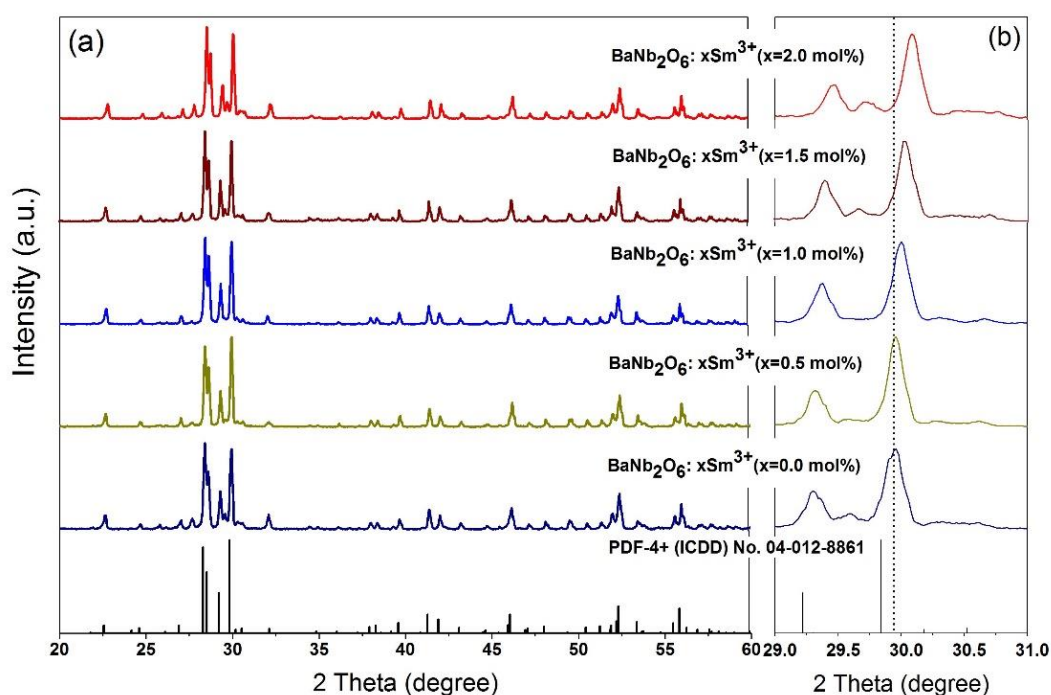
Figure 4.1. X-ray diffraction patterns of $BaNb_2O_6$: xSm^{3+} (x=0.0, 0.5, 1.0 1.5 and 2.0 mol%) powder.
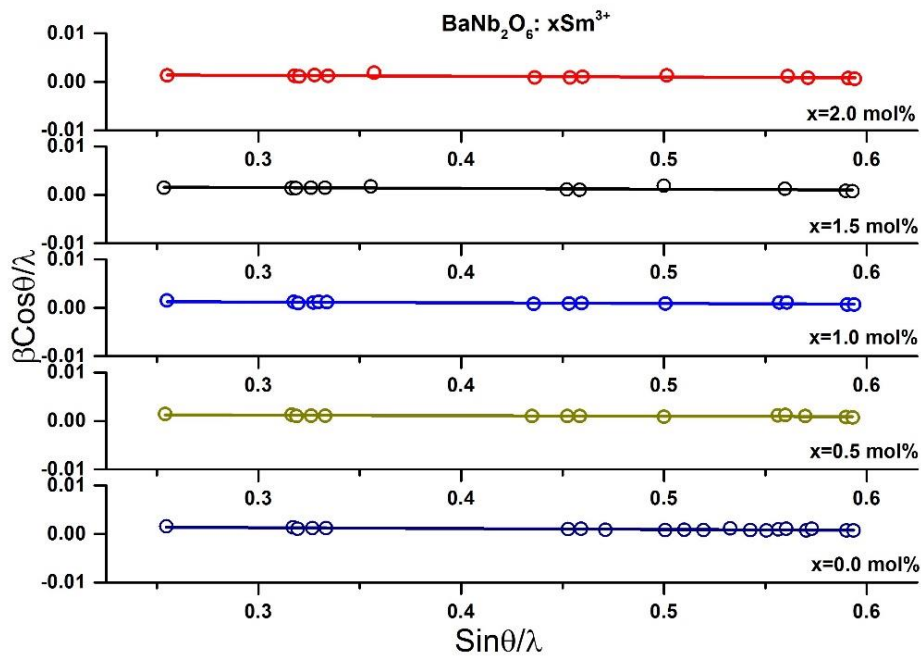
Figure 4.2. W-H plot of $BaNb_2O_6$: xSm^{3+} (x=0.0, 0.5, 1.0 1.5 and 2.0 mol%).

4.3.2. Morphological observation

Figure 4.3 (a & b) shows the SEM micrographs at different magnifications for the $BaNb_2O_6$: xSm^{3+} (x= 1.5 mol%) phosphors prepared through solid state reaction method. The agglomerated, uneven and dense solid particles were observed in the range of 3-5 μm size [146]. It is obvious that, micrometer crystalline powder would be very much suitable to produce an efficient luminescence for solid state lighting applications
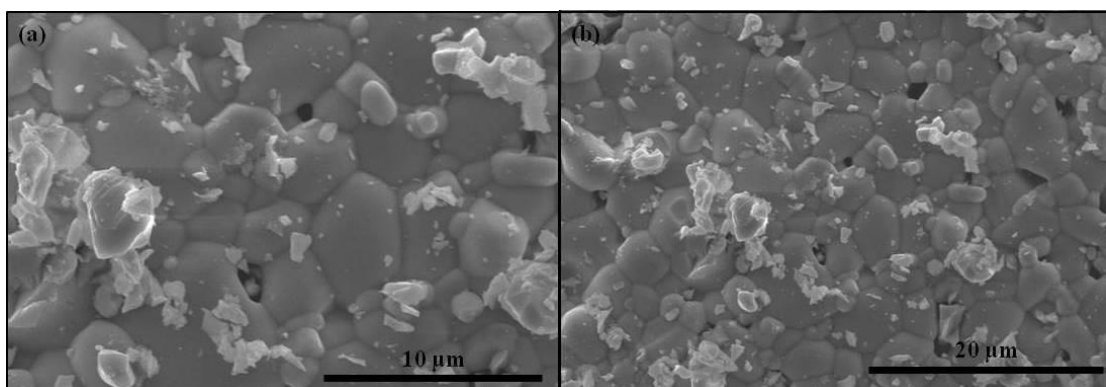
Figure 4.3. Scanning electron micrographs of $BaNb_2O_6$: xSm^{3+} (x = 1.5 mol %) sintered at 1200 °C.

4.3.3. Luminescent studies

Figure 4.4 depicts the photoluminescence excitation and emission spectra of $BaNb_2O_6$: xSm^{3+} (x= 1.5 mol%) phosphors sintered at 1200 °C. The PLE spectrum exhibits ten excitation bands corresponding to the intra-configurational 4f-4f transitions of Sm^{3+} ions originating from the ground state $^6H_{5/2}$ to excited state levels $^4P_{1/2}$, $^4H_{9/2}$, $^4D_{3/2}$, $^4D_{1/2}$, $^4G_{11/2}$, $^4F_{7/2}$, $^4M_{19/2}$, $^4G_{9/2}$, $^4I_{13/2}$ and $^4M_{15/2}$ at 325, 345, 363, 378, 388, 405, 418, 440, 463 and 479 nm, respectively [30,152]. In order to know the optimized excitation wavelength, the four intense excitation wavelengths, (405, 418, 463 and 479 nm) have been chosen to measure photoluminescence spectrum.
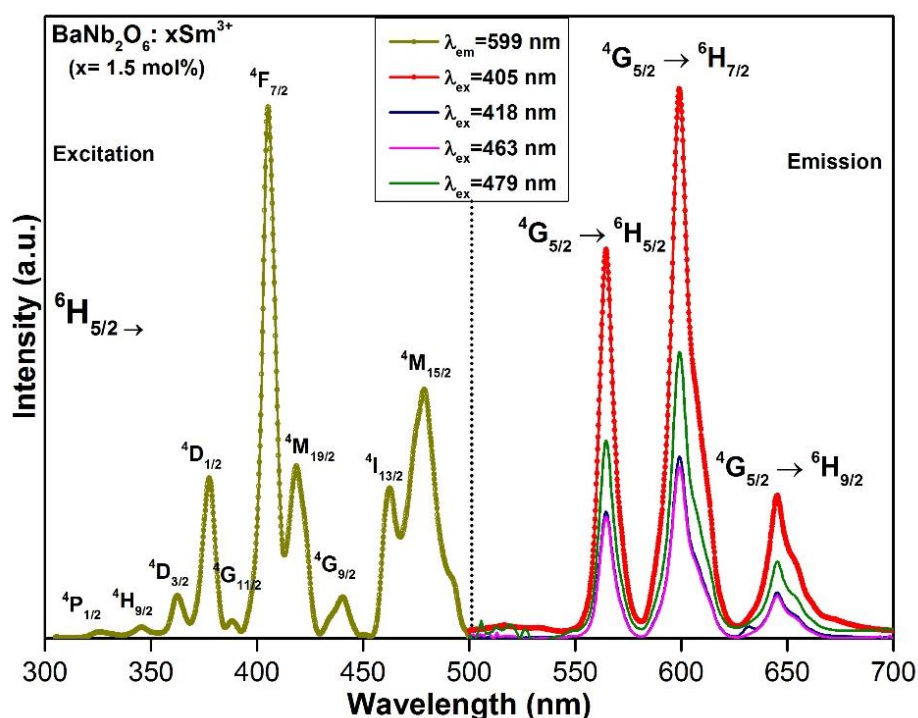
Figure 4.4. Photoluminescence excitation spectrum at λ_{em}=599 nm and emission spectra of Sm^{3+} doped $BaNb_2O_6$ phosphor at different excitation wavelengths.

The three emission bands were observed in orange-red (500-700 nm) spectral region for all excitation wavelengths, which are attributed to de-excitation of $^4G_{5/2}$ level of Sm^{3+} ions to its lower multiplets of ^6H_J (J= 5/2, 7/2 and 9/2). Among these excitation bands, the emission intensity measured at 405 nm excitation was more intense than other wavelengths and considered as optimum excitation wavelength.

The emission spectra of $BaNb_2O_6$: xSm^{3+} (x= 0.5, 1.0, 1.5, 2.0, 2.5 and 3.0 mol%) phosphors measured at λ_{ex}=405 nm ($^6H_{5/2} \rightarrow {}^4F_{7/2}$) excitation wavelength is shown in Figure 4.5. Three emission peaks were observed at 565, 599 and 645 nm corresponding to $^4G_{5/2} \rightarrow {}^6H_{5/2}$, $^4G_{5/2} \rightarrow {}^6H_{7/2}$, and $^4G_{5/2} \rightarrow {}^6H_{9/2}$, respectively.
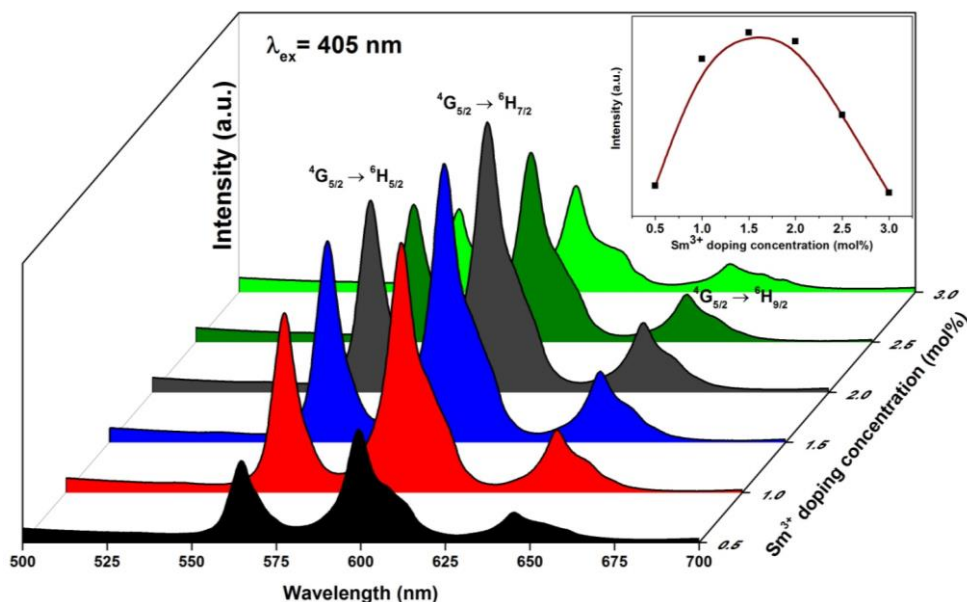
Figure 4.5. Photoluminescence spectra of $BaNb_2O_6$: xSm^{3+} (x= 0.5, 1.0, 1.5, 2.0, 2.5 and 3.0 mol%) at λ_{ex}=405 nm. (Inset shows the dependence of emission intensity on the Sm^{3+} doping concentration.)

The emission peak centered at 565 nm ($^4G_{5/2} \rightarrow {}^6H_{5/2}$) is originated due to purely magnetic dipole moment, second peak at 645 nm ($^4G_{5/2} \rightarrow {}^6H_{9/2}$) is due to purely electric dipole moment and the other at 599 nm ($^4G_{5/2} \rightarrow {}^6H_{7/2}$) is due to both magnetic and electric dipole moments [148,150,152]. Generally, the intensity ratio of electric dipole to magnetic dipole transitions is useful in understanding the symmetry of local environment around the trivalent $4f^5$ ions. In the present phosphor, the magnetic dipole transition is more intense than electric dipole transition suggested that there is no deviation from inversion center and more symmetric in nature [153]. It is observed from Figure 4.5 that there is no change in the position of emission band for all doping concentrations. However, the emission intensity changes with doping concentration of Sm^{3+} ions. Initially, the emission intensity increases, then reaches to a maximum at x=1.5 mol% (critical concentration), beyond that the emission intensity begins to decrease with increase in concentration due to concentration quenching effect [154]. Thus the optimum concentration of Sm^{3+} ions in $BaNb_2O_6$ host is 1.5 mol% and also

the graph between Sm^{3+} ions doped concentration and emission intensity of $^4G_{5/2} \rightarrow ^6H_{7/2}$ peak represented the same inset of Figure 4.5. The concentration quenching may be induced by cross relaxation processes due to proximity in Sm^{3+} ions. When the Sm^{3+} ions doping increases, there is more possibility of enhancing the energy transfer within Sm^{3+} ions beyond the optimal doping concentration through non radiative process.

The critical energy transfer distance *(R_c)* in $BaNb_2O_6:Sm^{3+}$ can be calculated by substituting the values of critical concentration *(X_c)* and structural parameters such as unit cell volume *(V)* and the number of Z ions in the unit cell *(N)*, in the equation as suggested by Blasse [129,130]:

$$R_c \approx 2 \left[\frac{3V}{4\pi X_c N} \right]^{\frac{1}{3}}$$

For the $BaNb_2O_6:Sm^{3+}$ system, $N = 8$, $V = 977.35$ $Å^3$, and $X_c = 0.015$. The calculated critical distance between Sm^{3+} ions is 24.60 Å. Usually, the non-radiative energy transfer occurs due to exchange interaction, radiation re-absorption or multipolar interaction between rare earth ions. Exchange interaction may occur when the critical distance between the activator ions is less than 5 Å, which is much less than the calculated distance for Sm^{3+} doped $BaNb_2O_6$ phosphor. Hence, the multipolar interaction may be responsible for energy transfer mechanism in the present system. In order to obtain the *Q* value according to the Dexter [132,133,155] theory as discussed in section 3.3.3., the plot of *log(I/x)* as a function of *log(x)* is fitted linearly as shown in Figure 4.6. The slope is equal to *–Q/3* from the graph. The calculated Q value is 5.20, which is approximately equal to 6 indicates that the electric dipole-dipole (d-d) interaction is responsible for the luminescence quenching of $^4G_{5/2}$ level in Sm^{3+} doped $BaNb_2O_6$ host. The partial energy level diagram of Sm^{3+} ions in $BaNb_2O_6$ is shown in Figure 4.7. When the population is excited to $^4F_{7/2}$ level for Sm^{3+} ions by 405 nm wavelength, the initial population relaxes non radiatively to the $^4G_{5/2}$ level. There are several energy levels between $^4F_{7/2}$ and $^4G_{5/2}$ levels with little energy differences, which leads non-radiative relaxation to the population of the $^4G_{5/2}$ state [156]. This energy level is separated from the next lower lying $^6F_{11/2}$ level by ~7407 cm^{-1}. Thus, it could be confirmed that radiative transitions and relaxation by non-radiative energy transfer are the two main processes, which could finally depopulate the $^4G_{5/2}$ state.
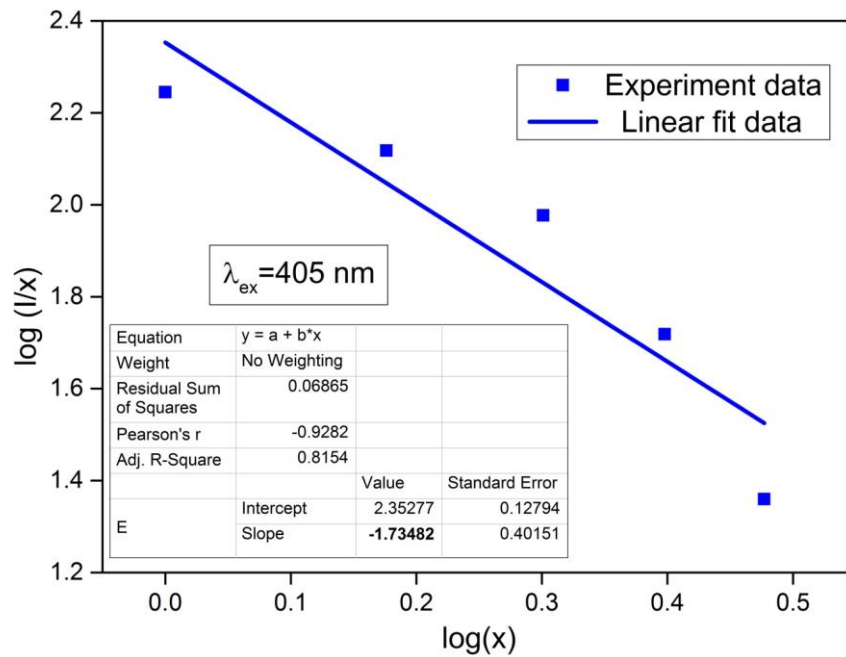
Figure 4.6. The relationship between log*(I/x)* versus log*x* in Sm^{3+} doped $BaNb_2O_6$ phosphors.

The luminescence spectra exhibit three intense emission bands at 565, 599 and 645 nm. The possible cross relaxation channels (CRC) responsible for non-radiative emission beyond the optimum doping concentration as shown in Figure 4.7. The possible cross relaxation channels in the present $BaNb_2O_6$:Sm^{3+} phosphors are as follows: CRC1: $(^4G_{5/2}+^6H_{5/2}) \rightarrow (^6F_{5/2}+^6F_{11/2})$, CRC2: $(^4G_{5/2}+^6H_{5/2}) \rightarrow (^6F_{7/2}+^6F_{9/2})$, CRC3: $(^4G_{5/2}+^6H_{5/2}) \rightarrow (^6F_{9/2}+^6F_{7/2})$ and CRC4: $(^4G_{5/2}+^6H_{5/2}) \rightarrow (^6F_{11/2}+^6F_{5/2})$. Energy transfer though cross relaxation channels may take place between Sm^{3+} ions from $^4G_{5/2}$ populated state to nearby Sm^{3+} ions in the ground state [157]. The energy difference between the $^4G_{5/2}$ state to intermediate levels of Sm^{3+} ions $^6F_{5/2}$, $^6F_{7/2}$, $^6F_{9/2}$, and $^6F_{11/2}$ are 10824, 9947, 8798 and 7407 cm^{-1} respectively, which are closely matching with the energy difference between $^6H_{5/2}$ ground state to various excited levels $^6F_{11/2}$ (10471 cm^{-1}), $^6F_{9/2}$ (9090 cm^{-1}), $^6F_{7/2}$ (7931 cm^{-1}) and $^6F_{5/2}$ (7054 cm^{-1}). The chromaticity diagrams and CIE coordinates are very important to disclose the exact emission color and color purity of the sample [152]. The calculated CIE chromaticity coordinate were found to be (0.557, 0.440) for the optimized $BaNb_2O_6$: xSm^{3+}(x=1.5 mol%) phosphor based on emission spectrum under 405 nm excitation, which is located exactly on the NTSC color gamut as shown in Figure 4.8. The obtained CIE chromaticity coordinates are very much close to the Nichia corporation developed amber LED NSPAR 70BS

(0.575, 0.425). It is observed from Fig. 4.8 that the (x, y) chromaticity coordinates located in pure orange region and the calculated color purity was found to be 99.5%, which confirms the pure emission of orange light from $BaNb_2O_6$: xSm^{3+} (x= 1.5 mol%) phosphors. The calculated CCT value was found to be 1970 K, which is unusual in other Sm^{3+} doped hosts and this emission could be useful for solid state lighting and displays applications.
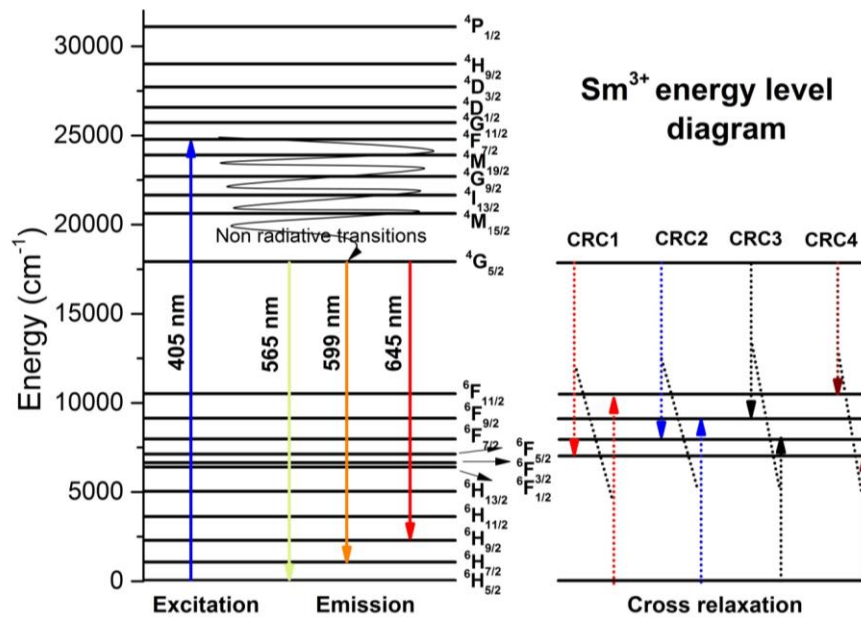
Figure 4.7. Partial energy level diagram and cross relaxation channels of Sm^{3+} ions.
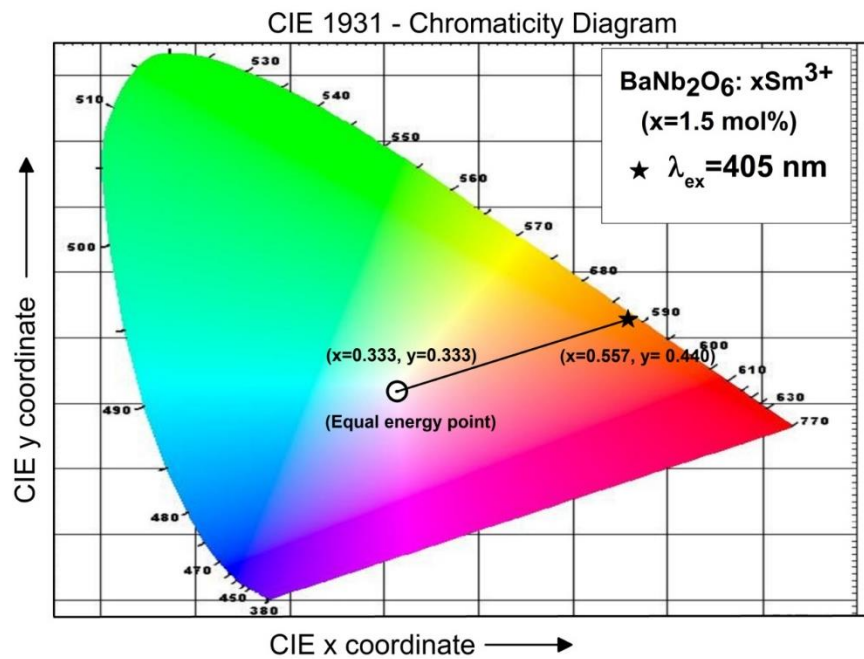
Figure 4.8. Chromaticity coordinates for optimized Sm^{3+} doped $BaNb_2O_6$ phosphor on CIE 1931 chromaticity diagram.

4.3.4. Luminescence decay analysis

The lifetime values for the $^4G_{5/2}$ excited level of Sm^{3+} ions in the prepared $BaNb_2O_6:xSm^{3+}$ (x= 0.5, 1.5 and 2.5 mol%) phosphor have been determined by using decay curve profile measured for $^4G_{5/2} \rightarrow {}^6H_{7/2}$ transition (599 nm) under 405 nm excitation wavelength are depicted in Figure 4.9. The decay curves of the as prepared phosphor are well fitted with a double exponential function as discussed in section 3.3.5 and the calculated average lifetimes for the $^4G_{5/2}$ excited level were found to be 369.74, 196.82 and 142.85 μs corresponding to 0.5, 1.5 and 2.5 mol % of Sm^{3+} concentrations, respectively. These results indicate that the average lifetime decreased with increasing concentration of Sm^{3+} ions, which confirm the possibility of energy transfer between Sm^{3+} ions.
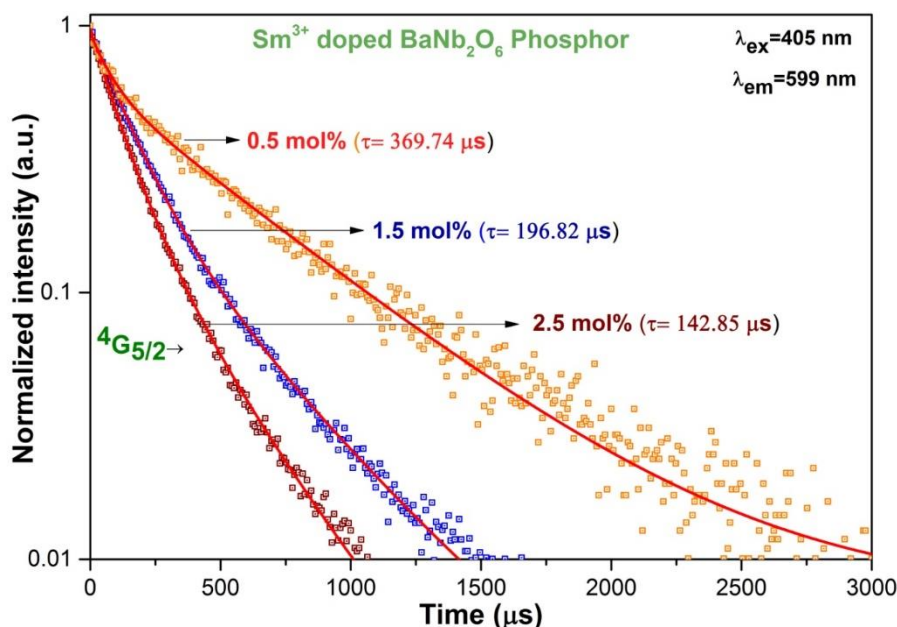
Figure 4.9. Decay curves of $BaNb_2O_6$: xSm^{3+} (x= 0.5, 1.5 and 2.5 mol%) concentrations (λ_{ex}=405 nm and λ_{em}=599 nm).

5

Red Light Emitting Eu^{3+} doped $BaNb_2O_6$ Phosphor for Solid State Lighting Applications

Eu^{3+} doped $BaNb_2O_6$ phosphors were successfully synthesized by conventional solid state reaction method. TGA-DSC, XRD and SEM characterization techniques were used to disclose thermal, structural and morphological properties of the synthesized phosphors. X-ray diffraction pattern for the synthesized phosphor calcined at 1200 ^oC confirms the formation of pure orthorhombic phase for $BaNb_2O_6$. In addition to the above mentioned characterizations, photoluminescence properties were also investigated for the $BaNb_2O_6$ phosphor under n-UV /blue excitations. Intense red emission was observed at 614 nm correspond to $^5D_0 \rightarrow {}^7F_2$ transitions of Eu^{3+} under the both 395 nm ($^7F_0 \rightarrow {}^5L_6$) and 466 nm ($^7F_0 \rightarrow {}^5D_2$) excitations. The CIE chromaticity coordinates evaluated from the emission spectra are falling in the pure red region of the CIE 1931 diagram, which are very much close to the commercial red phosphor ($Y_2O_2S :Eu^{3+}$). The above results indicate that Eu^{3+} doped $BaNb_2O_6$ phosphors may be potential candidates to use in w-LEDs in which tricolor (red/green/blue) phosphors are excited by n-UV light.
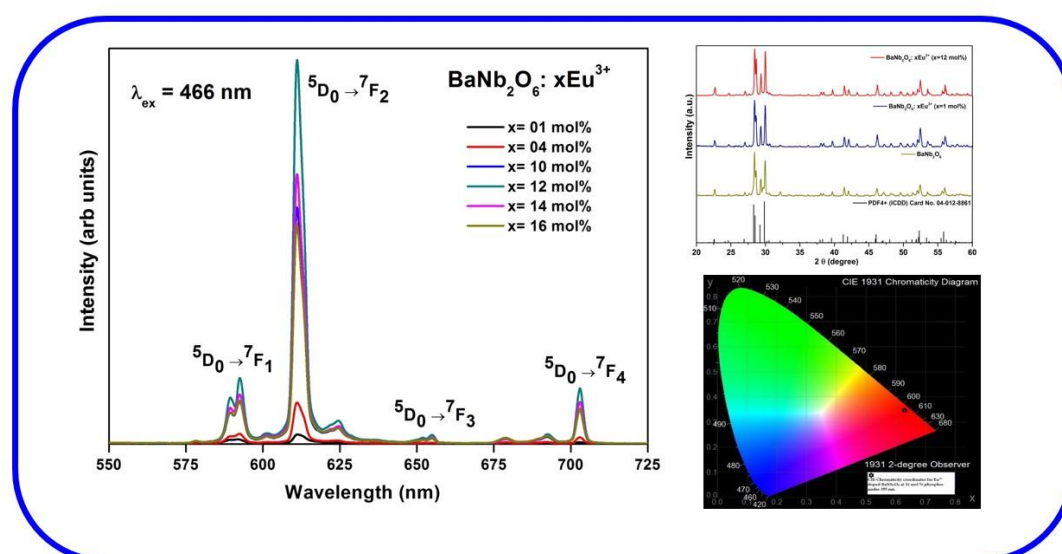
5.1. Introduction

Inorganic compounds doped with rare earth ions form an important class of phosphor materials, which have been utilized for developing efficient w-LEDs, emission display devices such as field emission displays (FED), plasma display panels (PDP) and in lightening industries [9,158,159]. Due to low energy consumption, longer lifetime and environmental friendliness, solid state lighting has been received much attention to replace the traditional lighting sources such as incandescent and fluorescent lamps [70,160]. The phosphor converted emission is one of the important approaches to produce efficient commercial w-LEDs with the combination of blue LED and yellow phosphor ($Y_3Al_5O_{12}$:Ce^{3+}). However, such type of phosphors has poor color rendering index (CRI) due to lack of red component in white light emission [5,161–163]. Moreover, n-UV phosphor converted LEDs have many potential advantages such as excellent color rendering index, light color tolerance and high conversion efficiency into visible light [52,164,165]. Pondering on the aforementioned points, we made an effort to prepare and investigate n-UV excited efficient germane red phosphors aptly suitable for w-LEDs.

The doping of rare earth ions in suitable host has always remained the most famous way to obtain the excellent luminescent properties. The effective energy transfer from host to rare earth ion can exhibit a rich optical phenomenon. Since, the partially filled 4f electrons of rare earth ions are well shielded from the surrounding chemical environment by 5s and 5p electrons, the emission arising from the 4f-4f transition composed a sharp line with relatively long lifetime [166,167]. Among all rare earth ions, the characteristics of $^5D_0 \rightarrow {}^7F_2$ transition of trivalent europium (Eu^{3+}) ion is one of the sources to obtain the red emission for lighting and display applications. Moreover, the nature of this transition line strongly depends on the local environment and can be exploited to review the site symmetry [168].

In the present chapter, Eu^{3+} doped $BaNb_2O_6$ powders have been synthesized by solid state reaction method to explore the utility and potential use as phosphor. However, to the best of our knowledge, the study of the optical/luminescent properties of europium doped barium niobates has not been reported so far. Structural and morphological and photoluminescent properties were analysed. Emission spectra

measured as a function of Eu^{3+} concentration and investigated the luminescence properties in detail for Eu^{3+} doped $BaNb_2O_6$.

5.2. Synthesis of Eu^{3+} doped $BaNb_2O_6$

The precursor chemicals $BaCO_3$, Nb_2O_5 and Eu_2O_3 were taken as starting materials. $BaNb_2O_6$: xEu^{3+} (x = 1, 4, 10, 12, 14 and 16 mol %) phosphors were synthesized by conventional solid state reaction method. The synthesis procedure adopted to prepare $BaNb_2O_6$: xEu^{3+} phosphor has been described in section 2.1.1 (Chapter 2) and Figure 2.4.

5.3. Results and Discussion

5.3.1. Structural and morphological analysis

Figure 5.1, represents the XRD pattern for the $BaNb_2O_6$ and $BaNb_2O_6$: xEu^{3+} (x= 1 and 12 mol %) sample sintered at 1200 $^{\circ}$C. All the diffraction lines are matching with the reported values of orthorhombic $BaNb_2O_6$ pattern of standard PDF4+ ICDD Card No. 04-012-8861. No other impurity peaks were detected, which indicates the formation of pure orthorhombic $BaNb_2O_6$ phase. The crystallite size (D) and strain (ε) of $BaNb_2O_6$ were calculated by most reliable Williamson - Hall (W-H) equation [94]. The average crystallite size and strain (%) were found to be 55, 54, 50 nm and 0.08, 0.087, 0.92, respectively for $BaNb_2O_6$: xEu^{3+} (x= 0.00, 1.0 and 12 mol%). Further the average crystallite size was calculated by conventional Debye- Scherer's equation [169], which is in good agreement with the crystallite size calculated from W-H method. The calculated lattice parameters was a= 7.845Å, b= 12.168 Å and c=10.253 Å for pure $BaNb_2O_6$ and which belongs to space group *$C222_1$ (20)* and volume (V)= 979.853 Å^3.

Figure 5.2 represents the SEM image for the optimized 12 mol % Eu^{3+} doped $BaNb_2O_6$ sample sintered at 1200 $^{\circ}$C. It was clearly seen from the figure that the particles are agglomerated with irregular morphology in the μm range. The typical crystalline grain size is in the range of 3-5 μm in dimension. The micrometre crystalline powder would be suitable to obtain high efficient phosphor and very much useful for solid state lighting applications [170].
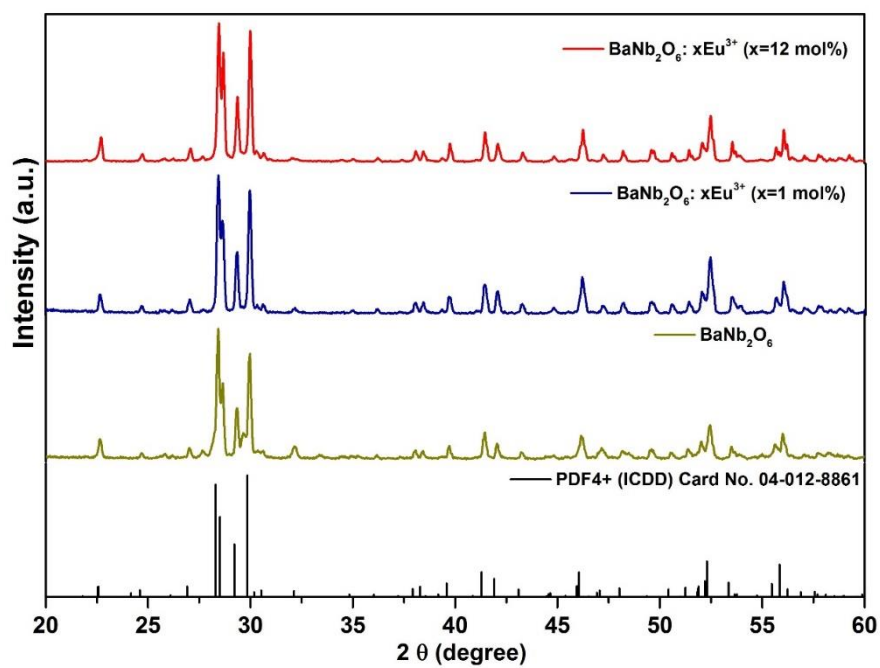
Figure 5.1. X-ray diffraction patterns of $BaNb_2O_6$: xEu^{3+} (x= 0, 1 and 12 mol%) phosphor sintered at 1200 $^{\circ}$C.
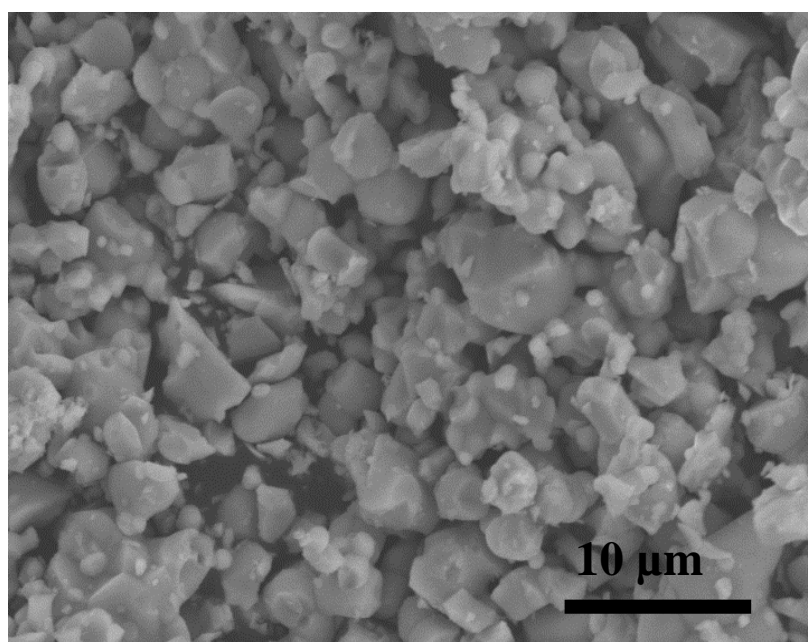
Figure 5.2. SEM image of $BaNb_2O_6$: xEu^{3+} (x = 12 mol%) phosphor.

5.3.2. Luminescent properties

Excitation spectrum of 12 mol% Eu^{3+} doped $BaNb_2O_6$ phosphor sintered at 1200 $^\circ$C is shown in Figure 5.3. The spectrum exhibits five bands due to intra 4f transitions of the Eu^{3+} ions and assigned as $^7F_0 \rightarrow ^5D_4$, $^7F_0 \rightarrow ^5L_7$, $^7F_0 \rightarrow ^5L_6$, $^7F_0 \rightarrow ^5D_3$ and $^7F_0 \rightarrow ^5D_2$ at wavelengths 362, 383, 395, 417 and 466 nm, respectively. The broad excitation band 325-360 nm may be attributed to the charge transfer band, which may be originated from an electron transfer from 2p orbital of an oxygen ligand to an empty 4f orbital of europium ion and the host charge transfer band occurs from an oxygen atom to the empty 4d orbital of the central niobium atoms within NbO_6 group [171]. The intense bands $^7F_0 \rightarrow ^5L_6$ (395 nm) and $^7F_0 \rightarrow ^5D_2$ (466 nm) observed in n-UV and blue regions, which confirms the existence of Eu^{3+} state in europium doped $BaNb_2O_6$ phosphor. Moreover, this phosphor is suitable to efficiently excite in n-UV and blue regions, which is one of the prerequisite properties to use this phosphor for preparation of w-LED devices.
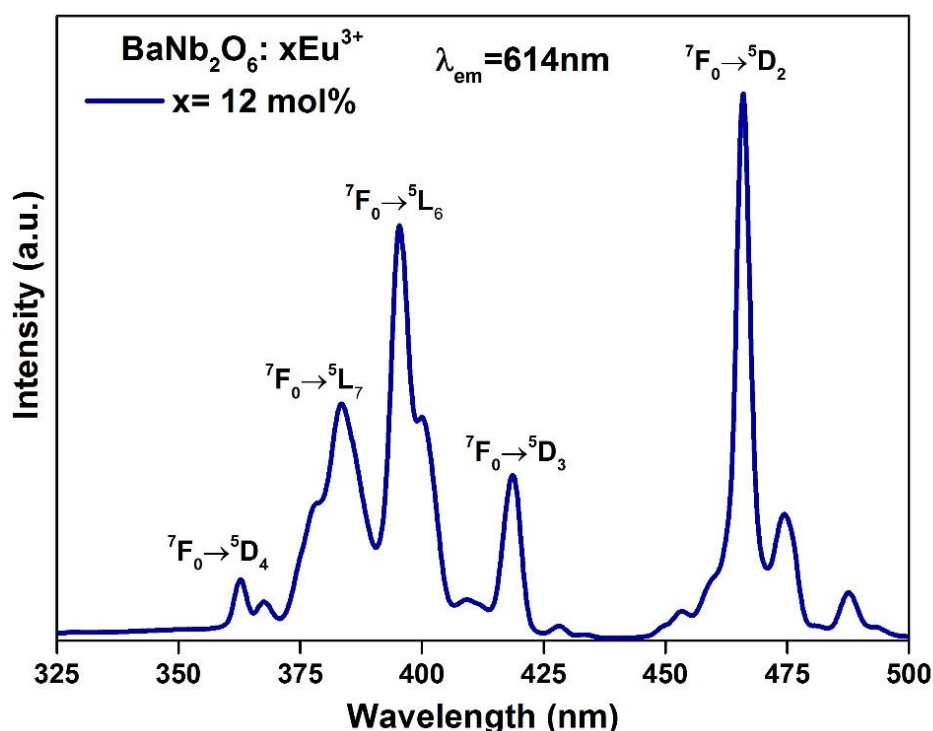
Figure 5.3. Photoluminescence excitation spectra (λ_{em}=614 nm) for $BaNb_2O_6$:xEu^{3+} (x= 12 mol%).

Figures 5.4 and 5.5 represent the emission spectra of Eu^{3+} doped $BaNb_2O_6$ phosphor for different concentrations of europium under 466 and 395 nm excitation wavelengths, respectively. Generally, magnetic dipole transition is allowed and electric dipole transition is forbidden as per the selection rule. But, forbidden electric dipole transition ($^5D_0 \rightarrow ^7F_2$) became partially allowed due to odd parity component of the crystal field in $BaNb_2O_6$:Eu^{3+}. The emission peak centred at 593 nm ($^5D_0 \rightarrow ^7F_1$) is attributed to magnetic dipole (MD) transition and intense emission peak at 615 nm ($^5D_0 \rightarrow ^7F_2$) is ascribed to electric dipole (ED) transition. But, weak transitions observed at 654 nm and 703 are assigned as ($^5D_0 \rightarrow ^7F_3$) and ($^5D_0 \rightarrow ^7F_4$), respectively. According to Judd-ofelt theory intensity distribution of $^5D_0 \rightarrow ^7F_J$ (where J=0, 1, 2, 3 and 4) transitions depends only on the symmetry of local environment around activator ions. Owing this property, some transitions are hypersensitive to the crystal environment and are called as hypersensitive transitions [172]. The emission intensity of the observed
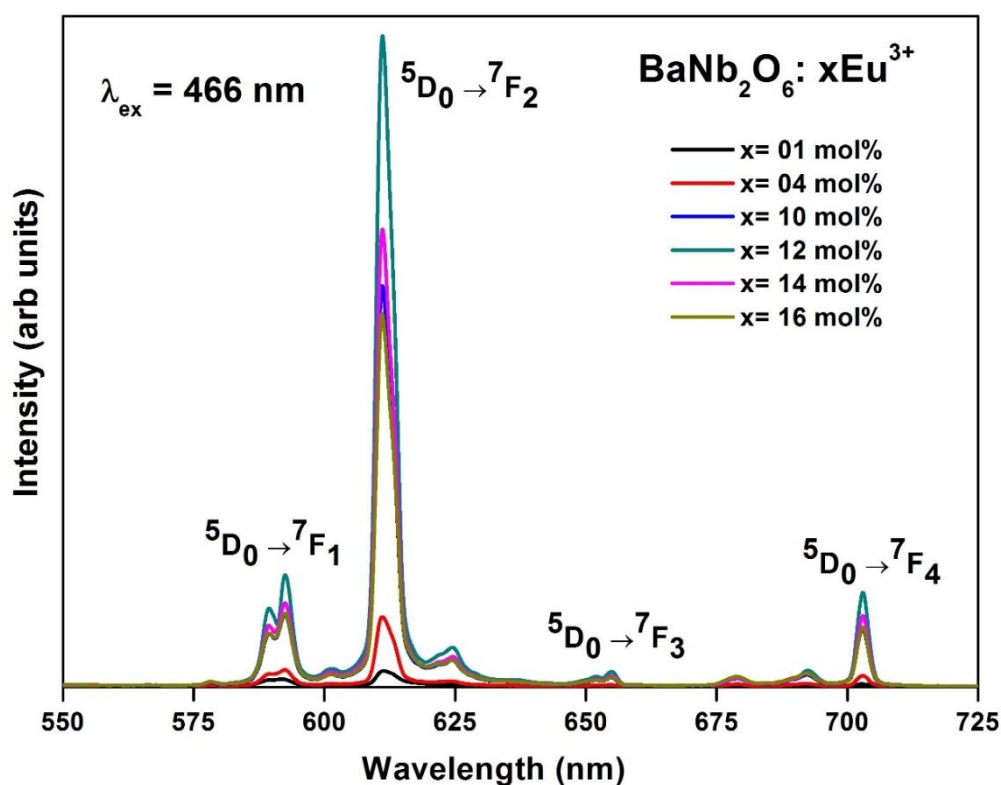
Figure 5.4. Emission spectra (λ_{ex}=466 nm) of $BaNb_2O_6$: xEu^{3+} (x= 1, 4,10,12,14 and 16 mol%).

bands is changing with Eu^{3+} ion concentrations whereas the shape of the emission band is not changing. It is well known that the trivalent lanthanides energy levels are weakly

affected by ligand ions in crystals because the 4f electrons are shielded by the external electric fields of the outer $5s^2 5p^6$ electrons.
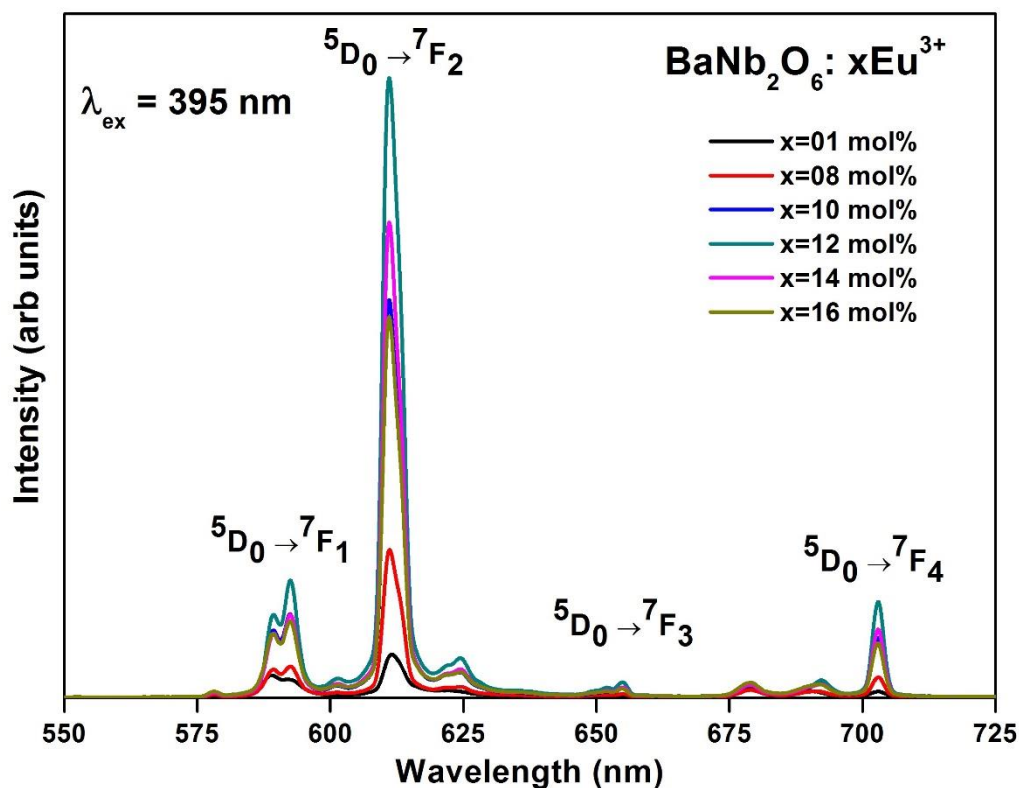
Figure 5.5. Emission spectra (λ_{ex}=395 nm) of BaNb$_2$O$_6$: xEu^{3+} (x= 1, 4,10,12,14 and 16 mol%).

Therefore, the shape of the optical spectra for most of the phosphors with the same lanthanide doping are similar to those expected for free ions [173]. Figure 5.6 shows the variation of emission intensity with Eu^{3+} concentration in the range from 1 to 16 mol% under the excitation of 466 nm. The intensity of all the observed emission bands increases with Eu^{3+} concentration by reason of energy migration among the activators up to 12 mol% and beyond this finally reached at killer site due to quenching mechanism associated with exchange interaction [50]. Such exchange of energy between the Eu^{3+} ions is obvious as the distance between them decreases with increasing Eu^{3+} ion concentrations [174].

The emission intensity of $^5D_0 \rightarrow ^7F_2$ transition is more intense than the $^5D_0 \rightarrow ^7F_1$ transition in BaNb$_2$O$_6$:Eu^{3+}. Therefore, the activator Eu^{3+} (0.95Å) occupies the Ba^{2+} (1.36Å) site without an inversion symmetry, which helps to improve the purity of red color [175]. Hence, Eu^{3+} can be a good luminescent activator for red phosphor due to
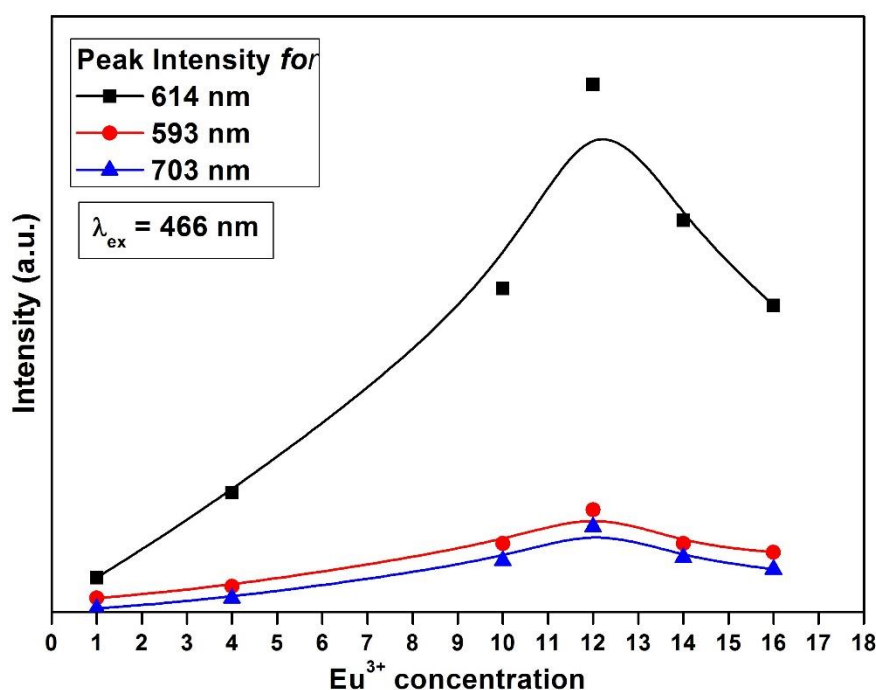
Figure 5.6. Variation of emission intensity with the Eu^{3+} concentration in $BaNb_2O_6$ phosphor.

the intense $^5D_0{\rightarrow}^7F_2$ transition centred at 614 nm based on the fact that red emission constituted by very narrow emission appear brighter than the broad red emission to human eye though the phosphor exhibiting same red chromaticity and emission energy [176]. The integrated Red (R)/Orange (O) ratio of electric dipole transition and magnetic dipole transition i.e. I ($^5D_0{\rightarrow}^7F_2$) /I ($^5D_0{\rightarrow}^7F_1$) have been calculated and named as asymmetric ratio. The obtained R/O ratio are found to be increase with Eu^{3+} concentration up to 12 mol% and considered that 12 mol % of Eu^{3+} as optimum R/O ratio 5.556 achieved for $BaNb_2O_6{:}Eu^{3+}$ phosphor [177].

The simplified energy level diagram is plotted in Figure 5.7 to demonstrate the mechanism involved in the emission and excitation processes in Eu^{3+} doped $BaNb_2O_6$ phosphor. When the Eu^{3+} ions were excited with 395 nm (to $^5L_6$ level) and 466 nm (to $^5D_2$ level) light, the population relaxes finally to the $^5D_0$ level through non-radiatively and then exhibit four emission bands in the visible region from $^5D_0$ level (shown with downward arrow) [178].

The color purity of the material can be estimated in terms of mathematically driven coordinates called CIE chromaticity coordinates. Figure 5.8 shows the CIE chromaticity diagram for optimized sample of 12 mol% Eu^{3+} doped $BaNb_2O_6$ phosphor

sintered at 1200 °C in an ambient atmosphere under 395 nm excitation. The calculated CIE color coordinates were found to be (x=0.628 and y=0.365), which falls in the pure red region suggests that the investigated phosphor may be used as red emitting phosphor for RGB composed w-LEDs. In addition to that, the calculated CIE chromaticity coordinates for $BaNb_2O_6:Eu^{3+}$ are closer to the commercial red phosphor of $Y_2O_2S:Eu^{3+}$ (x= 0.622, y= 0.351) and also close to the National Television Standard Committee (NTSC) standard value of red phosphor (x= 0.67, y= 0.33) [179].
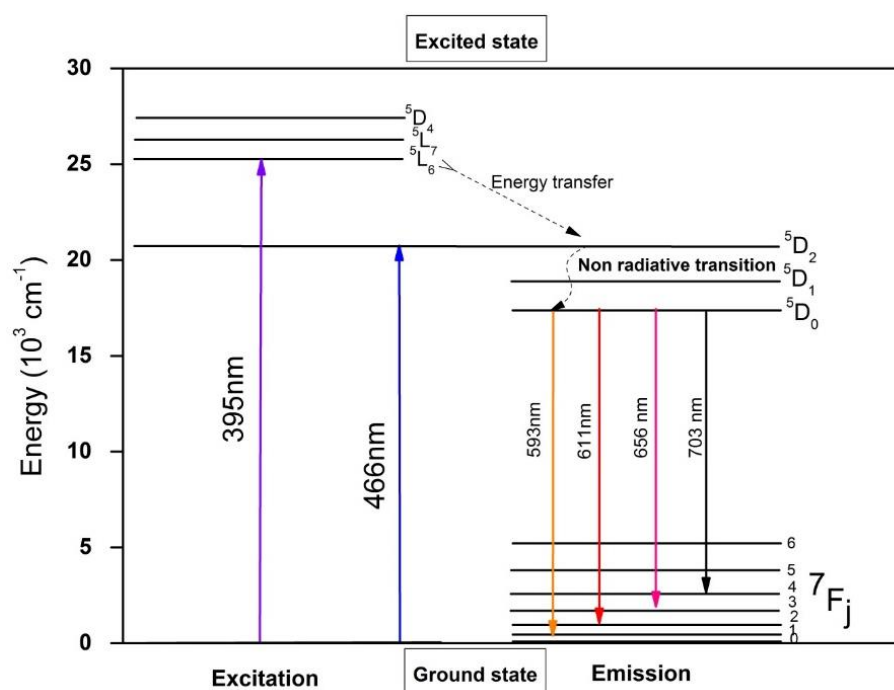
Figure 5.7. Simple model of illustrating the energy transfer mechanism and the emission process of Eu^{3+} in $BaNb_2O_6$.
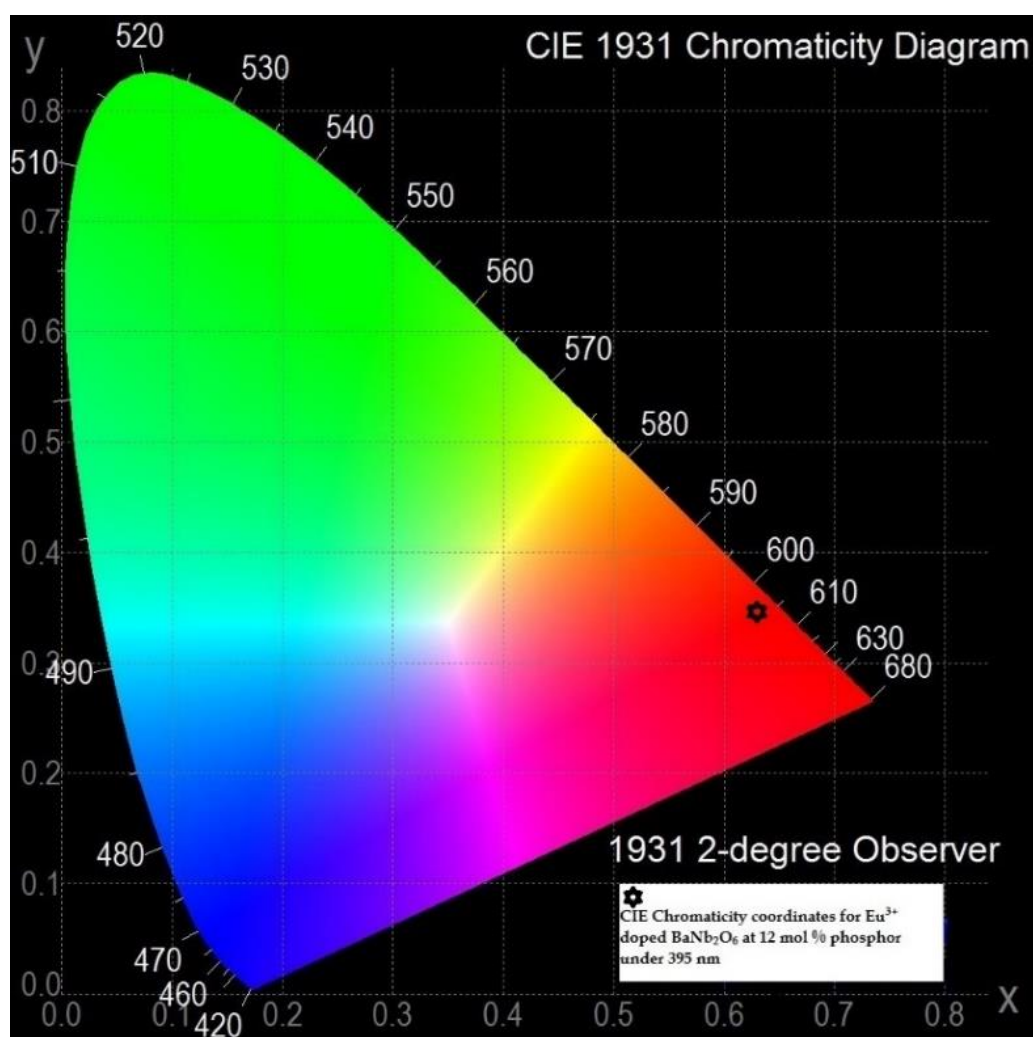
Figure 5.8. CIE chromaticity diagram for 12 mol% Eu^{3+} doped $BaNb_2O_6$ phosphor.

6

Significant Enhancement in Photoluminescent Properties of BaNb$_2$O$_6$: Eu^{3+} Phosphors *via* Flux Assisted SSR and MCG Methods

BaNb$_2$O$_6$: Eu^{3+} doped phosphors have been synthesized by flux assisted solid state reaction and metal citrate gel methods. The thermal, structural, morphological and luminescent properties of these phosphors were investigated. The orthorhombic crystal structure was confirmed by X-ray diffraction pattern and observed the irregular morphology of particles in SEM image with the particle size in micrometer (μm) range for the samples synthesized by flux assisted SSR method whereas the sample synthesized by MCG method exhibit nano regime particles. Absorption and excitation spectra exhibit the intense f-f transitions of Eu^{3+} ions in the n-UV and blue wavelength region. Photoluminescence studies reveal that the BaNb$_2$O$_6$: Eu^{3+} phosphors synthesized by flux assisted SSR and MCG methods significantly enhanced the emission intensity when compared to the phosphor prepared by conventional SSR method.
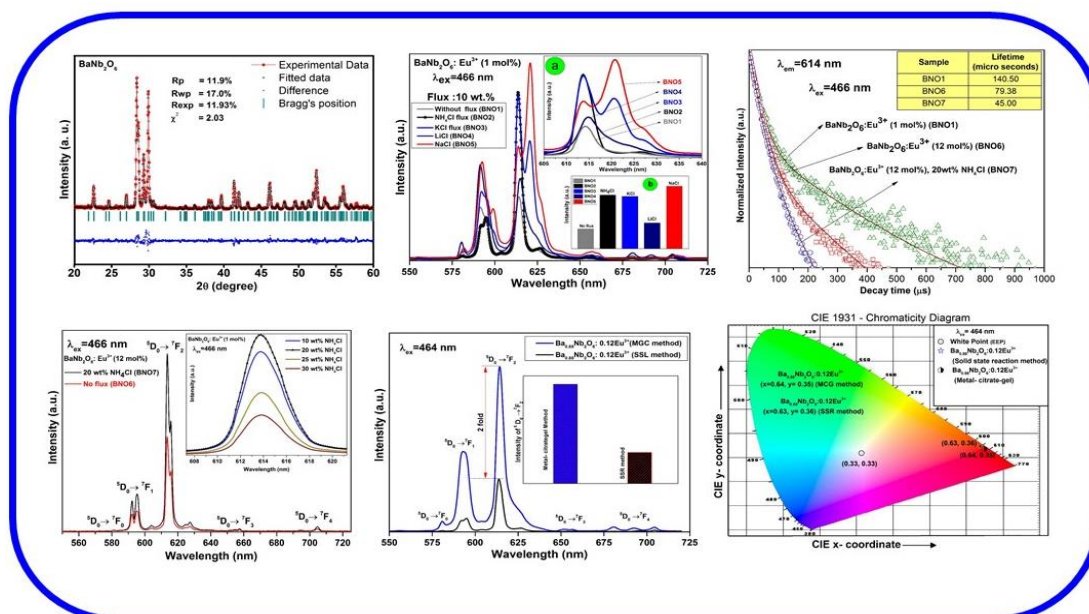
6.1. Introduction

Since the development of InGaN-based phosphor converted w-LEDs, SSL technology has flourished in designing a new generation of light sources for general illumination and display devices [160]. However, pc-w-LED has several serious issues, such as a poor color rendering index (Ra <65) due to lack of red emission and blue-yellow color separation [52,180,181]. In an attempt to improve the color rendering index, Wu et. al. [105], reported green and red light emitting sulfide phosphor coated on blue InGaN LED chip to obtain white light while Xie et. al. [182] described w-LEDs fabricated with red emitting nitride phosphor. Sulfide and nitride phosphors are still suffering from some shortcomings. Sulfide based phosphors exhibit chemical instability and low efficiency due to luminescence saturation with increasing applied current. The nitride phosphors exhibit a very broad and deep red emission that does not have high luminous efficacy, and also they require very high firing temperature and nitrogen pressure for their synthesis. The commercially available red emitting Y_2O_3: Eu^{3+} employed in w-LEDs has stable chemical and physical properties, but it has negligible absorption in the blue region (450-470 nm). Y_2O_3: Eu^{3+} phosphor has broadband excitation spectrum centered at 248 nm, which is due to charge transfer between the Eu^{3+} cations and surrounding ions. Therefore, there is a requisite to search for an efficient red emitting phosphor with strong absorption under n-UV/blue light to render the better color resulting from an ideal w-LEDs source [183–187].

In the previous Chapter (Chapter 5) $BaNb_2O_6$: Eu^{3+} phosphor have been synthesized and the results confirmed that this phosphor exhibit promising down conversion emission under n-UV and blue excitation sources [188]. Many of the researchers have devoted their efforts to enhance the luminescent properties of rare earth doped niobate phosphors. Recent research reports reveal that the blending of chloride salts known as flux along with rare earth dopants emerged as an effective way to enhance the emisison intensity and efficiency of the phosphors [189,190]. Fluxes not only improve the efficiency of trivalent rare earth ions but also play a significant role in the crystal growth. The improved luminescence intensity can be originated from the local crystal field symmetry breaking around rare earth ions by flux blending [191,192]. Recently, this method has been employed in several systems like $BaMgAl_{10}O_{17}$: Eu^{3+}

[193], $La_2Mo_2O_9$: Eu^{3+} [190], (Ba, Sr)$_2SiO_4$: Eu^{3+} [194] and $YNbO_4$: Eu^{3+} [195], to obtain enhanced luminescence properties.

In addition to this flux assited SSR method, it has been also widely accepted that size reduction of particles can improve the properties drastically due to the formation of enhanced surface states. In this pursuit, synthesis of nanophosphors has been drawn much attention. An application point of view, nanophosphors could be coat more times better than the bulk phosphors, which can provide fine grain control over the thickness of the film, and consequently this helps to improve the homogeneity as well as uniformity of the resultant film. Several other wet-chemical techniques have been employed such as solvothermal method, hydrothermal synthesis, a co-precipitation method, sol gel method, *etc.* for the synthesis of nanophosphors [107,196–198]. Among all these synthesis methods, citrate based sol gel technique (metal- citrate gel method) is advantageous due to cost effective and short operation time. The phosphor synthesized by citrate gel method exhibit high purity, excellent luminescence, good homogeneity relatively at low temperatures and ability to yield nano-sized powder [199].

Therefore, in the present Chapter, Eu^{3+} doped $BaNb_2O_6$ phosphors have been synthesized by the using various chloride fluxes (NH_4Cl, KCl, LiCl, and NaCl) in SSR method (flux assisted SSR method) and also synthesized via MCG method. Moreover, to the best of our knowledge, studies of Eu^{3+} doped $BaNb_2O_6$ phosphor by flux assisted SSR and MCG method have not been reported so far. The comparative investigation on structural, morphology, luminescent properties have been investigated in the present chapter. To examine the enhancement in emission intensity, the synthesized phosphors have been compared with phosphor prepared by solid state reaction method.

6.2. Synthesis of $BaNb_2O_6$: Eu^{3+} by Flux Assisted SSR and MCG Methods

The various fluxes incorporated $BaNb_2O_6$: Eu^{3+} phosphor powder samples were prepared by a conventional SSR method. The high purity Eu_2O_3, $BaCO_3$, Nb_2O_5 were taken as starting materials and pure (99.9%) NH_4Cl, KCl, LiCl, and NaCl chemicals were used as the flux in different weight ratios. The stoichiometric amount of $BaCO_3$, Nb_2O_5 along with various fluxes (in various wt% ratios) were weighed and mixed for an hour using acetone as a dispersing medium and the mixture placed in a

programmable muffle furnace. In the MCG method, Eu_2O_3, $NbCl_5$, Citric acid and Hydrogen peroxide were taken as starting precursors. The synthesis procedures for Eu^{3+} doped $BaNb_2O_6$ phosphors have been described in section 2.1.1 (*Figure 2.4*) and 2.1.2 (*Figure 2.5*) for SSR and MCG method, respectively.

6.3 Results and Discussion

6.3.1. BaNb₂O₆: Eu³⁺ phosphors synthesized by flux assisted SSR method

6.3.1.1. Structural analysis

Sample BNO1 stands for 1 mol% Eu^{3+} doped $BaNb_2O_6$, whereas BNO2, BNO3, BNO4 and BNO5 represents the $BaNb_2O_6$: xEu^{3+} (x= 1 mol%) powder blended with 10 wt% amount of NH_4Cl, KCl, LiCl, and NaCl fluxes, respectively. X-ray diffraction patterns measured for as-prepared BNO1, BNO2, BNO3, BNO4 and BNO5 phosphor samples are as shown in Figure 6.1. The sharp and intense diffraction pattern indicate the crystalline nature of samples. All the observed peaks of BNO1, BNO2, and BNO3 samples exhibit similar kind of diffraction patterns, which are in good agreement with the standard PDF4+ ICDD card No. 04-012-8861. The presence of no impurity peaks were present, which confirmed the formation of single phase orthorhombic crystal structure of $BaNb_2O_6$ with space group $C222_1$ (20). However, the observed peaks of BNO4 and BNO5 phosphor samples represent some other phases. The phases have been identified by standard JCPDS card and found to be well matched with $Ba_2LiNb_5O_{15}$ (Card No. 00-037-1077) and $Ba_2NaNb_5O_{15}$ (Card No. 00-034-0210) for BNO4 and BNO5, respectively. In the BNO2 sample, the NH_4Cl firstly lower the decomposition temperature of carbonates and then takes place in chemical reaction process to accelerate the kinetics of the phase formation as the flux. During the chemical reaction, NH_4Cl may be broken into NH_3 and HCl at 300 °C and could increase the diffusion rate between $BaCO_3$ and Nb_2O_5 to form the highly crystalline europium doped $BaNb_2O_6$ phosphor at 1200 °C [192,200]. Due to the above mentioned reason, BNO2 sample exhibits the single phase of $BaNb_2O_6$. BNO3 sample represents the pure phase, which may be due to the similar ionic radius of K^+ (1.38 Å, CN=6) and Ba^{2+} (1.36 Å, CN=6). Therefore, K^+ ion could successfully substitute the Ba^{2+} site [201]. In the case of BNO4 and BNO5 samples, the ionic radius of Li^+ (0.78 Å, CN=6) and Na^+ (1.02 Å,

CN=6) is very small as compared to Ba^{2+} (1.36 Å, CN=6). The mismatch in ionic radii may be expected to be one of the main reasons for forming unknown phase along with $BaNb_2O_6$ phase.
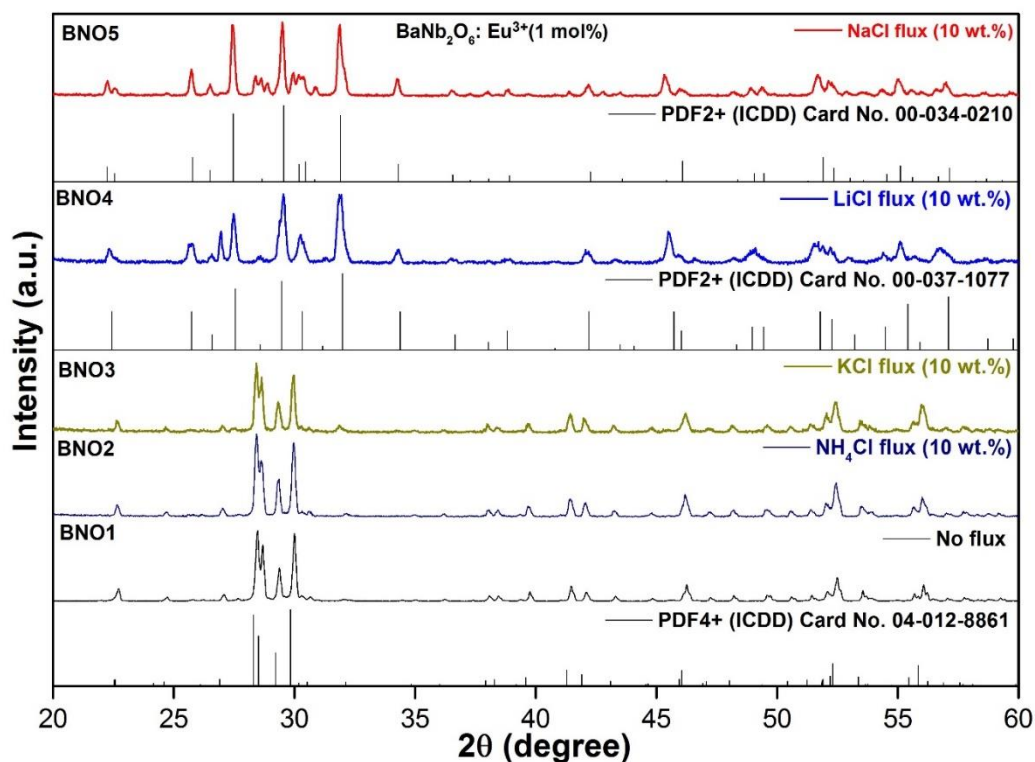
Figure 6.1. X-ray diffraction pattern of various flux blended Eu^{3+} doped $BaNb_2O_6$ phosphors synthesized at 1200 °C.

Figure 6.2 shows the XRD patterns of BNO, BNO6, and BNO7 samples. BNO only represents $BaNb_2O_6$ powder without any dopant or flux. BNO6 represents the 12 mol% of Eu^{3+} doped $BaNb_2O_6$, whereas BNO7 represents the same 12 mol% of Eu^{3+} doped $BaNb_2O_6$ blended with excess 20 wt% NH_4Cl flux. All the peaks of BNO, BNO6, and BNO7, are well matched with the standard PDF4+ ICDD card No. 04-012-8861. No anonymous peaks were observed in BNO6 and BNO7 samples even by adding 12 mol % Eu^{3+} ion and 20 wt% NH_4Cl flux. The above results confirm that the influence of Eu^{3+} and NH_4Cl was negligible on the crystal structure of $BaNb_2O_6$ [200,202]. Furthermore, crystallite sizes were calculated for the intense peak by using well-known Debye- Scherer's equation [167,188] [$D = 0.94\lambda/\beta Cos\theta$], where D is the average crystallite size, λ is the X-ray wavelength (1.5406 Å), 0.94 is shape factor, β is full width half maximum and θ is the diffraction angles of the observed peaks. The calculated average crystallite size for BNO, BNO1, BNO2, BNO3, BNO4, BNO5,

BNO6 and BNO7 are approximately 54, 52, 43, 39, 33, 38, 42 and 40 nm, respectively. As BNO7 sample exhibits intense diffraction patterns indicate the better crystallinity than other samples, which may affect the luminescent properties.
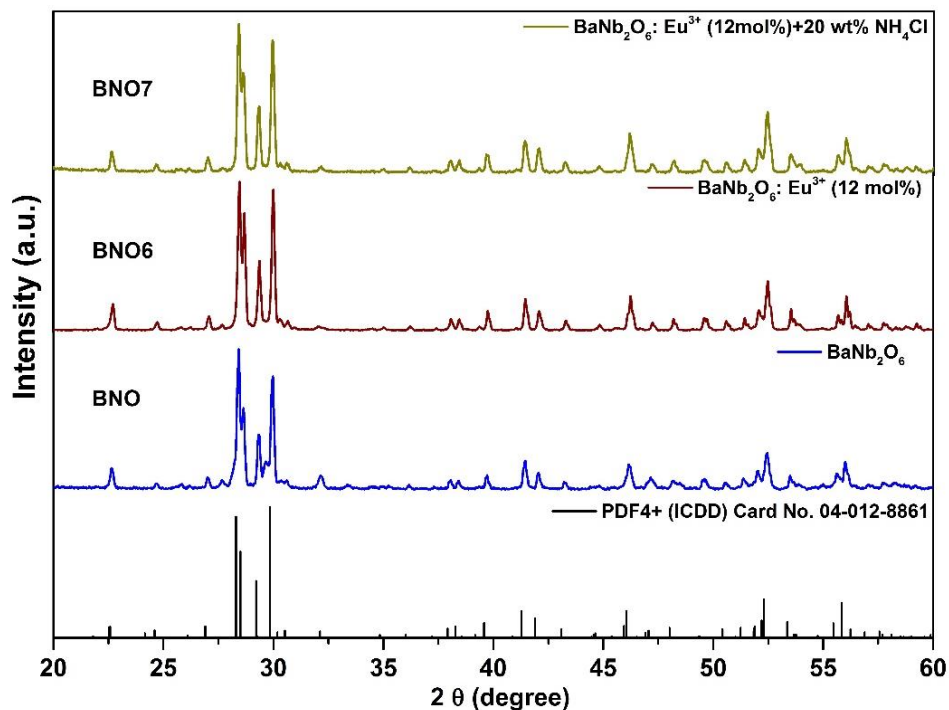
Figure 6.2. X-ray diffraction patterns of BNO, BNO6 and BNO7 samples.

In order to obtain the crystallographic information Rietveld refinement, [96,187,203] of BNO, BNO6 and BNO7 samples were carried out via FullProf Suite software. The profile was fitted using Pseudo- Voigt profile function. The observed, calculated and difference of powder diffraction pattern and Bragg positions of the BNO, BNO6 and BNO7 samples are shown in Figure 6.3 (a-c), respectively. From the Rietveld refinement results, no impurity phase were identified and the obtained goodness of fit (χ^2) were found to be 4.3, 3.59 and 1.91 for BNO, BNO6 and BNO7 samples, respectively. The results are well matching with published data by Sirotinkin *et al*. and the calculated lattice parameters are summarized in Table. 6.1. The cell volume of BNO6 and BNO7 were found to be little bit higher than that of BNO due to Eu^{3+} doping and incorporation of NH_4Cl flux. Figure 6.3 (d) displays the three-

dimensional crystal structure rendered with VESTA software. This $BaNb_2O_6$ structure belongs to the orthorhombic structure with space group $C222_1$ (20) [149].
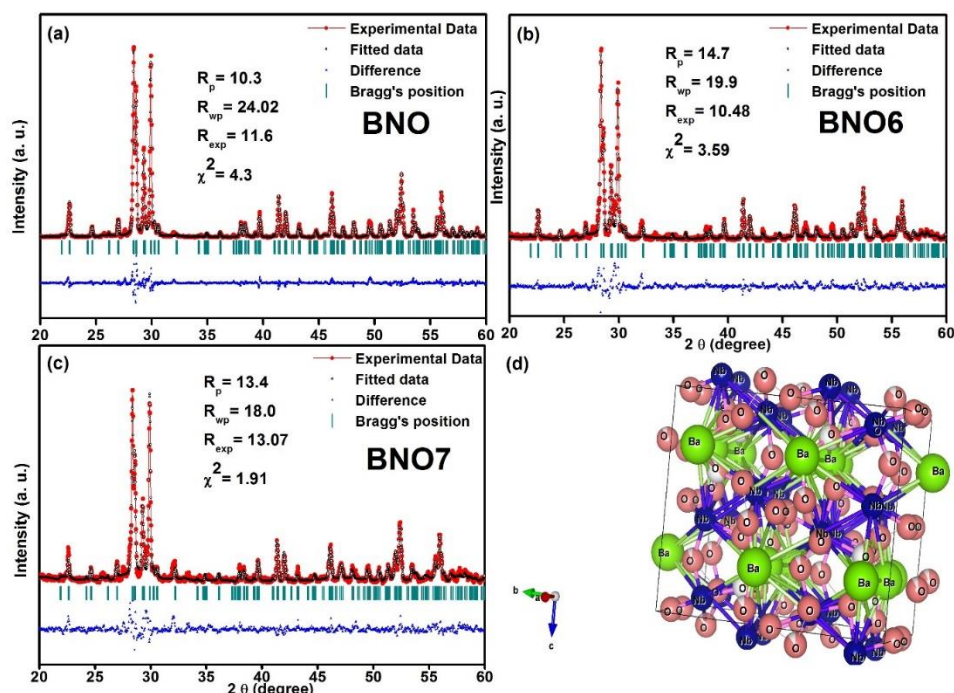
Figure 6.3. Rietveld refinement of **(a)** BNO, **(b)** BNO6 **(c)** BNO7 and **(d)** Crystal structure of $BaNb_2O_6$.

Table. 6.1. Calculated crystallographic information of BNO, BNO6 and BNO7 samples by Rietveld refinement method.

Sample No.	BNO	BNO6	BNO7
Radiation	Cu-K$_\alpha$		
2 theta	20-60		
Crystal structure	Orthorhombic		
Space group	$C222_1(20)$		
a (Å)	7.8552	7.8627	7.8637
b (Å)	12.1882	12.1904	12.2005
c (Å)	10.2696	10.2748	10.2803
α (degree)	90		
β (degree)	90		
γ (degree)	90		
R$_{exp}$ (%)	11.62	10.48	13.07
R$_p$ (%)	10.30	14.70	13.40
R$_{wp}$ (%)	24.20	19.90	18.00
GOF (χ^2)	4.3	3.59	1.91
Volume (Å^3)	983.233	984.850	985.413

6.3.1.2. Scanning electron microscopy observations

The typical SEM images of BNO1, BNO2, BNO6, and BNO7 phosphor samples prepared at 1200 ℃ are shown in Figure 6.4 (a-d). All the observed SEM pictures for BNO1, BNO2, BNO6 and BNO7 indicate the irregular shape of the uneven distribution of particles in micrometer (µm) range.
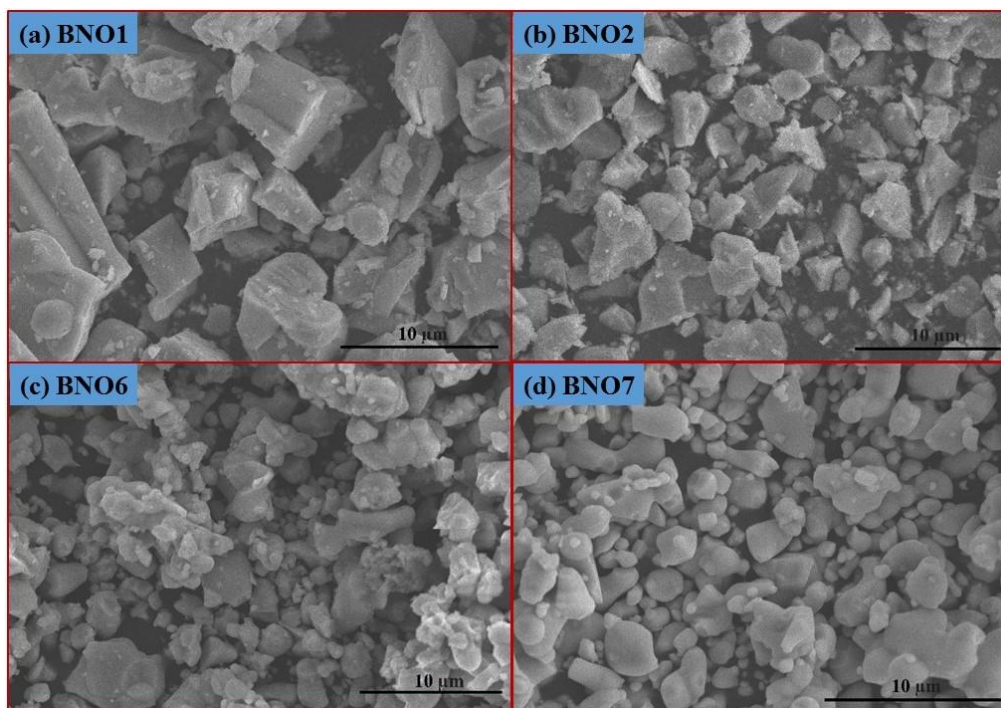
Figure 6.4. SEM micrographs of (a) BNO1, (b) BNO2, (c) BNO6 and (d) BNO7 samples.

The overall morphology of the samples BNO1 and BNO2 is more or less similar, but the particle size is decreasing with the incorporation of flux in 1 mol% Eu^{3+} doped $BaNb_2O_6$ phosphor. However, the sample BNO7 displays more fine particles within the range of 1-2 µm due to the influence of 12 mol% Eu^{3+} doping concentration and 20 wt% NH_4Cl flux. Actually, the chloride fluxes help us to synthesize the powder with desirable properties, including the crystal growth, shape, high purity and good chemical homogeneity which is due to fast evaporation or decomposition of fluxes, along with the rapid nucleation of the compound during the reaction at high temperature [191]. In SEM pictures, the observed particles are not uniform in size and has irregular morphology are mainly due to solid state reaction. Besides melting point or decomposition temperature, other parameters of fluxes such as solubility of raw materials, ionic radii of anion/cation, as well as purity of flux, may also have a

significant effect on size, morphology, and luminescent properties of materials [48,166]. Based on above reasons and explanation, it is could be suggested that the fluxes have a significant role in the growth and crystallinity of the synthesized phosphors. This observation is also in agreement with the results of XRD.

6.3.1.3. Band gap measurements

Diffuse reflectance spectra of BNO1, BNO6, and BNO7 phosphor samples are shown in Figure 6.5 in the range of 300 to 550 nm.
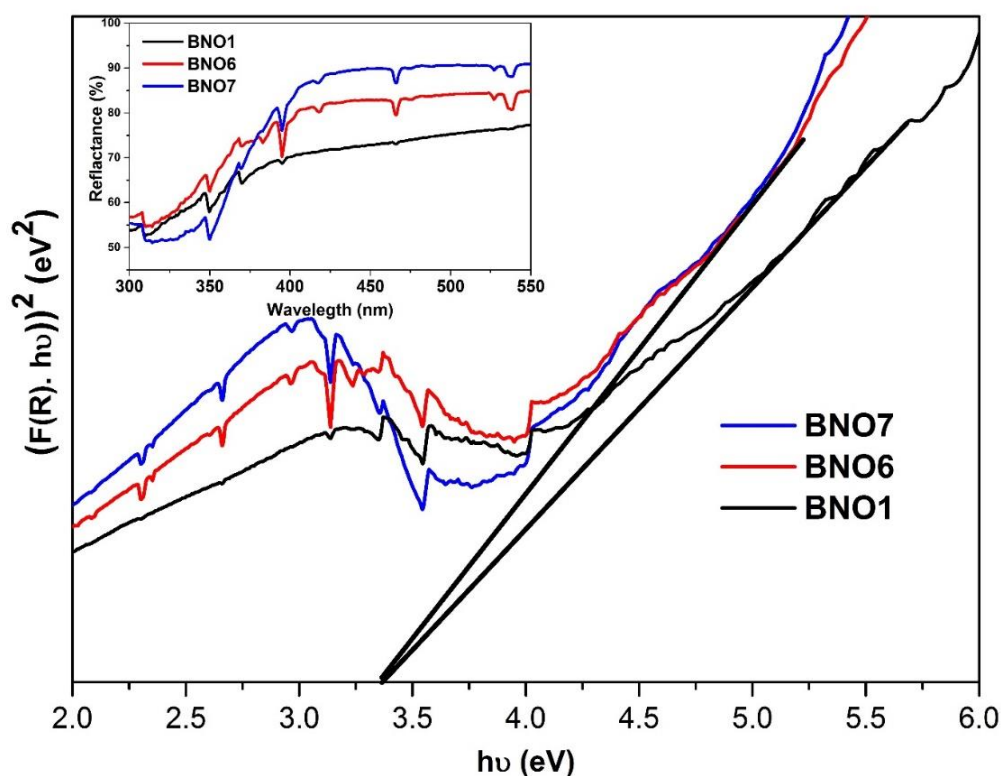
Figure 6.5. Optical band gap (E_g) estimation of BNO1, BNO6 and BNO7 via Kubelka-Munk function.

All the samples exhibit strong absorption bands at 362, 383, 395, 466 and 532 nm corresponding to $^7F_0 \to {}^5D_4$, $^7F_0 \to {}^5G_2$, $^7F_0 \to {}^5L_6$, $^7F_0 \to {}^5D_2$, and $^7F_0 \to {}^5D_1$ transitions of Eu^{3+} ions, respectively as shown in the inset of Figure 6.5 [101,183]. The band gap of BNO1, BNO6, and BNO7 samples were estimated according to the equation [204]:

$$[F(R)hv]^n = A(hv - E_g)$$

where hυ is the photon energy, A is a proportional constant, E_g is the value of the band gap, n=2 for direct transition or ½ for indirect transition, and F(R) is a Kubelka-Munk function defined as [186,205]

$$F(R) = \frac{\alpha}{S} = \frac{(1-R)^2}{2R}$$

where R, α, and S are the reflectance, absorption, and scattering coefficient, respectively. Since the scattering coefficient is wavelength independent, F(R) is proportional to α. From the linear extrapolation of $[F(R)h\upsilon]^2$=0, the estimated E_g values are found to be about 3.37 eV for BNO1, BNO6 and BNO7 as shown in the Figure 6.5, which is in good agreement with calculated band gap by *Cho et al.* [63] for pure $BaNb_2O_6$ sample. Hence, it confirms that the band gap of the samples is not affected by adding Eu^{3+} concentration and also fluxes.

6.3.1.4. *Photoluminescence excitation and emission spectra*
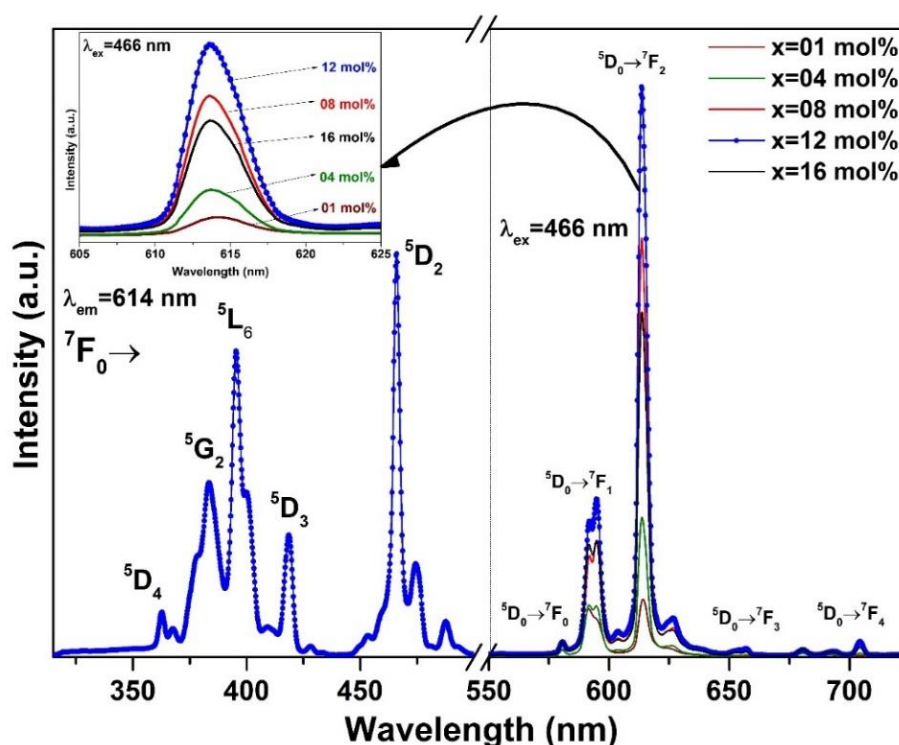
Figure 6.6. Photoluminescence excitation spectrum and emission spectra of Eu^{3+} doped $BaNb_2O_6$ phosphors.

Figure 6.6 represents the photoluminescence excitation and emission spectra of $BaNb_2O_6$: Eu^{3+} phosphors, which are measured in the spectral region from 315 to 525 nm and 550 to 750 nm, for excitation and emission, respectively. The peaks

observed in the excitation spectrum are well matched with the peaks in the absorption spectrum. The properties/characteristic features of photoluminescence excitation and emission spectra have been discussed in section 5.3.2.

6.3.1.5. Influence of chloride fluxes on luminescence intensity

The fluxes play a significant role in the enhancement of the luminescence intensity and has a vital role in promoting grain growth and improvement in crystallinity [189]. Figure 6.7 shows the modulation in emission spectra of 1 mol% of Eu^{3+} doped $BaNb_2O_6$ as a consequence of various fluxes in BNO1, BNO2, BNO3, BNO4 and BNO5 phosphor samples under 466 nm excitation wavelength. It was observed that the emission intensity of flux assisted phosphor is significantly enhanced with various chloride fluxes. In the Figure 6.7 (a), emission spectra of BNO1 and BNO2 samples exhibit similar profile with variation in intensity. However, the emission of BNO4 is slightly shifted toward higher wavelength. The emission intensity of BNO2 and BNO3 increased two times than that of BNO1 phosphor. On the other hand, the emission intensity of BNO5 sample with NaCl flux enhanced significantly, about three times and shifted toward higher wavelength (red shift). The redshift was observed due to crystal field splitting in BNO4 and BNO5 phosphor, which leads to distorting the crystal symmetry [206]. Very less enhancement in emission intensity has been observed in BNO4 emission intensity with LiCl flux. Moreover, the remarkable enhancement was observed in the emission intensity of sample BNO2 (blended with NH_4Cl flux) and exhibit similar spectrum profile and phase with the BNO1 phosphor. Based on the above result, NH_4Cl was found to be a suitable flux for the synthesis of Eu^{3+} $BaNb_2O_6$ phosphor, and it gave the strongest and enhanced red emission without altering the crystal structure and emission profile. Figure 6.7 (b) represents the intensity variation with various flux in a bar graph. The above results are entirely consistent with X-ray diffraction results and based on especially purity of the phase.

In our study, the flux NH_4Cl accelerates the kinetics of formation of the phosphor by enhancing the diffusion coefficient. More flux could form more liquid to obtain a sufficient diffusion of atoms [192,202]. It is evident from the Figure 6.8 (b), no shift has been observed in the emission line of increasing flux density up to 30 wt% of NH_4Cl in 1 mol% Eu^{3+} doped $BaNb_2O_6$. However, it can be noted that the luminescence intensity of 1 mol% Eu^{3+} doped $BaNb_2O_6$ significantly enhanced up to

20 wt% NH_4Cl flux, beyond that intensity decreases. This phenomenon caused may be due to more quantity of chloride flux creates more impurities, and it may act as a killer to the luminescent properties [192]. Figure 6.8 (a) shows the relative emission spectra of BNO6 and BNO7 phosphor samples at 466 nm excitation wavelength. Both the emission spectra resembles the same shape and position with variation in intensities. The emission intensity of BNO7 phosphor is enhanced more than two times and exhibit intense red emission in comparison to BNO6 phosphor (optimized sample based on dopant concentration without flux) without disturbing the crystal structure of host lattice. Therefore, the conclusion has been drawn that, among all the fluxes, NH_4Cl gives better emission and found to be very much suitable flux with $BaNb_2O_6$: Eu^{3+} phosphor to design red phosphor for the solid state lighting devices under n-UV /blue LED chip excitation.
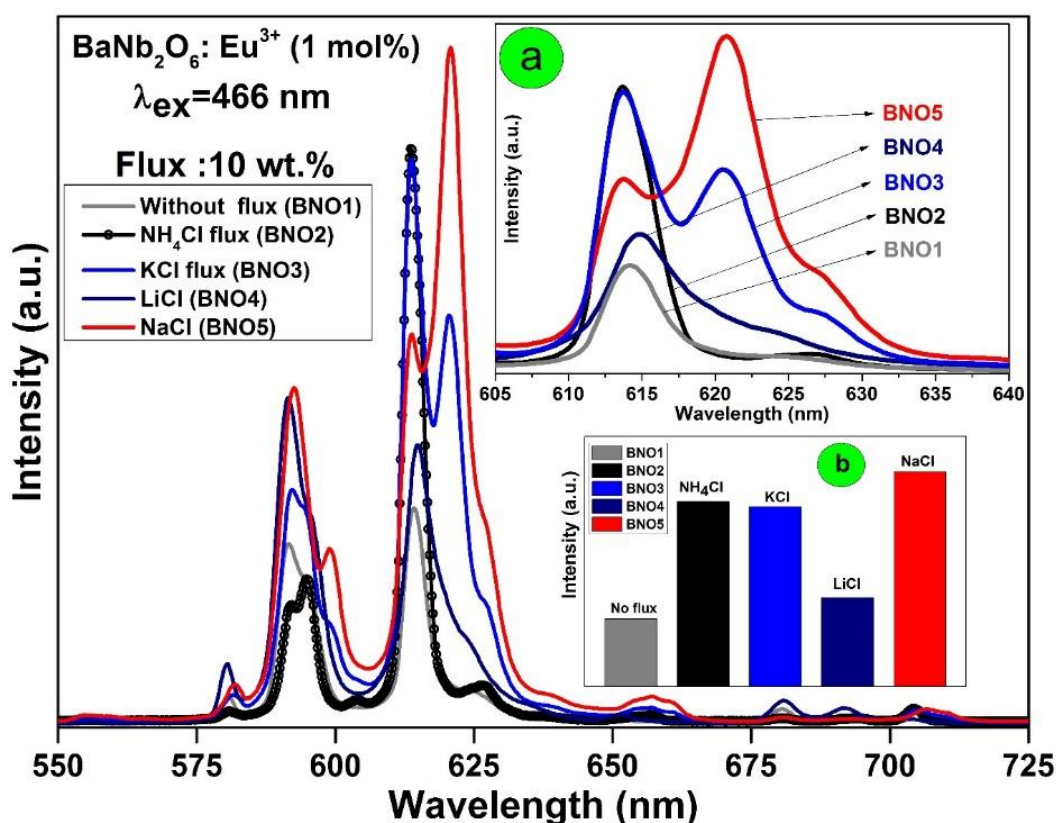
Figure 6.7. Photoluminescence spectra of $BaNb_2O_6$: xEu^{3+} (x=1 mol%) and blended with 10 wt% NH_4Cl, LiCl, KCl and NaCl fluxes. **(a)** Enlargement of the PL spectra in the region from 605 to 640 nm **(b)** Bar graph intensity with various flux.
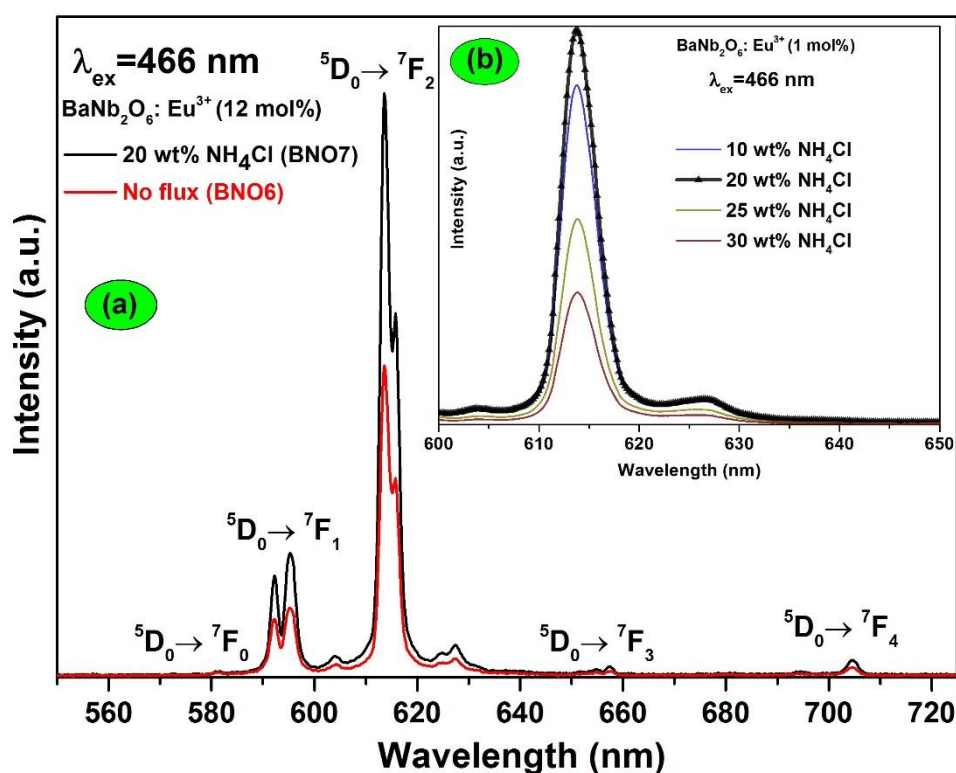
Figure 6.8. Photoluminescence spectra of BNO6 and BNO7 phosphors (Inset: BaNb2O6: xEu^{3+} (x=1 mol%) blended with different weight ratios of NH4Cl flux).

It is well known that the electric dipole transition dominates in the emission spectra when Eu^{3+} ions are situated at low symmetry site, as in Table. 6.2, flux doped phosphors are not an exception to this trend. It was observed that the intensity of red emission was greater than that of orange emission. Therefore, the calculated asymmetric ratios R/O = ($^5D_0{\rightarrow}^7F_2$)/ ($^5D_0{\rightarrow}^7F_1$) were given in Table 6.2. The intensity ratio represents the degree of distortion of the inversion symmetry of the local environment around the Eu^{3+} ions in the host and is known as an asymmetric ratio [183,207]. The asymmetric ratio of all the samples were estimated by the area under the peak ($^5D_0{\rightarrow}^7F_2$) and ($^5D_0{\rightarrow}^7F_1$) transitions of the 614 and 593 nm emission bands, respectively. The magnitudes of asymmetric ratios for the samples BNO1, BNO2, BNO6, and BNO7 are approximately higher and improving with the flux and dopant concentration, which suggest an improvement in purity of red color. The CIE chromaticity coordinates of the BNO1, BNO2, BNO3, BNO4, BNO5, BNO6 and BNO7 phosphors were investigated under the excitation wavelength 395 and 466 nm

respectively. The calculated CIE coordinates for all samples tabulated in Table. 6.2 and located in the pure red region except BNO4.

Table 6.2. Asymmetric ratios and CIE chromaticity coordinates for BNO1, BNO2, BNO3, BNO4, BNO5, BNO6 and BNO7.

Sample No.	Sample Name	Flux content		Asymmetric ratio (R/O)	CIE chromaticity coordinates (x, y)	
		Name	(wt%)		395 nm	466 nm
BNO1	$BaNb_2O_6$: Eu^{3+} (1 mol %)	No flux	-	4.50	(0.63, 0.36)	(0.65, 0.35)
BNO2		NH_4Cl	10	3.95	(0.63, 0.35)	(0.65, 0.35)
BNO3		KCl	10	2.41	(0.65, 0.35)	(0.65, 0.35)
BNO4		LiCl	10	0.82	(0.62, 0.38)	(0.63, 0.37)
BNO5		NaCl	10	1.99	(0.65, 0.35)	(0.65, 0.35)
BNO6	$BaNb_2O_6$: Eu^{3+} (12 mol %)	No flux	-	4.75	(0.64, 0.35)	(0.65, 0.35)
BNO7		NH_4Cl	20	4.75	(0.64, 0.35)	(0.65, 0.35)

The CIE chromaticity coordinates for optimized BNO7 phosphors was found to be (0.65, 0.35) under 466 nm excitation as shown in Figure 6.9., which is equal to the commercial red emitting Y_2O_3: Eu^{3+} phosphors (0.65, 0.35). The color purity [149] of the synthesized samples were calculated using the formula:

$$\text{Color purity} = \frac{\sqrt{(x_s - x_i)^2 + (y_s - y_i)^2}}{\sqrt{(x_d - x_i)^2 + (y_d - y_i)^2}} \times 100\%$$

where, (x_s, y_s) are the coordinates of sample point (x_d, y_d) are the coordinates the dominant wavelength and (x_i, y_i) are the coordinates of the illuminant point. In BNO7 phosphor, $(x_d, y_d) = (0.65, 0.35)$ for the dominant wavelength at 614 nm. The calculated color purity was found to be 99.5% pure, which confirms the pure red light emission.
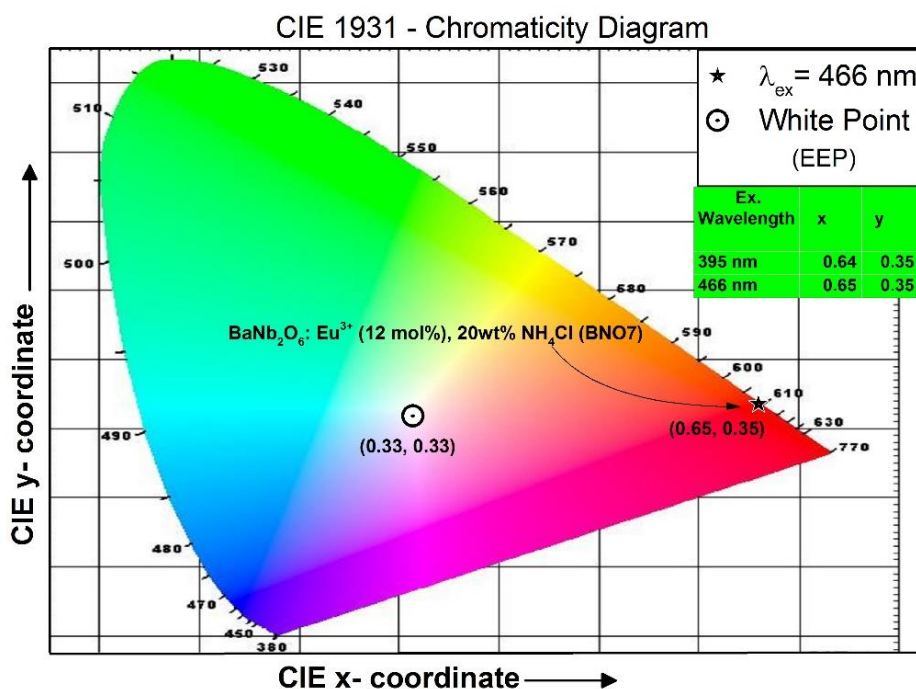
Figure 6.9. CIE chromaticity coordinates of optimized BNO7 phosphor.

6.3.1.6. Lifetime measurements

The lifetime measurements have been carried out to get the idea regarding the energy transfer mechanism involved in the emission process. The decay profiles were recorded for prominent red emission transitions $^5D_0 \rightarrow ^7F_2$ (at 614 nm) of Eu^{3+} ions under 466 nm excitation for BNO1, BNO6, and BNO7 samples as shown in Figure 6.10. The decay curves well fitted by using the bi-exponential decay function for all samples. The calculated average lifetime of samples BNO1, BNO6 and BNO7 were found to be 140.5, 79.38 and 45 μs, respectively. The bi-exponential nature and decrease in lifetime with increasing dopant concentration and flux suggest that the energy transfer processes are active in the present system. The lifetime is in the order of microseconds suggested that this phosphor could be a potential candidate for various display devices and lighting applications.
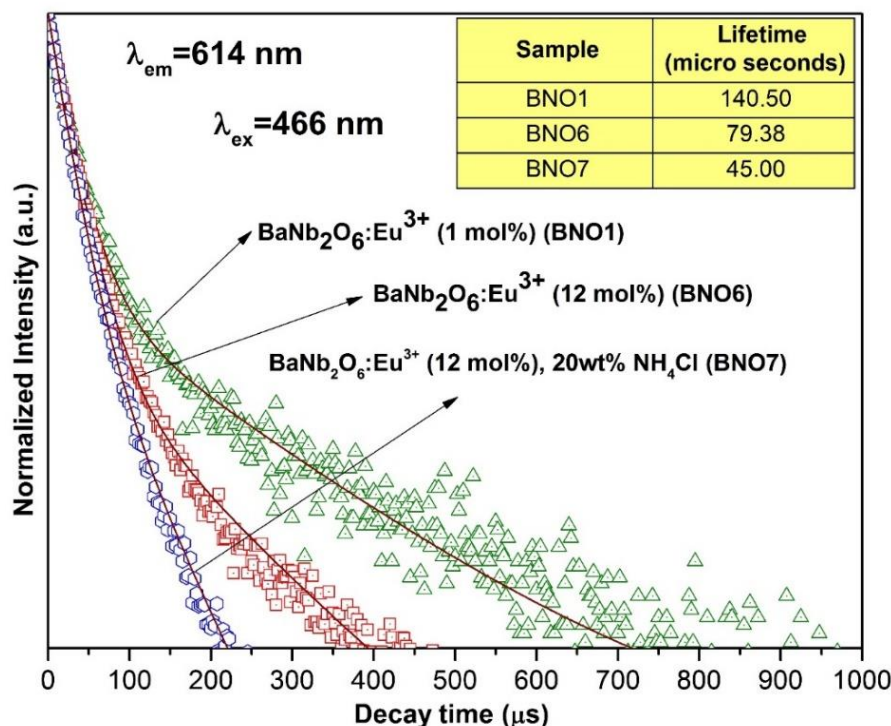
Figure 6.10. Lifetime decay curve of BNO1, BNO6, and BNO7 phosphor samples.

6.3.2. BaNb₂O₆: Eu³⁺ nanophosphors synthesized by MCG method

6.3.2.1. Thermal studies

The thermal behavior of as synthesized $BaNb_2O_6$ dried powder was investigated by TGA-DSC graph as shown in Figure 6.11. Dehydration, oxidation, combustion, and crystallization are the most significant thermal reactions perceived in TGA-DSC curve [208,209]. The overall weight loss were observed in two stages, and the total weight loss was about 61.6 % of the total precursor mass. The first stage of weight loss was about to 53.8 % observed in the temperature range 150-450 °C, which is associated with the broad endothermic bump shown in DSC. This behaviour is due to the dehydration of water and moisture present in the gel. In second stage weight loss was about 7.8 % in the temperature range of 450-630 °C corresponding to the sharp endothermic peak at 503 °C as shown in DSC curve could be attributed to the removal of carbonaceous impurities and decomposition of organic compound (citric acid). After 630 °C, no significant weight loss was observed. Minute/Tiny endothermic peak was observed at 722 °C due the evaporation of CO_2 gas. Moreover, the exothermic peak at 925 °C and 953 °C could be allocated to the crystallization peak/ phase formation of

the amorphous gel into crystalline nanoparticles of $BaNb_2O_6$ [210]. Based on the TGA-DSC profile dried gel was sintered at 1000 °C for 3 h.
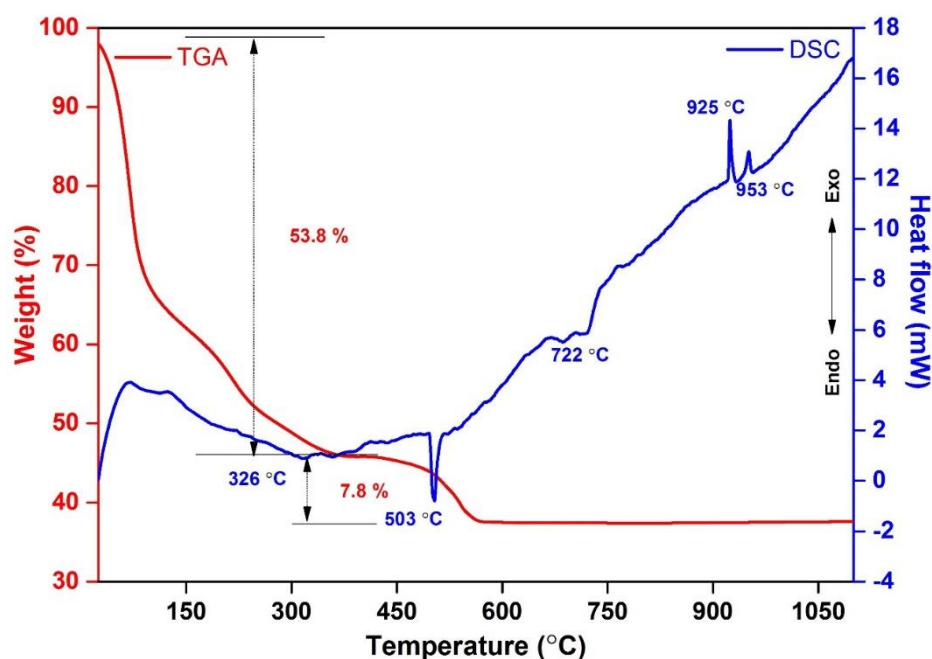
Figure 6.11. TGA-DSC profile for $BaNb_2O_6$ powder prepared by MCG method.

6.3.2.2. Structural analysis

Figure 6.12 (a) represents the X- ray diffraction pattern of as-synthesized powder fired at 400 °C, which exhibits the amorphous nature of dried gel powder. Figure 6.13 (b-d) represents the diffraction pattern of $BaNb_2O_6$: xEu^{3+}(x= 0, 1 and 12 mol%), phosphors calcined at 1000 °C for 3 h. All the diffraction peaks are well indexed and consistent with the standard PDF4+ (ICDD) Card No. 04-012-8861 of $BaNb_2O_6$ [149]. Moreover, no impurity phase was observed in diffraction pattern indicating that pure phase formation of $BaNb_2O_6$ [211]. Hence, the Ba^{2+} (1.36 Å) site seems to be replaced by Eu^{3+} (0.95 Å) ions in host lattice successfully without changes in the basic crystal structure of $BaNb_2O_6$. The average crystallite size and strain were obtained by the graph $\beta Cos\theta/\lambda$ versus $4Sin\theta/\lambda$ as shown in Figure 6.13. The average crystallite size and strain (%) for $BaNb_2O_6$: xEu^{3+} (x= 0, 1 and 12 mol%) were found to be 56.1, 59.4, and 62.3 nm and 0.0178, 0.014, and 0.012, respectively.
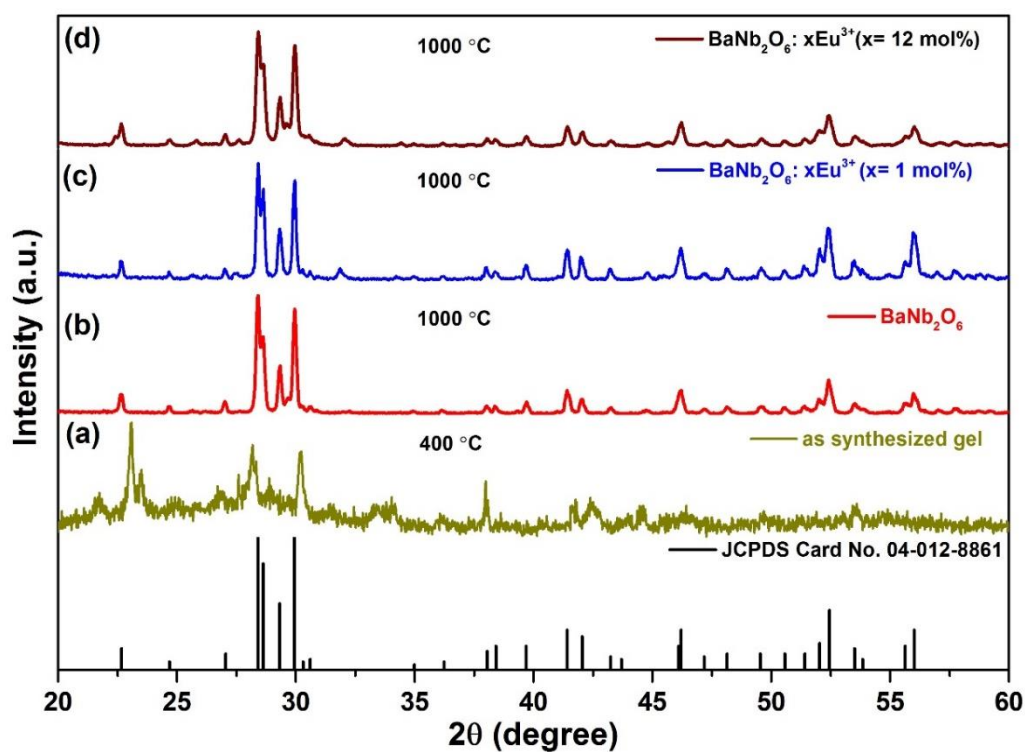
Figure 6.12. X-ray diffraction pattern for as synthesized gel powder at 400 °C and $BaNb_2O_6$: xEu^{3+} (0, 1 and 12 mol%) calcined at 1000 °C.
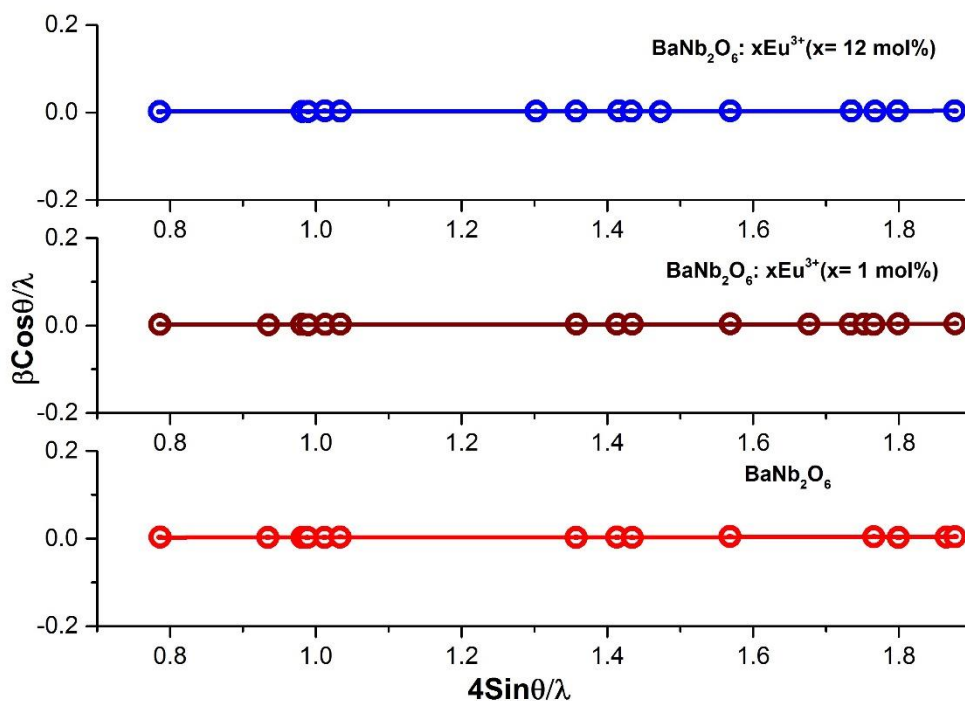
Figure 6.13. Williamson-Hall (W-H) plot for $BaNb_2O_6$: xEu^{3+} (x= 0, 1 and 12 mol%).
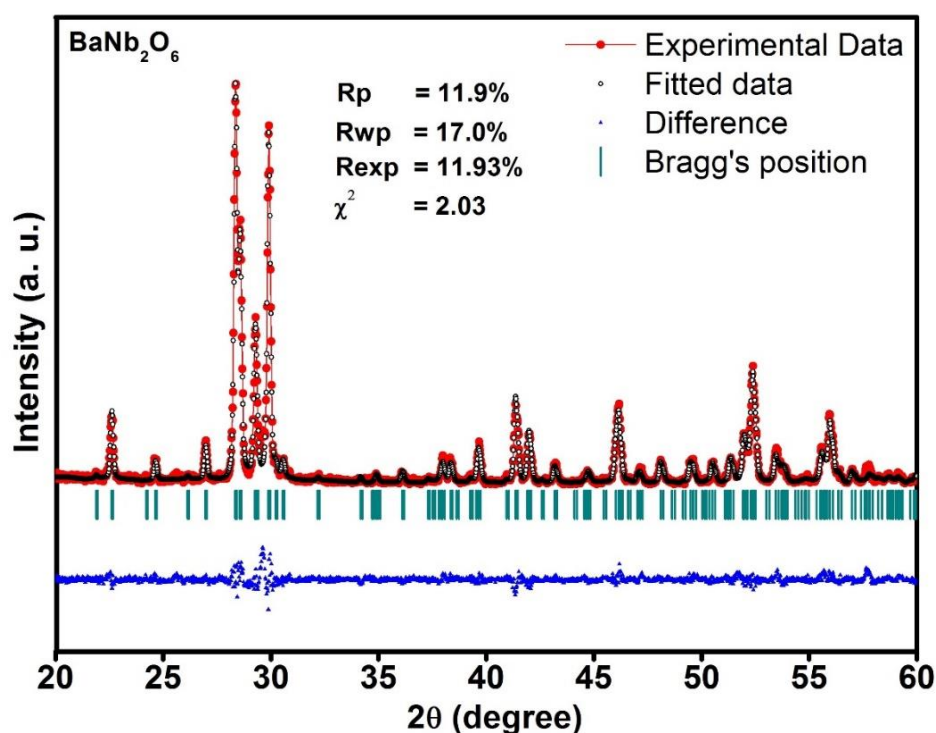
Figure 6.14. Rietveld refinement of $BaNb_2O_6$ powder synthesized via MCG method.

The experimental, calculated and difference results of the XRD refinement of $BaNb_2O_6$ were obtained using FullProf Suite program and represented in Figure. 6.14 [95,96]. The calculated lattice parameters were a= 7.8623 Å, b= 12.1949 Å and c= 10.2776 Å and volume is 985.416 $Å^3$. All the observed peaks satisfy the reliability factors as follows: χ^2= 2.03, R_p= 11.9%, R_{wp}= 17.0%, R_{exp}= 11.93% and confirms the orthorhombic structure of $BaNb_2O_6$ with space group $C222_1$ (20).

6.3.2.3. FE-SEM morphology

The surface morphology of an optimized sample, interpreted by using FE-SEM picture is shown in Figure 6.15. The observed particles are homogeneous in regular distribution and found to be the nano-meter size in the range of 60 - 70 nm. It should be noted that this particle size is uniform, spherical and better than Eu^{3+} doped $BaNb_2O_6$ phosphors synthesized via SSR method as shown in section 6.3.1.2 [188].
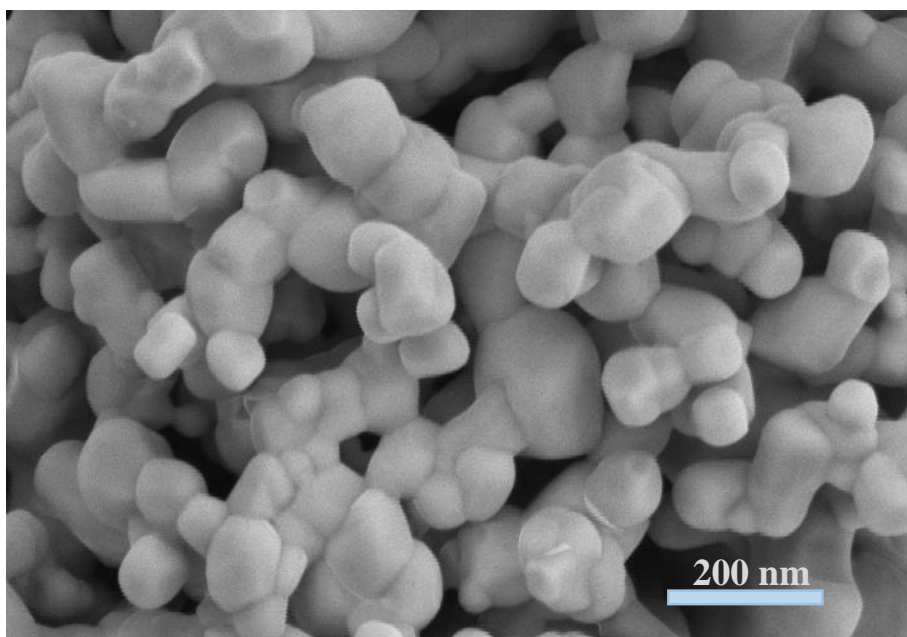
Figure 6.15. FE-SEM image of 12 mol% Eu^{3+} doped $BaNb_2O_6$ sample prepared via MCG method.

6.3.2.4. Photoluminescence excitation and emission

The photoluminescence excitation spectra recorded for $BaNb_2O_6$: xEu^{3+} (x=1, 4, 8, 12 and 16 mol%) nanophosphors are represented in Figure 6.16. The excitation peaks of the observed spectra are similar to the Eu^{3+} spectrum as discussed in the sections 6.3.1.4 and 5.3.2. Inset of Figure 6.16 shows the broad excitation band within the range from 315-360 nm, which is due to charge transfer band of O^{2-} to Eu^{3+} indicating the absorption of the NbO_6 group. Diffuse reflectance spectrum of 1 mol% Eu^{3+} doped $BaNb_2O_6$ nanophosphors is represented by dotted lines. Absorption bands are well matched with the excitation peaks of the $BaNb_2O_6$: Eu^{3+} nanophosphors as shown in Figure 6.16.

The measured emission spectra for $BaNb_2O_6$: xEu^{3+} (x=1, 4, 8, 12 and 16 mol%) nanophosphors are shown in Figure 6.17. The characteristic features of emission spectra exhibit similar profiles as observed and discussed in the sections 6.3.1.4 and 5.3.2, with variation in intensity under 466 and 395 nm excitation wavelengths. Moreover, the concentration quenching also observed at 12 mol% for Eu^{3+} doped $BaNb_2O_6$ nanophosphors synthesized by MCG method.
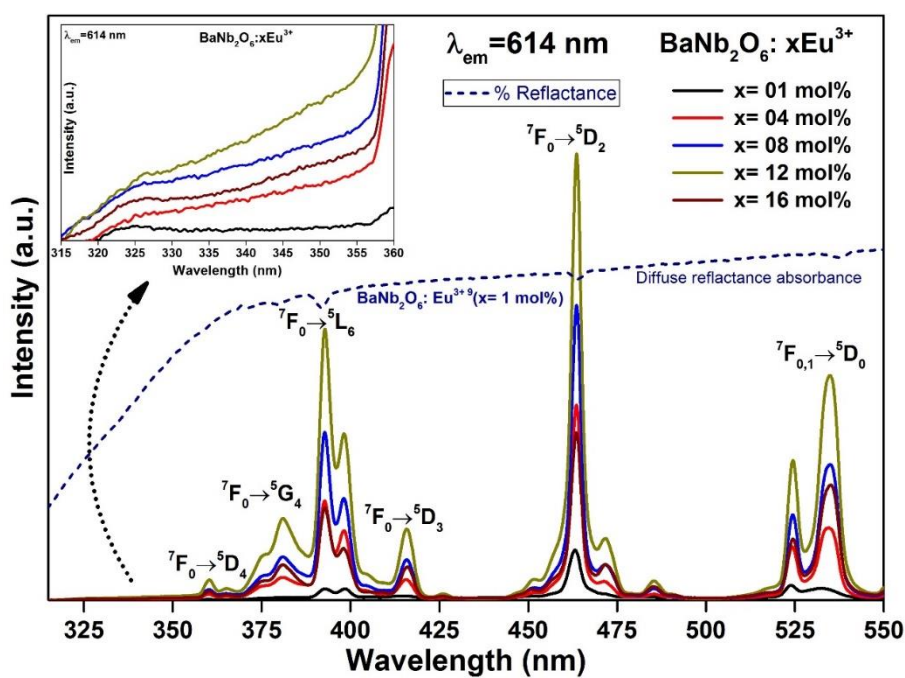
Figure 6.16. Excitation spectra of BaNb$_2$O$_6$: xEu^{3+} phosphor at λ$_{em}$= 614 nm.
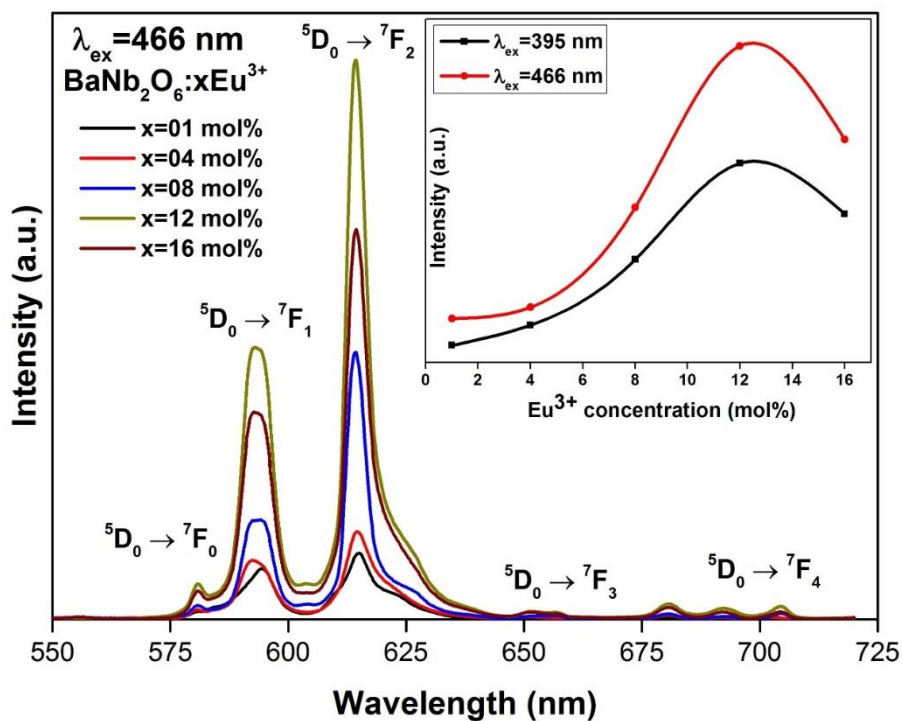
Figure 6.17. Emission spectra of BaNb$_2$O$_6$: xEu^{3+} phosphor at λ$_{ex}$= 466 nm.

6.3.2.5. Comparison of emission intensity of phosphors prepared by SSR and MCG methods

The emission spectra of 12 mol% Eu^{3+} doped $BaNb_2O_6$ phosphors prepared by SSR and MCG methods are shown in Figure 6.18. Both the spectrum resembles the same emission lines under 466 nm excitation wavelength. The emission intensity of the sample prepared by MCG method has been significantly enhanced more than three times relative to the sample synthesized by SSR method.
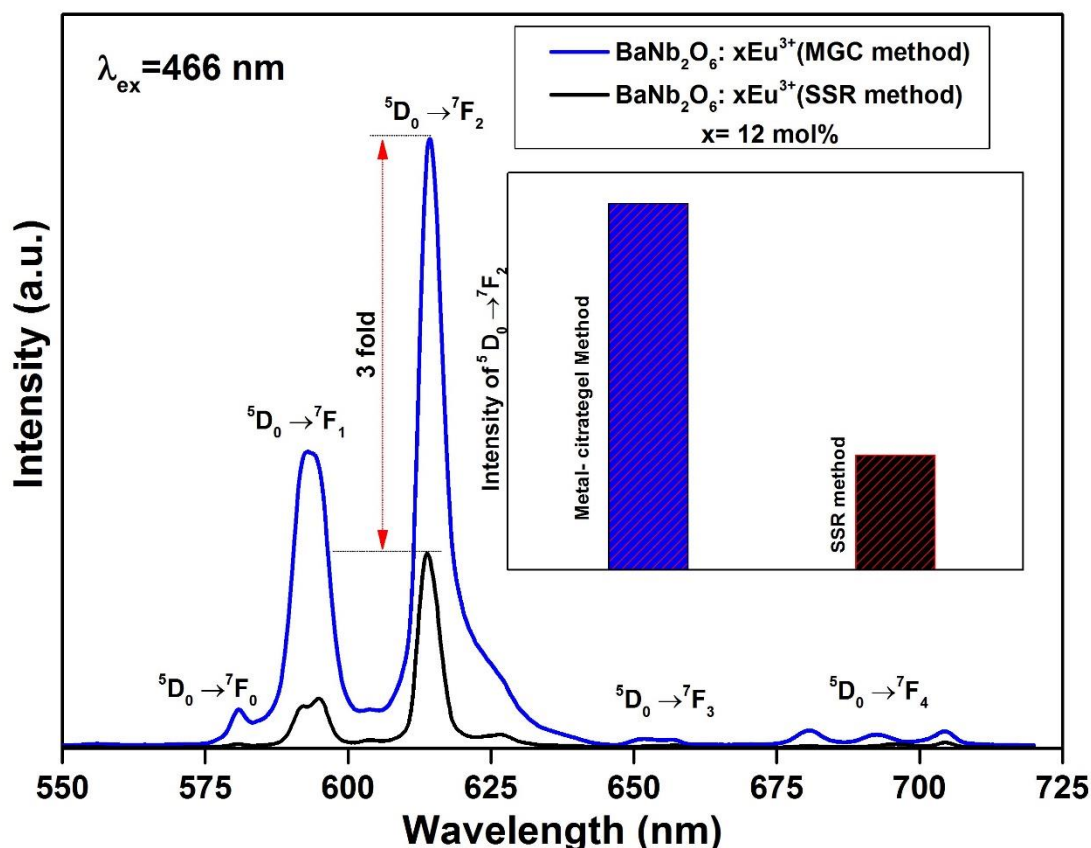
Figure 6.18. Comparison of emission spectra of 12 mol% Eu^{3+} doped $BaNb_2O_6$ phosphors synthesized via SSR and MCG methods.

6.3.2.6 CIE chromaticity coordinates

Figure 6.19 represents the CIE chromaticity coordinates on the CIE 1931 diagram. The calculated chromaticity coordinates of 12 mol% of Eu^{3+} doped $BaNb_2O_6$ are found to be (0.64, 0.35), and (0.63, 0.36) for MCG and SSR methods, respectively. Moreover, the calculated chromaticity coordinates are very much close to the NTSC standard value (0.67, 0.33) for the red emitting phosphor [188,212]. These chromaticity

coordinates suggest that Eu^{3+} doped $BaNb_2O_6$ are the efficient red emitting phosphor candidate for w-LEDs applications.
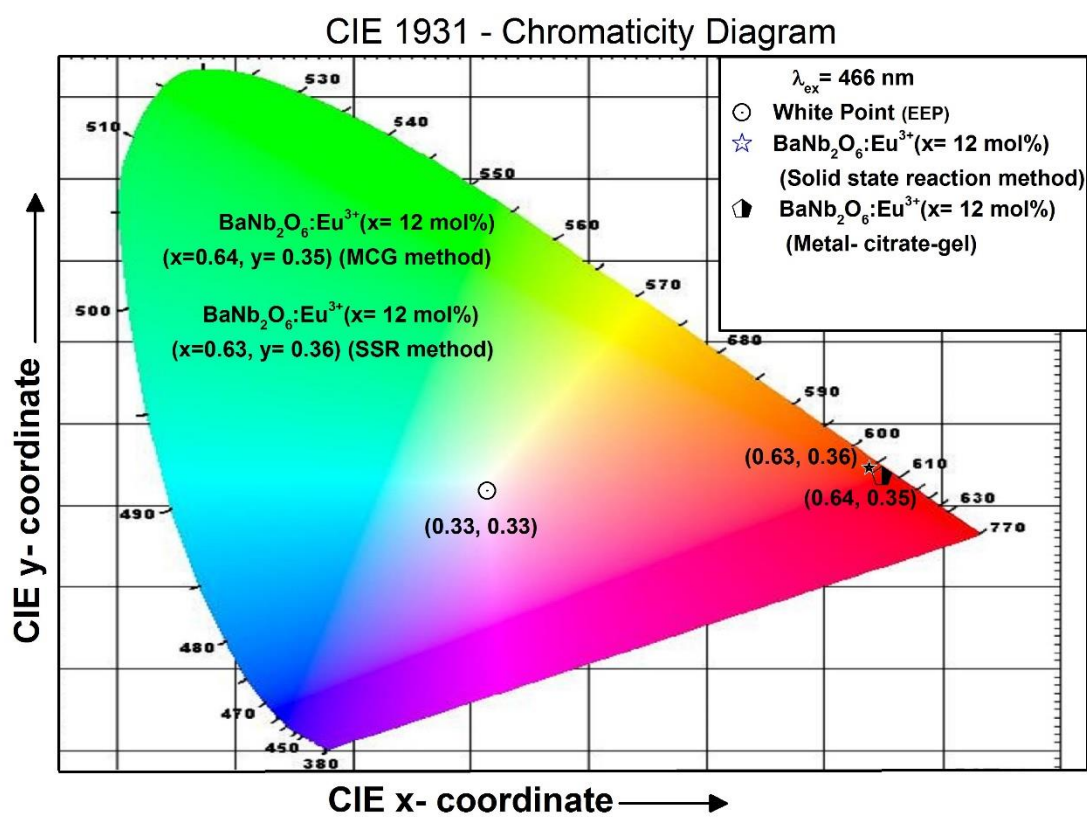
Figure 6.19. CIE chromaticity diagram for 12 mol% Eu^{3+} doped $BaNb_2O_6$ phosphor synthesized by MCG and SSR methods.

7

Summary and Scope for Future work

This chapter summarizes the relevant conclusions and the present status of the work. The general outcome of the thesis focussed on the development of new phosphors, which can be effectively excited by n-UV and blue LEDs with improved emission properties. The future work and scope of the present work are also discussed in the present chapter.
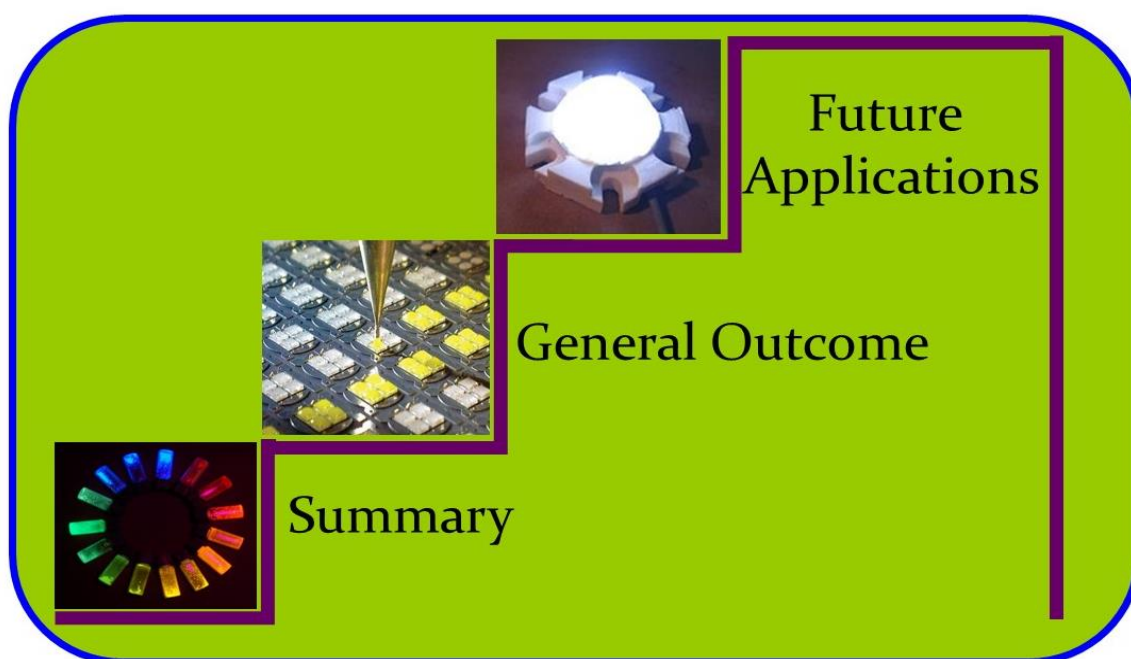
7.1. Summary

The objectives of the thesis were to synthesize and investigate the photoluminescent properties of rare earth doped alkaline eath niobate phosphors for solid state lighting applications. White, orange and red emitting single phase $BaNb_2O_6$ phosphors were successfully synthesized by solid state reaction method using suitable rare earth dopants (Dy^{3+}, Sm^{3+}, and Eu^{3+}). Further, enhancement of red emission was achieved via flux assisted SSR and MCG methods.

As discussed in previous chapters, phosphor converted w-LEDs are emerging as essential solid state light sources for display and illumination devices due to their unique properties such as energy saving, environmental friendliness, long lifetime etc. Therefore, in the present thesis Dy^{3+} doped $BaNb_2O_6$ phosphors have been synthesized for generating white light emission. The thermal, structural, morphological and photoluminescent properties of the phosphor samples have been performed. In addition, Sm^{3+} doped $BaNb_2O_6$ phosphors were synthesized to obtain orange emission, which could be used as orange component in generating white light with the combination of cyan and orange.

Phosphors converted w-LEDs have several shortcomings such as low CRI, halo effect due to lack of red component. Therefore, it is necessary to develop chemically and thermally stable, environment-friendly red phosphors along with better luminescent properties for fabricating highly efficient w-LEDs [6,213]. The commercially available red emitting phosphors, Y_2O_3: Eu^{3+}, Y_2O_2S: Eu^{3+}, CaS: Eu^{2+}, exhibit weak emission intensity, chemical instability and has poor absorption [213,214]. In this pursuit, red emitting Eu^{3+} doped $BaNb_2O_6$ phosphors have been synthesized by SSR method to use as red component for n-UV/blue based white LEDs. Moreover, the emission intensity significantly enhanced for this phosphor by synthesizing via flux assisted SSR and MCG methods. This work will be helpful to improve the CRI of commercial white LEDs and also useful for RGB white LEDs.

7.2. Important Findings of Research Work

The structural properties such as crystallinity, phase purity and crystallite size of rare earth doped $BaNb_2O_6$ phosphors were explored by using XRD. The XRD patterns of all the rare earth doped $BaNb_2O_6$ phosphors in present work are in good agreement with the standard PDF4+ (ICDD) Card No. 04-012-8861, which confirms the single phase orthorhombic structure of $BaNb_2O_6$ with space group $C222_1$ (20).

The morphology of the synthesized rare earth doped $BaNb_2O_6$ phosphors observed by SEM/FE-SEM images. Interestingly, the phosphors synthesized by MCG method exhibit spherical particles in nano regime and rest of the phosphors prepared by SSR method with in the micrometre range with irregular shape and inhomogeneous morphology.

Moving forward to the photoluminescence properties of the rare earth doped $BaNb_2O_6$ phosphors, the salient features of the current thesis are summarized as:

Excitation spectra measured for Dy^{3+} doped $BaNb_2O_6$ phosphors, which indicate that these phosphors could be effectively excited by n-UV LED chips with an excitation wavelength of 386 nm. The optimized Dy^{3+} concentration has been found based on the concentration dependent luminescent spectra. The blue (482 nm) and yellow (574 nm) emission bands corresponding to $^4F_{9/2} \rightarrow {}^6H_J$ (J = 15/2 and 13/2) transitions and the value of Y/B ratio has been found in the vicinity of unity. The combination of these emission bands emits white light and the CIE chromaticity coordinates for the optimized phosphor are (x = 0.322, y = 0.339) with a CCT value of 5907 K, which are close to the standard white lamp colorimetric point in the cool white region. All the above-mentioned results indicate that the Dy^{3+} ion doped $BaNb_2O_6$ phosphor could be used as a practical potential luminescent material for n-UV based w-LED applications.

For Sm^{3+} doped $BaNb_2O_6$ phosphors, the intense orange emission at 599 nm ($^4G_{5/2} \rightarrow {}^6H_{7/2}$ transition) has been observed under 405 nm wavelength excitation, and the optimized doping concentration has been found at 1.5 mol%. The CIE chromaticity coordinates were found to be (0.557, 0.440), which is in close proximity to the Nichia corporation developed amber LED. The calculated color purity was found to be 99.5%,

which confirms the pure orange emission from Sm^{3+} doped $BaNb_2O_6$ phosphor and CCT value was 1970 K. The decay curves were well fitted to the double exponential function, and the average lifetimes for the $^4G_{5/2}$ excited level of Sm^{3+} in the present host is in the range of microseconds. The above mentioned results suggest that the Sm^{3+} doped $BaNb_2O_6$ phosphor is a potential candidate for use in the fabrication of w-LEDs and displays applications.

The photoluminescent spectra of Eu^{3+} doped $BaNb_2O_6$ phosphors exhibit characteristic emission transitions of Eu^{3+}, i.e. $^5D_0 \rightarrow {}^7F_J$ (J = 0, 1, 2, 3, 4) under n-UV/blue excitation wavelengths. Eu^{3+} doped $BaNb_2O_6$ phosphor exhibit concentration quenching beyond 12 mol% of Eu^{3+} ion concentration due to energy transfer processes. The calculated CIE chromaticity coordinates are very much closer to the commercial red phosphor (Y_2O_2S: Eu^{3+}). The above mentioned results indicate that this Eu^{3+} doped $BaNb_2O_6$ phosphors could be useful as red component in the fabrication of n-UV/blue based w-LEDs.

Eu^{3+} doped $BaNb_2O_6$ phosphors synthesized by flux assisted SSR and MCG methods. The optical band gap for the $BaNb_2O_6$ phosphor has been found to be 3.37 eV. The phosphors exhibit strong red emission under blue wavelength (466 nm) excitation. Flux dependent luminescent studies suggested that NH_4Cl flux is the best suitable flux among all other chloride fluxes for Eu^{3+} doped $BaNb_2O_6$ phosphor, which enhanced the emission intensity for two times when compared to the phosphor with same doping concentration (without flux). On the other hand, the emission intensity has been three times higher than the intensity observed for the Eu^{3+} doped $BaNb_2O_6$ nanophosphors synthesized by MCG method when compared to the optimized phosphor synthesized by SSR method (without flux). The calculated CIE coordinates have been found to be (0.65, 0.35) and (0.64, 0.35) for the optimized sample synthesized by flux assisted SSR and MCG methods, respectively. It is interesting to note that these coordinates are close to the NTSC standard for red color and also for commercial red phosphor (Y_2O_3: Eu^{3+}).

The aforementioned results confirm that rare earth doped $BaNb_2O_6$ phosphors developed in this current study could be useful for solid state lighting applications and especially for w-LEDs.

7.3. Scope of Future Work

1. To enhance the luminescence properties for Eu^{3+} doped $BaNb_2O_6$ phosphor by using suitable co-dopant. (for ex: Bi^{3+} may act as sensitizer; as the excitation peak of Eu^{3+} is exactly matching with Bi^{3+} emission)

2. New synthesis routes to be devised to improve the particle shape/morphology, luminescence properties and also to reduce the particle size

3. Investigation on luminescent properties of new hosts ($Ba_2NaNb_5O_{15}$, $Ba_2LiNb_5O_{15}$) explored in the flux assisted SSR method (section 6.3.1.1).

4. Enhancement of CRI by mixing red emitting $BaNb_2O_6$ phosphor to the commercial Ce^{3+}:YAG phosphor

5. To fabricate prototype phosphor converted white LED by using rare earth doped $BaNb_2O_6$ phosphor.

6. To extend the utility of this phosphor for other possible applications such as plasma display panels, solar cell, IR and UV detection, FEDs etc.

References

[1] C.C. Lin, A. Meijerink, R.-S. Liu, J. Phys. Chem. Lett. 7 (2016) 495–503.

[2] B. Valeur, N. Berberan-Santos, J. Chem. Educ. 88 (2011) 731–738.

[3] H. Chander, Proc. ASID (2006) 11–22.

[4] X. Liu, J. Qiu, Chem. Soc. Rev. 44 (2015) 8714–8746.

[5] A. H. Kitai, Solid State Luminescence, Springer, Netherlands, 1993.

[6] K.N. Shinde, S.J. Dhoble, H.C. Swart, K. Park, Phosphate Phosphors for Solid-State Lighting, Springer-Verlag Berlin Heidelberg, 2012.

[7] M. Raukas, J. Kelso, Y. Zheng, K. Bergenek, D. Eisert, A. Linkov, F. Jermann, ECS J. Solid State Sci. Technol. 2 (2012) R3168–R3176.

[8] G. Blasse, B.C. Grabmaier, Luminescent Materials, Springer-Verlag, Germany, 1994.

[9] M. Leskelä, J. Alloys Compd. 275 (1998) 702–708.

[10] K. Binnemans, Chem. Rev. 109 (2009) 4283–4374.

[11] A. Kitai, Luminescent Materials and Applications, John Wiley & Sons Ltd, England, 2008.

[12] G. Bai, M.K. Tsang, J. Hao, Adv. Opt. Mater. 3 (2015) 431–462.

[13] T. Jüstel, H. Nikol, C. Ronda, Angew. Chemie - Int. Ed. 37 (1998) 3084–3103.

[14] B.L. Abrams, P.H. Holloway, Chem. Rev. 104 (2004) 5783–5801.

[15] N. Thejo Kalyani, S.J. Dhoble, Renew. Sustain. Energy Rev. 44 (2015) 319–347.

[16] J.R. Lakowicz, Principles of Fluorescence Spectroscopy, 3rd ed., Springer Science+Business Media, LLC, Singapore, 2006.

[17] F. Wang, X. Liu, Chem. Soc. Rev. 38 (2009) 976–989.

[18] V.B. Pawade, H.C. Swart, S.J. Dhoble, Renew. Sustain. Energy Rev. 52 (2015) 596–612.

[19] S. Ye, F. Xiao, Y.X.X. Pan, Y.Y.Y. Ma, Q.Y.Y. Zhang, Mater. Sci. Eng. R Reports 71 (2010) 1–34.

[20] N. Thejokalyani, S.J. Dhoble, Renew. Sustain. Energy Rev. 32 (2014) 448–467.

[21] W. Zheng, P. Huang, D. Tu, E. Ma, H. Zhu, X. Chen, Chem. Soc. Rev. 44 (2015) 1379–1415.

[22] S. V Eliseeva, J.-C.G. Buenzli, Chem. Soc. Rev. 39 (2010) 189–227.

[23] N. Yeh, T.J. Ding, P. Yeh, Renew. Sustain. Energy Rev. 51 (2015) 55–61.

[24] F. Auzel, Chem. Rev. 104 (2004) 139–173.

[25] X. Huang, S. Han, W. Huang, X. Liu, Chem. Soc. Rev. 42 (2013) 173–201.

[26] K.A. Gschneidner, L. Eyring, Handbook on the Physics and Chemistry of Rare Earths, Elsevier Science B.V, 1998.

[27] G.H. Dieke, H.M. Crosswhite, B. Dunn, J. Opt. Soc. Am. 51 (1961) 820–827.

[28] W.J. Miniscalco, Rare-Earth-Doped Fiber Lasers and Amplifiers, 2nd ed., Taylor & Francis, New York, 2001.

[29] G.H. Dieke, Spectra and Energy Levels of Rare Earth Ions in Crystals, Interscience Publishers, New York, 1968.

[30] W.T. Carnall, P.R. Fields, K. Rajnak, J. Chem. Phys. 49 (1968) 4424–4442.

[31] G. Blasse, A. Bril, R. Mn, J. Chem. Phys. 47 (1967) 1920–1926.

[32] J.C. Boyer, F. Vetrone, J.A. Capobianco, A. Speghini, M. Bettinelli, J. Phys. Chem. B 108 (2004) 20137–20143.

[33] R. Saraf, C. Shivakumara, S. Behera, H. Nagabhushana, N. Dhananjaya, RSC Adv. 5 (2015) 4109–4120.

[34] D.G. Karraker, Inorg. Chem. 6 (1967) 1863–1868.

[35] G.R. Choppin, D.E. Henrie, K. Buijs, Inorg. Chem. 5 (1966) 1743–1748.

[36] P. Patel, MRS Bull. 36 (2011) 678–680.

[37] V.K. Khanna, Fundamentals of Solid-State Lighting, CRC Press Taylor & Francis Group, 2014.

[38] M.S. Shur, A. Žukauskas, Proc. IEEE 93 (2005) 1691–1703.

[39] E. Fred Schubert, Light Emitting Diodes, 2nd ed., Cambridge University Press, New York, 2005.

[40] X. Huang, Nat. Photonics 8 (2014) 748–749.

[41] A. Kar, A. Kar, Proceeding IEEE Int. Conf. Green Comput. Commun. Electr. Eng. ICGCCEE 2014 (2014) 1–6.

[42] S. Bhardwaj, T. Özçelebi, R. Verhoeven, J. Lukkien, IEEE Trans. Consum. Electron. 57 (2011) 1612–1621.

[43] D.A. Steigerwald, J.C. Bhat, D. Collins, R.M. Fletcher, M.O. Holcomb, M.J. Ludowise, P.S. Martin, S.L. Rudaz, IEEE J. Sel. Top. Quantum Electron. 8 (2002) 310–320.

[44] A. Ẑukauskas, R. Vaicekauskas, F. Ivanauskas, H. Vaitkeviĉius, P. Vitta, M.S. Shur, IEEE J. Sel. Top. Quantum Electron. 15 (2009) 1753–1762.

[45] S. Pimputkar, J.S. Speck, S.P. DenBaars, S. Nakamura, Nat. Photonics 3 (2009)

180–182.

[46] N.T. Tran, J.P. You, F.G. Shi, J. Light. Technol. 27 (2009) 5145–5150.

[47] B. Jacob, Light. Res. Technol. 41 (2009) 219–228.

[48] X. Wang, J. Li, P. Shi, W. Guan, H. Zhang, Opt. Mater. (Amst). 46 (2015) 432–437.

[49] F. Kang, Y. Zhang, M. Peng, Inorg. Chem. 54 (2015) 1462–1473.

[50] Y.C. Chang, C.H. Liang, S.A. Yan, Y.S. Chang, 114 (2010) 3645–3652.

[51] R.J. Xie, Y.Q. Li, N. Hirosaki, H. Yamamoto, Nitride Phosphors and Solid-State Lighting, Taylor & Francis, New York, 2011.

[52] X. Li, J.D. Budai, F. Liu, J.Y. Howe, J. Zhang, X.-J. Wang, Z. Gu, C. Sun, R.S. Meltzer, Z. Pan, Light Sci. Appl. 2 (2013) e50.

[53] K. Binnemans, Coord. Chem. Rev. 295 (2015) 1–45.

[54] P.A. Tanner, L. Fu, B.M. Cheng, J. Phys. Chem. C 113 (2009) 10773–10779.

[55] P.A. Tanner, Y.Y. Yeung, L. Ning, J. Phys. Chem. A 117 (2013) 2771–2781.

[56] L.N. Tripathi, B.R. Chaubey, C.P. Mishra, Phys. Stat. Sol. A 60 (1980) 185–192.

[57] Y.F. Lin, Y.H. Chang, Y.S. Chang, B.S. Tsai, Y.C. Li, J. Alloys Compd. 421 (2006) 268–272.

[58] D.C. Rodriguez Burbano, E. Martin Rodriguez, P. Dorenbos, M. Bettinelli, J.A. Capobianco, J. Mater. Chem. C Mater. Opt. Electron. Devices 2 (2014) 228–231.

[59] K. Kato, F. Okamoto, Jpn. J. Appl. Phys. 22 (1983) 76–78.

[60] Y.R. Do, J. Electrochem. Soc. 147 (2000) 1597–1600.

[61] J. Satapathy, M.V.R. Reddy, Int. J. Appl. Phys. Math. 1 (2011) 6–9.

[62] F. Galasso, G. Layden, G. Ganung, U. Aircraft, E. Hartford, Mater. Res. Bull. 3 (1968) 397–408.

[63] I.S. Cho, S.T. Bae, D.H. Kim, K.S. Hong, Int. J. Hydrogen Energy 35 (2010) 12954–12960.

[64] W.M. Yen, S. Shionoya, H. Yamamoto, Phosphor Handbook, 2nd ed., CRC Press Taylor & Francis Group, New York, 2003.

[65] M.H. Crawford, IEEE J. Sel. Top. Quantum Electron. 15 (2009) 1028–1040.

[66] I. Ahemen, Dilip, K. De, A.N. Amah, Appl. Phys. Res. 6 (2014) 95–108.

[67] S. Reineke, M. Thomschke, B. Lussem, K. Leo, Rev. Mod. Phys. 85 (2013) 1245–1293.

[68] C.J. Humphreys, MRS Bull. 33 (2008) 459–470.

[69] M.R. Krames, O.B. Shchekin, R. Mueller-Mach, G.O. Mueller, L. Zhou, G. Harbers, M.G. Craford, J. Disp. Technol. 3 (2007) 160–175.

[70] J.M. Phillips, M.E. Coltrin, M.H. Crawford, A.J. Fischer, M.R. Krames, R. Mueller-Mach, G.O. Mueller, Y. Ohno, L.E.S. Rohwer, J.A. Simmons, J.Y. Tsao, Laser Photonics Rev. 1 (2007) 307–333.

[71] I.L. Azevedo, M.G. Morgan, F. Morgan, Proc. IEEE 97 (2009) 481–510.

[72] C.S. McCamy, Color Res. Appl. 17 (1992) 142–144.

[73] R.C. Ropp, Encyclopedia of the Alkaline Earth Compounds, Elsevier B.V, Amsterdam, 2013.

[74] T.H. Fang, Y.J. Hsiao, Y.S. Chang, Y.H. Chang, Mater. Chem. Phys. 100 (2006) 418–422.

[75] J. Wu, D. Xue, CrystEngComm 13 (2011) 3773–3781.

[76] A. Wachtel, J. Electrochem. Soc. 111 (1964) 534–538.

[77] G. Blasse, M.G.J. van Leur, Mater. Res. Bull. 20 (1985) 1037–1045.

[78] G. Blasse, L.H. Brixner, Mater. Res. Bull. 24 (1989) 363–366.

[79] R.C. Pullar, J.D. Breeze, N.M. Alford, J. Am. Ceram. Soc. 88 (2005) 2466–2471.

[80] M. Nazarov, D.Y. Noh, New Generation of Europium and Terbium Activated Phosphors, Pan Stanford Publishing, 2015.

[81] C. Guo, H.K. Yang, J.H. Jeong, J. Lumin. 130 (2010) 1390–1393.

[82] Y. Li, M. Gecevicius, J. Qiu, Chem. Soc. Rev. 45 (2016) 2090–2136.

[83] Z. Wang, H. Liang, M. Gong, Q. Su, Electrochem. Solid-State Lett. 8 (2005) H33–H36.

[84] S. Ekambaram, K.C. Patil, J. Alloys Compd. 217 (1995) 104–107.

[85] Q. Ma, B. Zhai, Y.M. Huang, Ceram. Int. 41 (2015) 5830–5835.

[86] S.R. Lukić, D.M. Petrović, M.D. Dramićanin, M. Mitrić, L. Dačanin, Scr. Mater. 58 (2008) 655–658.

[87] K.C. Patil, M.S. Hegde, T. Rattan, S.T. Aruna, Nanocrystalline Oxide Materials Combustion Synthesis, Properties and Applications, World Scientific Publishing Co. Pte. Ltd, Singapore, 2013.

[88] J.H. Park, W. Ahn, Y.J. Kim, Ceram. Int. 41 (2015) S734–S739.

[89] K. V Dabre, S.J. Dhoble, J. Lochab, J. Lumin. 149 (2014) 348–352.

[90] J.I. Golstein, C.E. Lyman, D.E. Newbury, E. Lifshin, P. Echlin, L. Sawyer, D.C. Joy, J.R. Michael, Scanning Electron Microscopy and X-Ray Microanalysis,

Kluwer Academic/Plenum Publisher, New York, 2015.

[91]   M.E. Brown, P.K. Gallagher, Handbook of Thermal Analysis and Calorimetry, Elsevier B.V, Amsterdam, 2003.

[92]   S. Yamazoe, T. Kawawaki, K. Shibata, K. Kato, T. Wada, Chem. Mater. 23 (2011) 4498–4504.

[93]   N. Salah, N.D. Alharbi, S.S. Habib, S.P. Lochab, J. Lumin. 167 (2015) 59–64.

[94]   B.D. Cullity, Elements of X-Ray Diffraction, Addison- Wesley Publishing Company, Inc, Philippines, 1978.

[95]   H.M. Rietveld, J. Appl. Crystallogr. 2 (1969) 65–71.

[96]   B.H. Toby, Powder Diffr. 21 (2006) 67–70.

[97]   M. Seibald, O. Oeckler, V.R. Celinski, P.J. Schmidt, A. Tucks, W. Schnick, Solid State Sci. 13 (2011) 1769–1778.

[98]   J.G. Sole, L.E. Bausa, D. Jaque, An Introduction to the Optical Spectroscopy of Inorganic Solids, JohnWiley & Sons Ltd, England, 2005.

[99]   M. Zhang, Y. Liang, R. Tang, D. Yu, M. Tong, Q. Wang, Y. Zhu, X. Wu, G. Li, RSC Adv. 4 (2014) 40626–40637.

[100]   H. Qian, J. Zhang, L. Yin, RSC Adv. 3 (2013) 9029.

[101]   S.H. Park, K.H. Lee, S. Unithrattil, H.S. Yoon, H.G. Jang, W. Bin Im, J. Phys. Chem. C 116 (2012) 26850–26856.

[102]   Y. Uchida, T. Taguchi, Opt. Eng. 44 (2005) 124003–124011.

[103]   H.S. Jang, W. Bin Im, D.C. Lee, D.Y. Jeon, S.S. Kim, J. Lumin. 126 (2007) 371–377.

[104]   S. Nakamura, S. Pearton, G. Fasol, The Blue Laser Diode, 2nd ed., Springer-Verlag Berlin Heidelberg GmbH, 2000.

[105]   J.K. Sheu, S.J. Chang, C.H. Kuo, Y.K. Su, L.W. Wu, Y.C. Lin, W.C. Lai, J.M. Tsai, G.C. Chi, R.K. Wu, IEEE Photonics Technol. Lett. 15 (2003) 18–20.

[106]   K. Li, X. Liu, Y. Zhang, X. Li, H. Lian, J. Lin, Inorg. Chem. 54 (2015) 323–333.

[107]   Y. Zhou, Z. Qiu, M. Lu, Q. Ma, A. Zhang, G. Zhou, J. Phys. Chem. C 111 (2007) 10190–10193.

[108]   M.K. Ekmekçi, M. Erdem, A.S. Başak, Dalt. Trans. 44 (2015) 5379–5385.

[109]   M.K. Ekmekci, M. Erdem, A. Mergen, G. Ozen, B. Di Bartolo, J. Alloys Compd. 591 (2014) 230–233.

[110]   D. Van der Voort, J.M.E. de Ruk, G. Blasse, Phys. Stat. Sol. A 135 (1993) 621–

626.

[111] A.K. Parchur, A.I. Prasad, S.B. Rai, R.S. Ningthoujam, Dalton Trans. 41 (2012) 13810–13814.

[112] M. Jayasimhadri, B. V. Ratnam, K. Jang, H.S. Lee, B. Chen, S.S. Yi, J.H. Jeong, L. Rama Moorthy, Int. J. Appl. Ceram. Technol. 8 (2011) 709–717.

[113] K. Mishra, S.K. Singh, A.K. Singh, S.B. Rai, Mater. Res. Bull. 47 (2012) 1339–1344.

[114] V.P. Sirotinkin, S.P. Sirotinkin, Russ. J. Inorg. Chem. 35 (1990) 1246–1248.

[115] S. Bathula, B. Gahtori, M. Jayasimhadri, S.K. Tripathy, K. Tyagi, A.K. Srivastava, A. Dhar, Appl. Phys. Lett. 105 (2014) 2–7.

[116] B.P. Singh, a K. Parchur, R.K. Singh, a a Ansari, P. Singh, S.B. Rai, Phys. Chem. Chem. Phys. 15 (2013) 3480–3489.

[117] A.K. Parchur, R.S. Ningthoujam, S.B. Rai, G.S. Okram, R.A. Singh, M. Tyagi, S.C. Gadkari, R. Tewari, R.K. Vatsa, Dalton Trans. 40 (2011) 7595–7601.

[118] Y. Zhou, Q. Ma, M. Lu, Z. Qiu, A. Zhang, J. Phys. Chem. C 112 (2008) 19901–19907.

[119] D.L. Monika, H. Nagabhushana, R.H. Krishna, B.M. Nagabhushana, S.C. Sharma, T. Thomas, RSC Adv. 4 (2014) 38655–38662.

[120] E. Pavitra, G. Seeta Rama Raju, W. Park, J.S. Yu, New J. Chem. 38 (2014) 163–169.

[121] Z. Ci, Q. Sun, S. Qin, M. Sun, X. Jiang, X. Zhang, Y. Wang, Phys. Chem. Chem. Phys. 16 (2014) 11597–11602.

[122] B. V. Ratnam, M. Jayasimhadri, K. Jang, H. Sueb Lee, S.S. Yi, J.H. Jeong, J. Am. Ceram. Soc. 93 (2010) 3857–3861.

[123] Q. Su, Z. Pei, L. Chi, H. Zhang, Z. Zhang, F. Zou, J. Alloys Compd. 192 (1993) 25–27.

[124] S. Dutta, S. Som, S.K. Sharma, Dalton Trans. (2013) 9654–9661.

[125] M. Jayasimhadri, K. Jang, H.S. Lee, B.J. Chen, S.S. Yi, J.H. Jeong, J. Appl. Phys. 106 (2009) 1–4.

[126] G.H. Dieke, S. Singh, J. Opt. Soc. Am. 46 (1956) 495–499.

[127] B. Liu, C. Shi, Z. Qi, Appl. Phys. Lett. 86 (2005) 1–3.

[128] Q. Liu, Y. Liu, Z. Yang, Y. Han, X. Li, G. Fu, J. Alloys Compd. 515 (2012) 16–19.

[129] G. Blasse, Philips Res. 24 (1969) 131–144.

[130] Q. Xu, J. Sun, D. Cui, Q. Di, J. Zeng, J. Lumin. 158 (2015) 301–305.

[131] L.G. Van Uitert, J. Electrochem. Soc. 114 (1967) 1048–1053.

[132] D.L. Dexter, J. Chem. Phys. 21 (1953) 836–850.

[133] D.L. Dexter, J.H. Schulman, J. Chem. Phys. 22 (1954) 1063–1070.

[134] H. Li, R. Zhao, Y. Jia, W. Sun, J. Fu, L. Jiang, S. Zhang, R. Pang, C. L, Appl. Mater. Interfaces 6 (2014) 3163–3169.

[135] L. Zhang, H. Zhong, X. Li, L. Cheng, L. Yao, J. Sun, J. Zhang, R. Hua, B. Chen, Phys. B Condens. Matter 407 (2012) 68–72.

[136] J. Suresh Kumar, K. Pavani, A. Mohan Babu, N. Kumar Giri, S.B. Rai, L.R. Moorthy, J. Lumin. 130 (2010) 1916–1923.

[137] M.R.N. Soares, M.J. Soares, A.J.S. Fernandes, L. Rino, F.M. Costa, T. Monteiro, J. Mater. Chem. 21 (2011) 15262–15265.

[138] B.C. Jamalaiah, J. Suresh Kumar, A. Mohan Babu, L. Rama Moorthy, K. Jang, H.S. Lee, M. Jayasimhadri, J.H. Jeong, H. Choi, J. Lumin. 129 (2009) 1023–1028.

[139] M. Jayasimhadri, L. Rama Moorthy, R.V.S.S.N. Ravikumar, Opt. Mater. (Amst). 29 (2007) 1321–1326.

[140] X. Bai, G. Caputo, Z. Hao, V.T. Freitas, J. Zhang, R.L. Longo, O.L. Malta, R.A.S. Ferreira, N. Pinna, Nat. Commun. 5 (2014) 5702–5707.

[141] E. Matioli, S. Brinkley, K.M. Kelchner, Y.-L. Hu, S. Nakamura, S. DenBaars, J. Speck, C. Weisbuch, Light Sci. Appl. 1 (2012) e22.

[142] R. Zhou, L. Wang, M. Xu, D. Jia, J. Alloys Compd. 647 (2015) 136–140.

[143] H. Zhu, C.C. Lin, W. Luo, S. Shu, Z. Liu, Y. Liu, J. Kong, E. Ma, Y. Cao, R.-S. Liu, X. Chen, Nat. Commun. 5 (2014) 4312–4322.

[144] J. Chen, Y. Liu, L. Mei, H. Liu, M. Fang, Z. Huang, Sci. Rep. 5 (2015) 9673–9692.

[145] Z. Wang, P. Li, X. Zhang, Q. Li, T. Li, Z. Yang, Q. Guo, Phys. B Condens. Matter 414 (2013) 56–59.

[146] H. Deng, Z. Zhao, J. Wang, Z. Hei, M. Li, H.M. Noh, J.H. Jeong, R. Yu, J. Solid State Chem. 228 (2015) 110–116.

[147] G. Seeta Rama Raju, J.S. Yu, J.Y. Park, H.C. Jung, B.K. Moon, J. Am. Ceram. Soc. 95 (2012) 238–242.

[148] B. V. Ratnam, M. Jayasimhadri, K. Jang, Spectrochim. Acta - Part A Mol. Biomol. Spectrosc. 132 (2014) 563–567.

[149] A.K. Vishwakarma, K. Jha, M. Jayasimhadri, B. Sivaiah, B. Gahtori, D. Haranath, Dalt. Trans. 44 (2015) 17166–17174.

[150] B. Ding, C. Han, L. Zheng, J. Zhang, R. Wang, Z. Tang, Sci. Rep. 5 (2015) 9443.

[151] K.K. Rasu, D. Balaji, S.M. Babu, J. Lumin. 170 (2016) 547–555.

[152] R. Yu, H. Mi Noh, B. Kee Moon, B. Chun Choi, J. Hyun Jeong, H. Sueb Lee, K. Jang, S. Soo Yi, J. Lumin. 152 (2014) 133–137.

[153] Z. Xia, D. Chen, J. Am. Ceram. Soc. 1401 (2010) 1397–1401.

[154] J. Zheng, J. Feng, Q. Cheng, Z. Guo, L. Cai, C. Chen, Funct. Mater. Lett. 8 (2015) 1550042–1550047.

[155] J. Xu, Z. Ju, X. Gao, Y. An, X. Tang, W. Liu, Inorg. Chem. 52 (2013) 13875–13881.

[156] D. Ramachari, L. Rama Moorthy, C.K. Jayasankar, Mater. Res. Bull. 48 (2013) 3607–3613.

[157] D. Umamaheswari, B.C. Jamalaiah, T. Sasikala, I.G. Kim, L.R. Moorthy, J. Non. Cryst. Solids 358 (2012) 782–787.

[158] A.N. Belsky, J.C. Krupa, Displays 19 (1999) 185–196.

[159] C.. Ronda, T. Jüstel, H. Nikol, J. Alloys Compd. 275–277 (1998) 669–676.

[160] J. Hye Oh, S. Ji Yang, Y. Rag Do, Light Sci. Appl. 3 (2014) e141.

[161] M. Nyman, M.A. Rodriguez, L.E. Shea-Rohwer, J.E. Martin, P.P. Provencio, J. Am. Chem. Soc. 131 (2009) 11652–11653.

[162] A.A. Setlur, J.J. Shiang, U. Happek, Appl. Phys. Lett. 92 (2008) 2006–2009.

[163] C. Ronda, Luminescence From Theory to Applications, WILEY-VCH Verlag GmbH & Co. KGaA, Weinheim, 2008.

[164] H. Daicho, T. Iwasaki, K. Enomoto, Y. Sasaki, Y. Maeno, Y. Shinomiya, S. Aoyagi, E. Nishibori, M. Sakata, H. Sawa, S. Matsuishi, H. Hosono, Nat. Commun. 3 (2012) 1132–1140.

[165] D. Uma Maheswari, J. Suresh Kumar, L.R. Moorthy, K. Jang, M. Jayasimhadri, Phys. B Condens. Matter 403 (2008) 1690–1694.

[166] Y.S. Chang, Z.R. Shi, Y.Y. Tsai, S. Wu, H.L. Chen, Opt. Mater. (Amst). 33 (2010) 2–7.

[167] Z. Yu, G. Zhou, J. Zhou, H. Zhou, P. Kong, Y. Wu, H. Huang, X. Yu, X. Zhang,

R. Zhang, RSC Adv. 5 (2015) 94607–94614.

[168] J. Wang, Y. Cheng, Y. Huang, P. Cai, S. Il Kim, H.J. Seo, J. Mater. Chem. C 2 (2014) 5559–5569.

[169] S. Bathula, R.C. Anandani, A. Dhar, A.K. Srivastava, Mater. Sci. Eng. A 545 (2012) 97–102.

[170] G. Swati, S. Mishra, D. Yadav, R.K. Sharma, D. Dwivedi, N. Vijayan, J.S. Tawale, V. Shanker, D. Haranath, J. Alloys Compd. 571 (2013) 1–5.

[171] X.Z. Xiao, B. Yan, J. Alloys Compd. 433 (2007) 246–250.

[172] J. Hou, P. Chen, G. Zhang, Y. Fang, W. Jiang, F. Huang, Z. Ma, J. Lumin. 146 (2014) 97–101.

[173] U. Rambabu, S. Han, RSC Adv. 3 (2013) 1368.

[174] X. Zhao, J. Wang, L. Fan, Y. Ding, Z. Li, T. Yu, Z. Zou, Dalt. Trans. 42 (2013) 13502–13508.

[175] V.R. Bandi, Y.-T. Nien, I.-G. Chen, J. Appl. Phys. 108 (2010) 023111–023114.

[176] G.S.R. Raju, E. Pavitra, J.S. Yu, Phys. Chem. Chem. Phys. 16 (2014) 18124–18140.

[177] Y. Tian, X. Qi, X. Wu, R. Hua, B. Chen, J. Phys. Chem. C 113 (2009) 10767–10772.

[178] W.T. Carnall, P.R. Fields, K. Rajnak, J. Chem. Phys. 49 (1968) 4450–4455.

[179] S. Qi, D. Wei, Y. Huang, S. Il Kim, Y.M. Yu, H.J. Seo, J. Am. Ceram. Soc. 97 (2014) 501–506.

[180] Y. Du, Y. Zhang, K. Huang, S. Wang, L. Yuan, S. Feng, Dalton Trans. 42 (2013) 8041–8048.

[181] V.R. Bandi, B.K. Grandhe, K. Jang, H.S. Lee, D.S. Shin, S.S. Yi, J.H. Jeong, J. Alloys Compd. 512 (2012) 264–269.

[182] R.J. Xie, N. Hirosaki, N. Kimura, K. Sakuma, M. Mitomo, Appl. Phys. Lett. 90 (2007) 6–9.

[183] G. Seeta Rama Raju, E. Pavitra, G. Nagaraju, J.S. Yu, Dalt. Trans. 44 (2015) 1790–1799.

[184] O. Meza, E.G. Villabona-Leal, L.A. Diaz-Torres, H. Desirena, J.L. Rodríguez-López, P. Elías, J. Phys. Chem. A 118 (2014) 1390–1396.

[185] P. Pust, V. Weiler, C. Hecht, A. Tücks, A.S. Wochnik, A.K. Henß, D. Wiechert, C. Scheu, P.J. Schmidt, W. Schnick, Nat. Mater. 13 (2014) 891–896.

[186] Z. Xia, Y. Zhang, M.S. Molokeev, V. V. Atuchin, J. Phys. Chem. C 117 (2013) 20847–20854.

[187] Maheshwary, B.P. Singh, J. Singh, R.A. Singh, RSC Adv. 4 (2014) 32605–32621.

[188] A.K. Vishwakarma, K. Jha, M. Jayasimhadri, A.S. Rao, K. Jang, B. Sivaiah, D. Haranath, J. Alloys Compd. 622 (2015) 97–101.

[189] H. Chen, R. Yang, S. Chang, Y. Yang, Mater. Res. Bull. 47 (2012) 1412–1416.

[190] X. Li, Z. Yang, L. Guan, C. Liu, P. Li, J. Cryst. Growth 310 (2008) 3117–3120.

[191] R.P. Rao, J. Electrochem. Soc. 152 (2005) H115–H119.

[192] L. Zhang, Z. Lu, P. Han, J. Lu, N. Xu, L. Wang, Q. Zhang, J. Am. Ceram. Soc. 95 (2012) 3871–3877.

[193] B. Liu, Y. Wang, J. Zhou, F. Zhang, Z. Wang, J. Appl. Phys. 106 (2009) 053102–053106.

[194] H.S. Kang, Y.C. Kang, K.Y. Jung, S. Bin Park, Mat. Sci. Eng., B 121 (2005) 81–85.

[195] X. Liu, Y. Lu, C Chem, S. Luo, Y. Zeng, X. Zhang, M. Shang, C. Li, J. Lin, J. Phys. Chem. C 118 (2014) 27516–27524.

[196] D. Hou, X. Guo, C. Liu, T.-K. Sham, H. Liang, J. Gao, X. Sun, B. Zhang, F. Zhan, Y. Huan, Y. Tao, J. Lumin. 165 (2015) 23–29.

[197] C.-T. Lee, F.-S. Chen, C.-H. Lu, J. Alloys Compd. 490 (2010) 407–411.

[198] W. Zhang, Y. Wang, Y. Gao, J. Long, J. Li, J. Alloys Compd. 667 (2016) 341–345.

[199] T.-C. Chien, J.-C. Yang, C.-S. Hwang, M. Yoshimura, J. Alloys Compd. 676 (2016) 286–291.

[200] V. Sivakumar, A. Lakshmanan, J. Lumin. 145 (2014) 420–424.

[201] Y. Ding, W. Yang, Q. Zhang, L. Wang, J Mater Sci Mater Electron 3 (2015) 1982–1986.

[202] Y. Peng, Y. Su, R. Yang, Mater. Res. Bull. 48 (2013) 1946–1951.

[203] A.K. Singh, S.K. Singh, B.K. Gupta, R. Prakash, S.B. Rai, Dalt. Trans. 42 (2013) 1065–1072.

[204] R. Köferstein, L. Jäger, S.G. Ebbinghaus, Solid State Ionics 249–250 (2013) 1–5.

[205] R. López, R. Gómez, J. Sol-Gel Sci. Technol. 61 (2012) 1–7.

[206] Q. Long, Y. Xia, Y. Huang, S. Liao, Y. Gao, J. Huang, J. Liang, J. Cai, Mater. Lett. 145 (2015) 359–362.

[207] P.A. Tanner, Chem. Soc. Rev. 42 (2013) 5090–5101.

[208] V. Singh, R.P.S. Chakradhar, J.L. Rao, J.J. Zhu, Mater. Chem. Phys. 111 (2008) 143–148.

[209] H. Yan, H. Wang, P. He, J. Shi, M. Gong, Synth. Met. 161 (2011) 748–752.

[210] D.B. Bem, A.S. Luyt, F.B. Dejene, J.R. Botha, H.C. Swart, Phys. B Condens. Matter 404 (2009) 4504–4508.

[211] S. Som, S. Das, S. Dutta, H.G. Visser, M.K. Pandey, P. Kumar, R.K. Dubey, S.K. Sharma, RSC Adv. 5 (2015) 70887–70898.

[212] E. Pavitra, G. Seeta Rama Raju, J.Y. Park, Y.H. Ko, J.S. Yu, J. Alloys Compd. 553 (2013) 291–298.

[213] A.K. Vishwakarma, M. Jayasimhadri, J. Alloys Compd. 683 (2016) 379–386.

[214] A.K. Vishwakarma, M. Jayasimhadri, J. Lumin. 176 (2016) 112–117.

CURRICULAM VITAE

AMIT KUMAR VISHWAKARMA

Research Scholar
Luminescent Materials Research Lab (LMRL)
Department of Applied Physics,
Delhi Technological University-110 042
Email: amitvishwakarma85@gmail.com

Research Interest

Synthesis of Rare Earth doped Luminescent materials (Phosphors and Nanophosphors), Glasses and Glass ceramics

Academic Qualifications

❖ Pursuing PhD on the topic entitled **"Synthesis and photoluminescence properties of rare earth-doped alkaline earth niobate phosphors for solid state lighting applications"** in Department of Applied Physics from **Delhi Technological University** (formerly Delhi College of Engineering) , Delhi-42.

❖ **M.Sc.** in Physics in 2004-2006 from V.B.S.Purvanchal University Jaunpur (U.P).

❖ **B.Sc** in (Physics & Mathematics) in 2001-2004 from V.B.S.Purvanchal University Jaunpur (U.P).

❖ **Intermediate** in 2001 from U.P.Board Allahabad.

❖ **High school** in 1999 from U.P.Board Allahabad.

Teaching Experience

➢ Worked as **Assistant Professor** from September 2010 to October 2011 in **IILM-CET Academy of Higher Learning Greater Noida**

➢ Worked as **Lecturer** from December 2007 to August 2010 in **IILM-CET Academy of Higher Learning Greater Noida**.

Awards & Memberships

1. First place and cash prize for best poster presentation in National conference on Luminescence and its Applications (NCLA-2016) at RTM University Nagpur.

2. Received travel grant from Luminescent Society of India (LSI) to attend the National conference on Luminescence and its Applications (NCLA-2016) at RTM University Nagpur.

3. Received travel grant from Delhi Technological University (DTU) to attend the International Union of Material Research Society-(ICA-2013) conference at IISc Bangalore.

4. Lifetime member of Luminescent Society of India (LSI).

5. Member of SPIE-DCE Chapter.

Workshops/Seminars Attended

1. One day national seminar on **"Frontiers in Applied Science & Technology"** organized by Department of Applied Physics at Delhi Technological University, Delhi on 22nd, March, 2016.

2. Workshop on **"Advanced nanomaterials: Characterization and Applications"** organized by Department of Physics at BHU, Varanasi under UGC networking programme during 02-08th ,November, 2015.

3. National seminar on **"Recent Advances in Physics"** organized by Department of Applied Physics at Delhi Technological University, Delhi on 16th, February, 2015.

4. Workshop on **"Frontiers of spectroscopy"** organized by Department of Physics at BHU, Varanasi under UGC networking programme during 8-9th, January, 2015.

5. Workshop on **"Frontiers in Nano Science, Technology and Applications (FiNSTA'14)"** organized by Department of Physics SSSIHL, Puttaparthi (A.P) during 20-22nd, Dec, 2014.

6. Workshop on **"Nano Materials with particular reference to energy security"** organized by Department of Physics at BHU, Varanasi under UGC networking programme during 11-17th, March, 2014.

National and International conferences

1. National Conference on Luminescence and its Applications (NCLA-2016), **17-20th Feb, 2016,** RTM University Nagpur.

2. 5th International Conference on Luminescence and its Applications (ICLA-2015)**, 09 -12th Feb, 2015,** PES University, Bangalore.

3. International Conference on Frontiers of Spectroscopy (ICFS-2015), **10 -12th Jan, 2015,** Department of Physics. BHU, Varanasi.

4. National Conference on Luminescence and its Applications (NCLA-2014), **05-7th February, 2014,** R.D. University, Jabalpur.

5. International Union of Material Research Society-ICA-201**3, 16-20th Dec, 2013,** IISc Bangalore.

6. 3rd National Conference on Innovations in Indian Science Engineering & Technology-2013, **25-27th Feb, 2013,** CSIR-National Physical Laboratory, New Delhi

7. National Conference on Luminescence and its Applications (NCLA-2013), **08-10th Jan, 2013**, PESIT Bangalore.